EFFICIENT NUMERICAL METHODS FOR REYNOLDS AVERAGED NAVIER-STOKES EQUATIONS OF FLOW OVER TOPOGRAPHY AND APPLICATION

XIAO YU

A DISSERTATION SUBMITTED TO THE FACULTY OF GRADUATE STUDIES
IN PARTIAL FULFILMENT OF THE REQUIREMENTS
FOR THE DEGREE OF

DOCTOR OF PHILOSOPHY

GRADUATE PROGRAM IN DEPARTMENT OF MATHEMATICS AND STATISTICS
YORK UNIVERSITY
TORONTO, ONTARIO

JANUARY 2014

© Xiao Yu 2014

Abstract

Recently, wind energy has been used widely as a complement to the common used energy resources such as oil, coal, and natural gas. Fossil fuels can generate heavy pollution and release greenhouse gases, which are recognized as the main cause of the global warming. As a result, green and renewable energy technologies, such as wind energy and solar energy, are highly recommended nowadays. In order to build the wind farms and make the wind energy assessments, wind flow over topography has been studied intensively in wind energy industry.

In my thesis, we first improve an under-relaxed iteration scheme for the steady-state RANS equations of neutrally stratified airflow over complex topography. The NLMSFD scheme failed on predicting flow over terrains with a relatively high slope and we improve this iteration scheme to a much higher maximum slope. In the second part, we develop the efficient characteristic finite volume method (CFV) to

solve the time-dependent RANS equations of flow over topography with various surface roughnesses. In viscous flow, the convective term plays a more important role than the diffusive term, especially for the turbulent flow with a high Reynolds number. The CFV scheme is developed by combining the characteristic method and the finite volume method. It treats the convective term efficiently. Numerical experiments of solving the time-dependent RANS equations with $k - \varepsilon$ closure show the advantages of the accuracy, efficiency and stability of the method. In the last part, the CFV method is further applied to model wind flow and turbine wakes of large wind farms. We simulate the wind turbine wakes behind a cluster of wind farms which take into account the roughness change on the topography. We propose to consider RANS models with the Coriolis effect in modelling wind flows under a large scale due to the rotation of Earth. The wind flows within and downwind of the wind farms are predicted numerically. Simulation results on the Horns Rev wind farm are compared with field measurements.

Acknowledgements

I would like to thank my PhD supervisor Professor Dong Liang for his great guidance and encouragement during my study and research. I would also like to thank Professor Peter A. Taylor, who is my supervisory committee member, for the guidance and helps on my research work. I would like to thank Professor Xin Gao who is my supervisory committee member, and Dr. Wensong Weng who comes from Centre for Research in Earth and Space Science (CRESS) for their suggestions in my research. I also wish to thank York University, Natural Science and Engineering Research Council of Canada (NSERC), Mathematics for Information Technology and Complex Systems (MITACS), and Zephyr North Ltd. for the scholarship and assistantship I was given. Finally I am grateful to my wife Karen (Zijia) Lu and my daughter Chelsea Yu and all other family members for their patience and confidence in me.

Table of Contents

List of Tables

List of Figures

1 Introduction

1.1 Background

Renewable energy resources have been considered as a great supplement to traditional energy resources in the past many years. Wind energy has drawn great attentions after the oil crisis in the 20th century ([71], [3]). As the supplementary energy resource, wind energy is clean and economical. Studies and researches of wind energy are widely involved such as the wind resource assessment ([14], [46], [63], [51]), hardware manufacture and reliability ([89], [36], [17]), environmental impact ([24], [50]), and economic assessment ([84], [2], [15]). Electricity generated by wind power has provided an increased percentage of the total electricity generation year by year. The global wind energy capacity has a growth of 20 percent in 2012 with a total capacity of 282 GW ([30]). Since 2011, wind energy, together with other green energies, are considered as supplement or replacement of the nuclear energy after the Fukushima nuclear crisis ([39], [38]). Scientific studies on wind energy such as wind turbine and wind resource assessment are based on the

boundary-layer meteorology ([60], [61]). Some mathematical models were built for modelling the wind flows over topography analytically and numerically ([41], [52], [81], [76], [12]). Development of efficient numerical techniques has been becoming an important task due to the high complexities of the systems ([87], [88]). Figure 1.1 shows the Exhibition Place turbine in downtown Toronto, the first urban turbine in North America. Figure 1.2 represents the Canadian Wind Atlas which contributed from the EOLE Wind Energy Project, Environment Canada.

The turbulence flow is studied given the nature of the high Reynolds number of the air flow ([37], [29]). Mathematical models are derived based on the Navier-Stokes equations which are used to describe fluid motions. Numerical solutions of Navier-Stokes equations with high Reynolds numbers are very challenging in computational fluid dynamics (CFD). In such problems it causes computational difficulties and nonphysical oscillations. We should introduce the averaged variables and the perturbation terms for the small scale turbulence. If the turbulent flow field is homogeneous, an average in space can be considered. However, if the flow field is neither steady nor homogeneous, we may assume that an average is taken over a large number of experiments that have the same initial and boundary conditions, which is called the ensemble average. There are three major methods used numerically solving the Navier-Stokes equations with or without a turbulence model. In the Direct Numerical Simulation (DNS), the Navier-Stokes equations

Figure 1.1: The Exhibition Place turbine in downtown Toronto, the first urban turbine in North America. Photograph taken by Canadian Wind Energy Association, 2004.

are solved without any turbulence model. All the spatial scales of the turbulence must be resolved in the computational mesh and no turbulence closure is employed. The Reynolds Averaged Navier-Stokes (RANS) model, which is known since the early work of [65], gives averaged solutions to the Navier-Stokes equations that only mean quantities are described numerically. A turbulence closure scheme is needed to provide additional relationships between some averaged quantities. It can be applied to problems with arbitrarily large Reynolds numbers. Applications of RANS models in wind energy assessment can be found [9] and [25] etc. Large-eddy simulation (LES) is on some middle ground between the DNS and Reynolds-averaged simulations. A local spatial filter is applied to the equations and the numerical simulation gives an description of the large-scale turbulent motions. Applications can be found either in [21], [53], [70], or with some hybrid models in [33], [42].

Throughout this thesis, we consider the RANS models to describe averaged solutions. The ensemble properties of all time fluctuations in the flow are described by a turbulence closure. Many turbulence closures can be used jointly with the RANS models, such as mixing length, $k - \kappa Z$, $k - \varepsilon$, $k - \varepsilon - \tau$, and $q^2 l$ ([4], [54], [47]). Applications of RANS models with the most widely-used $k - \varepsilon$ closure can be found in [16] and [58], model equations are proposed for the Turbulent Kinetic Energy k (TKE) and its dissipation rate ε.

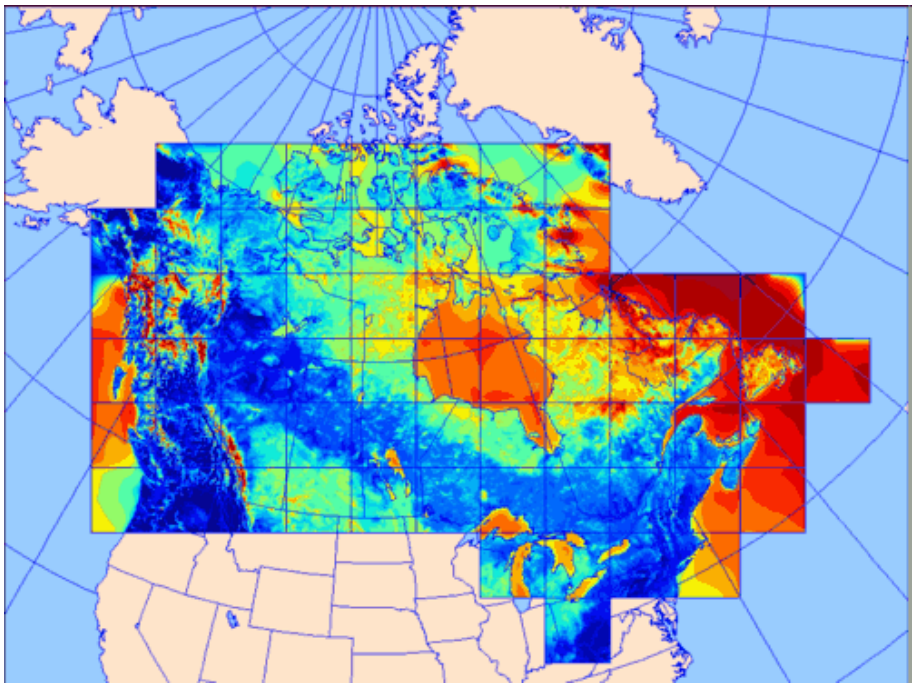

Figure 1.2: Canadian Wind Atlas. Contributed from the EOLE Wind Energy Project, Environment Canada.

1.2 Work of Thesis

Numerical computations of wind flows over topography have recently been playing an important role in the wind energy industry. In this thesis, we study and develop the efficient numerical methods for solving the RANS equations with turbulence closures, and we simulate wind flows over complex topography and turbine wakes of wind farms.

In the first part of the thesis, we first review the models of neutrally stratified turbulence flow over a rough surface with small curvature, which are reviewed in [41], [52], [81], [76], [82], [75], [12], and [49]. The predictions of turbulence variables depend on the closure scheme [77]. [16] has recently used a Mixed Spectral-Integration Model with $k-\varepsilon$ closure. To avoid the limitation of constant advection velocity and simple turbulence closure (mixing-length closure) in MS3DJH, a linearized Mixed Spectral Finite Difference model (MSFD) was developed by [10]. They use a Fourier transform on the horizontal coordinates and finite differences on the vertical coordinate, and [44] improved the numerical treatment for the vertical dimension. However it is still limited to a low slope due to linearization and the assumption that higher order terms are negligible. A non-linear extension (NLMSFD) of this model was then developed by [86] with non-linear terms treated

as additional source terms in an iterative procedure mentioned by [7]. Owing to instability of the iteration scheme, this non-linear mixed spectral finite difference mode (NLMSFD) was limited to a maximum slope of about 0.3. However the choice of relaxation factor can affect the convergence of the iteration scheme. We will show how the relaxation factor can affect the stability and improve the maximum slope for which convergent results can be obtained. We improve this iteration scheme to a much higher maximum slope by adjusting the relaxation factors. We simulate the flows over periodic sinusoidal waves with maximum slope of 0.5 similar to those used by [31] in their wind tunnel study. We find flow separation for both rough and smooth terrain surfaces. In the wind tunnel experiment, the flow remains attached over the smoother surface and separates over the rougher surface. For a realistic application, we use the improved iterative scheme to simulate the wind flow over Bolund hill, which is a field campaign reported by [6], in Denmark.

In the second part of the thesis, we develop an efficient Characteristic Finite Volume (CFV) method for solving the time-dependent RANS equations and $k-\varepsilon$ closure. The CFV scheme is developed by combining the characteristic method and the finite volume method ([59], [57], [55]). The numerical solutions of the time-dependent RANS equations are not easy to compute because of the dominance of the nonlinear convective term and the topography structure. In order to resolve the

dominance of the convective term, we take the significant advantage of the characteristic method to efficiently and accurately solve the time-dependent Reynolds Averaged Navier-Stokes (RANS) equations and the coupled $k - \varepsilon$ equations. The characteristic method approximates the derivative of temporal and convection discretization directly. Along characteristics, the solution changes much slower than along the original time direction. Hence it is computationally efficient that we can use large time steps and get more accurate results. The characteristic finite volume scheme is developed to solve the RANS equations and the coupled energy equations. Numerical experiments will focus on two-dimensional topography. Numerical examples of flow over two-dimensional flat terrain and complex terrain such as cliff and blocks are tested. The first test is flow over flat terrain, we compare results from the CFV scheme and a regular Euler time scheme. It shows the advantages of the accuracy and stability of the CFV method in large time steps. Complex terrains are then tested, which show that our method can be applied to flow over various terrain shape and roughness. Finally, the CFV method is applied to a realistic terrain wind flow over the Bolund hill in Denmark. Simulation results are in good agreement with field measurements by [11], [8].

In the third part of the thesis we apply the CFV to model wind flow and turbine wakes of large wind farms. The roughness change models of RANS equa-

tions with $k - \varepsilon$ closure solved by the CFV method are developed to predict the wind speed reduction and recovery within and downwind of the wind farm. Several approaches have been applied in [18], [25], [26]. We consider the effects of the infinitely large wind farm as a higher surface roughness than the surroundings. An empirical formula is derived to calculate the roughness of wind farms based on the terrain roughness. The prediction of turbine wakes is useful on deciding the distance between wind farms in order to maximize the potential energy which can be captured. The recovery of the wind speed on the downwind side of the wind farm will be computed. We simulate the wind turbine wakes behind a cluster of wind farms which take into account the roughness change on the topography. We propose to simulate RANS models with Coriolis Effect to predict wind flows in a large wind farm due to the rotation of Earth. The wind flows within and downwind of the wind farms are studied numerically. Simulation results on the Horns Rev wind farm are compared with field measurements.

2 Relaxation Factor Effects in NLMSFD Model and Applications of Flow Over Topographic Features

A linearized Mixed Spectral Finite Difference model (MSFD) developed by [10] used a Fourier transform on the horizontal coordinates and finite differences on the vertical coordinate, and [44] improved the numerical treatment for the vertical dimension. This model can operate with various closure schemes such as $E - \kappa Z$, $E - \varepsilon$, $E - \varepsilon - \tau$, and $q^2 l$, and better predict turbulence variables as noted by [4] (The Turbulence Kinetic Energy term E is also known as k in other literatures and Chapters of this thesis. In this Chapter we use E in order to distinct from the Fourier wave number k). A non-linear extension (NLMSFD) of this model was then developed by [86] with non-linear terms treated as additional source terms in an iterative procedure mentioned by [7]. This non-linear version of the MSFD model experienced difficulties on stability of the iteration scheme. Especially for

the complex terrain with a maximum slope of 0.3 or greater. In this Chapter, the relations between the stability of the iteration scheme and its relaxation parameter are discussed. Suitable choice of the relaxation factor will improve the computational stability on terrain with maximum slope up to 0.5 or 0.6 in certain circumstances. Examples of relatively high slope terrain are used to test the stability under a two-dimensional manner. By setting a smaller relaxation parameter than had previously been used we are able to calculate flow over complex terrain with a relatively high slope. The stability of the non-linear iteration scheme also depends on the roughness length (z_0) of the terrain, a larger roughness length (z_0) gives better convergence. Tests of the NLMSFD model give reasonable results on terrain with relatively high maximum slope and successfully predicted the flow separation in the wind-tunnel experiment. The choice of different relaxation factors does not affect the results, assuming the relaxation parameter is small enough to ensure numerical stability. The application on Bolund hill shows the potential of NLMSFD on a real topography with high maximum slope up to 0.77.

2.1 Steady-state RANS model with $E - \kappa Z$ Closure

In this section we test the effects of relaxation factor from the Non-linear MSFD model. The two-dimensional steady-state Reynolds Averaged Navier-Stokes (RANS) equations and $E - \kappa Z$ closure are used. Two-dimensional governing equations and

$E-\kappa Z$ closure can be found in [75] under Cartesian coordinates (x,z), details of RANS equations will be discussed in next chapter. The steady state Reynolds-averaged momentum, continuity, and turbulence kinetic energy (TKE) equations for incompressible flow are

$$\begin{aligned}
U\frac{\partial U}{\partial x}+W\frac{\partial U}{\partial z} &= -\frac{\partial P}{\partial x}-\frac{\partial \overline{uu}}{\partial x}-\frac{\partial \overline{uw}}{\partial z}, && (2.1)\\
U\frac{\partial W}{\partial x}+W\frac{\partial W}{\partial z} &= -\frac{\partial P}{\partial z}-\frac{\partial \overline{uw}}{\partial x}-\frac{\partial \overline{ww}}{\partial z}, && (2.2)\\
\frac{\partial U}{\partial x}+\frac{\partial W}{\partial z} &= 0, && (2.3)\\
U\frac{\partial E}{\partial x}+W\frac{\partial E}{\partial z} &= -\overline{uu}\frac{\partial U}{\partial x}-\overline{uw}\frac{\partial U}{\partial z}-\overline{uw}\frac{\partial W}{\partial x}-\overline{ww}\frac{\partial W}{\partial z}\\
&\quad -\varepsilon+\frac{\partial}{\partial x}\left(K\frac{\partial E}{\partial x}\right)+\frac{\partial}{\partial z}\left(K\frac{\partial E}{\partial z}\right). && (2.4)
\end{aligned}$$

Coriolis terms are omitted in the basic atmospheric surface layer context. Mean flow variables (U,W,P) are generally denoted by upper case and turbulent fluctuations u,v,w et al. by lower case symbols. $E=\frac{1}{2}(\overline{uu}+\overline{vv}+\overline{ww})$ is the turbulence kinetic energy, ε is the mean dissipation rate of TKE and K is eddy viscosity. Using an isotropic form for eddy viscosity, we have,

$$\begin{aligned}
\overline{uu} &= \frac{2}{3}E-K\left(\frac{\partial U}{\partial x}-\frac{\partial W}{\partial z}\right), && (2.5)\\
\overline{ww} &= \frac{2}{3}E-K\left(\frac{\partial W}{\partial z}-\frac{\partial U}{\partial x}\right), && (2.6)\\
\overline{uw} &= -K\left(\frac{\partial U}{\partial z}+\frac{\partial W}{\partial x}\right). && (2.7)
\end{aligned}$$

To close the system we also assume, with $E - \kappa Z$ closure

$$\varepsilon = \frac{(\alpha E)^{3/2}}{\ell}, \tag{2.8}$$

$$K = \ell(\alpha E)^{1/2}, \tag{2.9}$$

where the constant $\alpha = 0.25$ is the equilibrium ratio of surface shear stress to the turbulent kinetic energy and ℓ is the turbulence length scale. In the simple surface layer model of the lower atmospheric boundary layer we take

$$\ell = \kappa \left(z - z_s + z_0 \right), \tag{2.10}$$

with von Karman constant $\kappa = 0.4$, constant surface roughness z_0, and terrain surface $z_s(x)$. Equations are solved in a non dimensional framework using z_0 and u_* (the friction velocity for the undisturbed flow) as length and velocity scales respectively.

Boundary conditions on the surface are given as non-slip conditions for velocity and we assume that production balances dissipation of turbulence kinetic energy at the surface. Upper boundary conditions at $Z = H$ assume that vertical derivatives of mean variable perturbations are zero and perturbations of all turbulent quantities are zero. By fixing perturbed shear stress to be zero and allowing U to vary we are applying a fixed shear stress at the upper boundary. Because the surface topography causes a form drag on the flow this will lead to a reduction of U at the

upper boundary relative to flow over the flat surface.

The lower boundary is at $z = z_s(x)$ and a coordinate transform is used as,

$$X = x, \tag{2.11}$$

$$Z = z - z_s(x). \tag{2.12}$$

Another vertical coordinate transform

$$\eta = \ln\left(\frac{Z}{z_0} + 1\right), \tag{2.13}$$

is used later in the computations to ensure sufficient resolution near the surface. Lateral boundary conditions (in X) are simply that the flow is periodic –one of the limitation of the use of Fourier transform methods. The terrain $z_s(x)$ must also be periodic and the domain used covers just one wavelength.

2.2 Non-linear MSFD Method

Equations (2.1) to (2.9) are solved numerically based on the method presented on [10]. All unknown variables are split into unperturbed terms and perturbation

terms along the X direction,

$$
\begin{aligned}
U(X,Z) &= U_0(Z) + U_1(X,Z), && (2.14)\\
W(X,Z) &= (U_0(Z) + U_1(X,Z))\frac{\partial z_s}{\partial x} + W_1(X,Z), && (2.15)\\
P(X,Z) &= P_0(Z) + P_1(X,Z), && (2.16)\\
E(X,Z) &= E_0(Z) + E_1(X,Z), && (2.17)\\
\overline{uu}(X,Z) &= \overline{uu}_0(Z) + \overline{uu}_1(X,Z), && (2.18)\\
\overline{ww}(X,Z) &= \overline{ww}_0(Z) + \overline{ww}_1(X,Z), && (2.19)\\
\overline{uw}(X,Z) &= \overline{uw}_0(Z) + \overline{uw}_1(X,Z), && (2.20)\\
\varepsilon(X,Z) &= \varepsilon_0(Z) + \varepsilon_1(X,Z), && (2.21)\\
K(X,Z) &= K_0(Z) + K_1(X,Z), && (2.22)
\end{aligned}
$$

where the unperturbed terms are scaled by friction velocity u_*,

$$U_0(X,Z) = \frac{1}{\kappa}\ln\left(\frac{Z}{z_0}+1\right), \tag{2.23}$$

$$P_0(X,Z) = 0, \tag{2.24}$$

$$E_0(X,Z) = \frac{1}{\alpha}, \tag{2.25}$$

$$\overline{uu}_0(X,Z) = \frac{2}{3\alpha}, \tag{2.26}$$

$$\overline{ww}_0(X,Z) = \frac{2}{3\alpha}, \tag{2.27}$$

$$\overline{uw}_0(X,Z) = -1, \tag{2.28}$$

$$\varepsilon_0(X,Z) = \frac{1}{\kappa\left(\frac{Z}{z_0}+1\right)}, \tag{2.29}$$

$$K_0(X,Z) = \kappa\left(\frac{Z}{z_0}+1\right), \tag{2.30}$$

where $\alpha = 0.25$. Combining the variable decomposition and the coordinates transform, we can re-write the above differential equations. For example, the derivatives with respect to x and z become,

$$\frac{\partial U}{\partial x} = -\frac{\partial U_0}{\partial Z}\frac{\partial z_s}{\partial X} + \frac{\partial U_1}{\partial X} - \frac{\partial U_1}{\partial Z}\frac{\partial z_s}{\partial X}, \tag{2.31}$$

$$\frac{\partial U}{\partial z} = \frac{\partial U_0}{\partial Z} + \frac{\partial U_1}{\partial Z}. \tag{2.32}$$

Thus Equation (2.1) can be updated by arranging the linear terms to the left hand side and non-linear terms to the right hand side.

$$U_0\frac{\partial U_1}{\partial X} + W_1\frac{\partial U_0}{\partial Z} + \frac{\partial P_1}{\partial X} + \frac{\partial \overline{uu}_1}{\partial X} + \frac{\partial \overline{uw}_1}{\partial Z} = -U_1\frac{\partial U_1}{\partial X} - W_1\frac{\partial U_1}{\partial Z} + \frac{\partial P_1}{\partial Z}\frac{\partial z_s}{\partial X} + \frac{\partial \overline{uu}_1}{\partial Z}\frac{\partial z_s}{\partial X} \equiv R_1. \tag{2.33}$$

After the variable decomposition, we apply the Fourier transform on linear terms from the left hand side of Equation (2.33) with respect to the horizontal directions (X direction in the 2-D case).

$$\hat{U}_1(k) = \frac{1}{2\pi}\int_{-\infty}^{\infty} U_1(X)e^{-ikX}dX. \tag{2.34}$$

Hence the partial differential equations can be reduced to the ordinary differential equations with respect to the vertical direction Z. For example Equation (2.33) becomes,

$$ikU_0\hat{U}_1 + U_0'\hat{W}_1 + ik\hat{P}_1 + ik\widehat{uu}_1 + \frac{d}{dZ}\widehat{uw}_1 = R_1. \tag{2.35}$$

Apply the same treatment from Equations (2.1) to (2.9) we can obtain the following system,

$$\overrightarrow{L}(\widehat{\Phi}) = \widehat{\overrightarrow{R}(\Phi)}, \tag{2.36}$$

with first order terms in a linear system on the left hand side of Equation (2.36) and higher order source terms on the right hand side of Equation (2.36). $\widehat{\Phi}$ represents 9 unknowns,

$$\widehat{\Phi} = [\hat{U}_1,\ \hat{W}_1,\ \hat{P}_1,\ \hat{E}_1,\ \widehat{\overline{uu}}_1,\ \widehat{\overline{ww}}_1,\ \widehat{\overline{uw}}_1,\ \hat{\varepsilon}_1,\ \hat{K}_1]^T, \tag{2.37}$$

and hats denote a Fourier transform with respect to X. To solve the non-linear system in Equation (2.36), an under-relaxation iteration scheme from [7] is used as

follows,

$$\begin{aligned} \overrightarrow{L}(\widehat{\Phi}^*) &= \overrightarrow{\widehat{R}(\Phi^{(n-1)})}, \\ \widehat{\Phi}^{(n)} &= \omega\widehat{\Phi}^* + (1-\omega)\widehat{\Phi}^{(n-1)}. \end{aligned} \tag{2.38}$$

The stability of this scheme depends on the selection of relaxation factor ω. For given topography, most cases with moderate ω failed for terrain with a maximum slope greater than 0.3. A smaller relaxation factor is time consuming but will give a more stable iteration as shown in the example below.

The boundary conditions used for this case are given in following. On the

lower boundary where $z = z_s(x)$ or $Z = 0$ we have,

$$U = 0, \tag{2.39}$$

$$W = 0, \tag{2.40}$$

$$\frac{\partial P}{\partial Z} = 0, \tag{2.41}$$

$$0 = -\overline{uu}\frac{\partial U}{\partial X} - \overline{uw}\frac{\partial U}{\partial Z} - \overline{uw}\frac{\partial U}{\partial X} - \overline{ww}\frac{\partial W}{\partial Z} - \varepsilon, \tag{2.42}$$

$$\overline{uu} = \frac{2}{3}E - K\left(\frac{\partial U}{\partial X} - \frac{\partial W}{\partial Z}\right), \tag{2.43}$$

$$\overline{ww} = \frac{2}{3}E - K\left(\frac{\partial W}{\partial Z} - \frac{\partial U}{\partial X}\right), \tag{2.44}$$

$$\overline{uw} = -K\left(\frac{\partial U}{\partial Z} + \frac{\partial W}{\partial X}\right), \tag{2.45}$$

$$\varepsilon = \frac{(\alpha E)^{3/2}}{\ell}, \tag{2.46}$$

$$K = \ell(\alpha E)^{1/2}. \tag{2.47}$$

On the upper boundary where $z = H + z_s(x)$ or $Z = H$ we have,

$$U\frac{\partial U}{\partial X} + W\frac{\partial U}{\partial Z} = -\frac{\partial P}{\partial X} - \frac{\partial \overline{uu}}{\partial X} - \frac{\partial \overline{uw}}{\partial Z}, \tag{2.48}$$

$$P = 0, \tag{2.49}$$

$$\frac{\partial U}{\partial X} + \frac{\partial W}{\partial Z} = 0, \tag{2.50}$$

$$\overline{uu} = \overline{uu}_0, \tag{2.51}$$

$$\overline{ww} = \overline{ww}_0, \tag{2.52}$$

$$\overline{uw} = \overline{uw}_0, \tag{2.53}$$

$$\varepsilon = \frac{(\alpha E)^{3/2}}{\ell}, \tag{2.54}$$

$$K = \ell(\alpha E)^{1/2}. \tag{2.55}$$

2.3 Tests on Relaxation Factor

In the following tests, a two-dimensional periodic sinusoidal terrain is given as

$$z_s(x) = a\cos(kx), \tag{2.56}$$

where $k = 2\pi/L$, L is the wavelength, and the maximum slope is ak. Different roughness length are used for comparison with $L/z_0 = 10^3,\ 10^4,\ 10^5,\ 10^6$. The domain used has height of $2L$ and length of L. A typical value of L would be 1000 m with z_0 ranging from 1 mm to 1 m depending on the nature of the surface. A total number of 129 horizontal grid points and 101 vertical grid points are used in

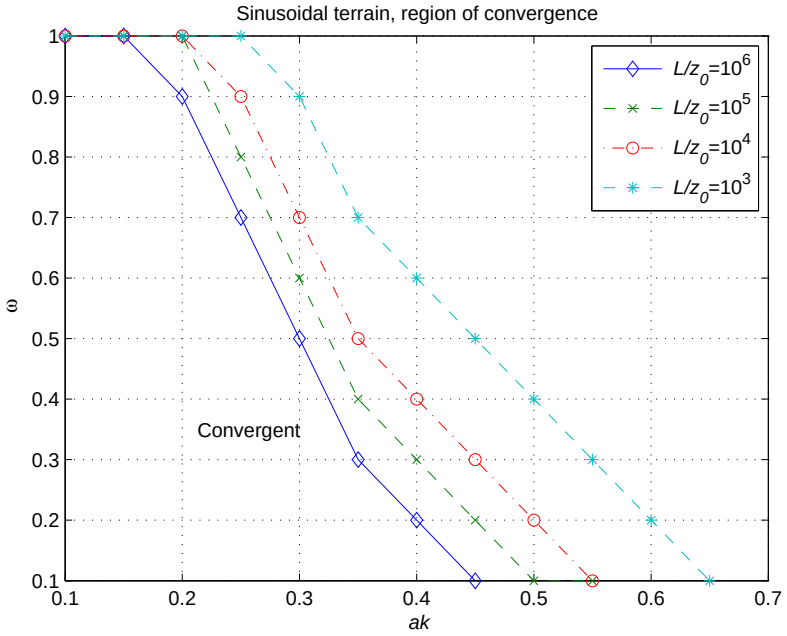

Figure 2.1: Region of convergence.

our computation.

In each test, the relative error of normalized surface shear stress $-\overline{uw}$ (RESS) before relaxation is used as criterion of convergence,

$$\text{RESS} \equiv \frac{\left\| \overline{uw}^{(*)}(\vec{X},0) - \overline{uw}^{(n)}(\vec{X},0) \right\|_2}{\left\| \overline{uw}^{(n)}(\tilde{X},0) \right\|_2} < \delta, \tag{2.57}$$

where δ is set as 2×10^{-3} and $\|\cdot\|_2$ denotes the L_2 norm. We investigate the stability of the method for various ak and ω. Figure 2.1 is an (ak,ω) domain plot for the region of convergence which is bounded above by lines for different L/z_0 values. From Figure 2.1 we find that the convergent region in (ak,ω) space is largest for the rougher surface cases where, for a maximum slope $ak = 0.65$ we could obtain

convergence with $\omega = 0.1$, while if $\omega = 0.5$ the iteration can only converge for a maximum slope $ak = 0.45$. Similarly when $L/z_0 = 10^6$, we have the smallest region of convergence and can only reach a maximum slope $ak = 0.45$ for $\omega = 0.1$. Even smaller relaxation factors such as $\omega = 0.05$ have also been tested but they are not plotted in Figure 2.1. In Figure 2.2 we show changes of errors under cases of convergence and divergence when $ak = 0.55$ and $L/z_0 = 10^3$. The y-axis is arranged under a logarithm scale in order to show the error pattern. By using a small relaxation parameter, Figure 2.2(a) shows the convergence of the iteration scheme for a relatively high maximum slope. Figure 2.2(b) shows a case of rapid divergence during the iteration.

We also tested cases when the vertical domain $H = L$ and $H = 4L$. Results of (ak, ω) plots show that there is little difference between these cases, and when $H = 2L$. The convergence of the iteration scheme is not sensitive to the choice of vertical domain height. Tests on other topographies such as Cosine square or Bell shape terrain showed similar behaviors.

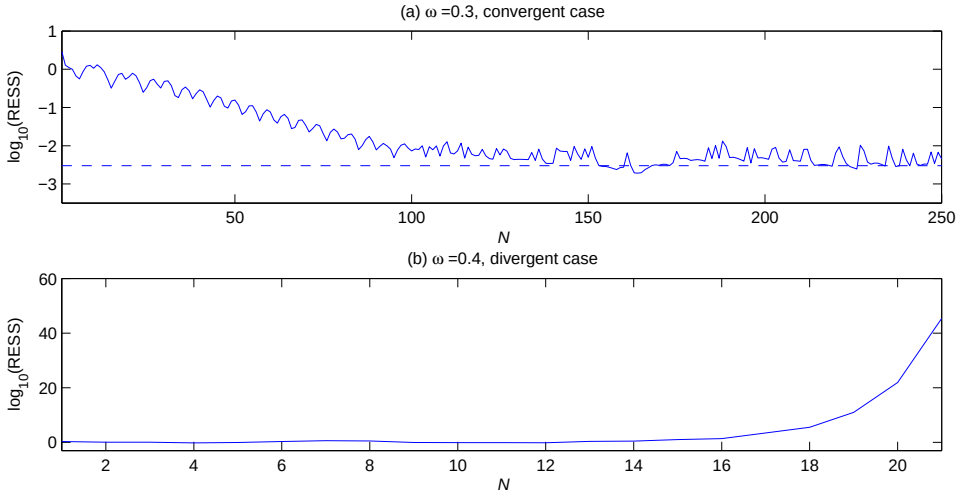

Figure 2.2: Related error of normalized surface shear stress in N steps, ak=0.55, $L/z_0 = 10^3$, (a) $\omega = 0.3$. (b) $\omega = 0.4$.

2.4 Comparisons with a wind tunnel study of flow over a sinusoidal wavy surface.

Flow over a two-dimensional periodic sinusoidal surface was studied in a wind tunnel by [31] for relatively smooth and rough surfaces. In their experiment a neutrally stratified flow is presented. They observed that flow separates in the rough case and generally remains attached in the smooth case. In the smooth case a secondary three-dimensional flow develops. This has longitudinal vortices aligned with the flow. We concentrate on their results from one period of the sinusoidal wave between the 11th and 12th trough in a wave train. The flow is essentially periodic

at this stage and periodic boundary conditions can be applied in the horizontal direction.

We use this case to test the NLMSFD model for a relatively steep slope with $E - \kappa Z$ closure. Vertical boundary conditions are applied as mentioned in the previous section. The periodic surface function is defined by Equation (2.56), where $k = 2\pi/\lambda$. In the wind tunnel, the terrain height was set to be $2a = 96.5$ mm, wavelength $\lambda = 609.6$ mm, thus the maximum slope is $ak = 0.5$. In our model we set the upper boundary at $Z = H = 1200$ mm, roughly 2λ. The two surfaces used in the wind tunnel had $z_0 = 0.4$ mm with a carpet cover and $z_0 = 0.03$ mm with the basic Masonite floor.

During the computation, periodic boundary conditions are applied on $x/\lambda = -0.5$ and $x/\lambda = 0.5$, and lower and upper boundary conditions are applied on $Z = 0$ mm and $Z = 1200$ mm. The NLMSFD model converges with relatively small relaxation factors ($\omega = 0.3$ for the rough case and $\omega = 0.2$ for the smooth case). In Figure 2.3, we compare velocity profiles at different locations (trough, midway upwind, crest, midway downwind). Our model results are normalized by the velocity at height λ. Wind tunnel data are normalized by a free-stream velocity, which was attained at $Z = \lambda$.

Although the general pattern of speed increases over the crest and decreases in the trough is the same in both cases we can see that the wind tunnel speed increases in the relatively smooth wall case are much larger than in the rough case. The NLMSFD model matches the wind tunnel results in the rough wall case reasonably well, especially considering that the wind tunnel boundary layer is roughly of depth λ while the model assumes a very deep constant stress layer as the background flow. Also note that the hot wire methodology used by [31] could not measure the reverse flow near the surface over the trough, although flow separation was observed in the rough wall case.

In the smooth wall case the model fails to predict the strong near-surface jet measured over the crest and wind speeds below $Z = \lambda$ are generally lower than those measured in the wind tunnel. This may be in part because the wind tunnel flow remained attached while the model predicts flow separation in the trough, which effectively reduces the steepness of the terrain seen by the outer flow. Model tests with a smoother surface ($z_0 = 0.01$ mm) have also been run and flow separation still occurred.

A factor which could cause model/wind tunnel differences in the smoother wall

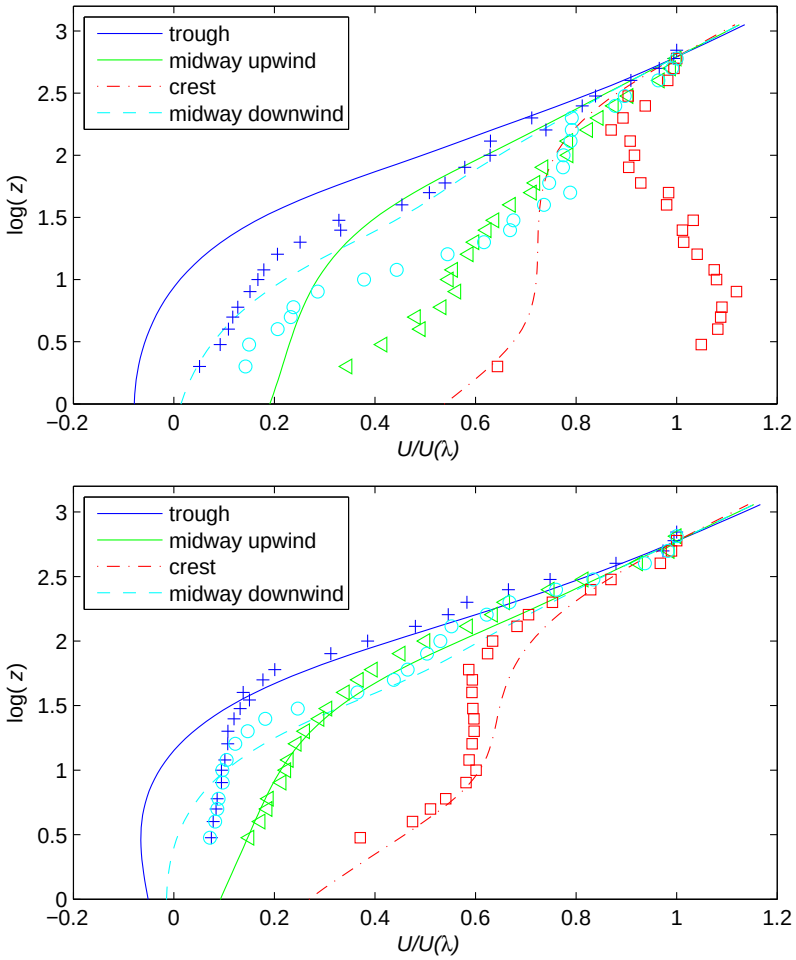

Figure 2.3: Comparison of model results and experimental data from Gong et al (1996), (a) $z_0 = 0.03$ mm (b) $z_0 = 0.4$ mm. Vertical results are plotted versus $\log(Z)$ where Z is in mm. x-direction velocity U is scaled by $U(\lambda)$. Line segments are model results and measurement data are given as: (+) trough, ($\triangleleft$) midway upwind, ($\square$) crest, (O) midway downwind.

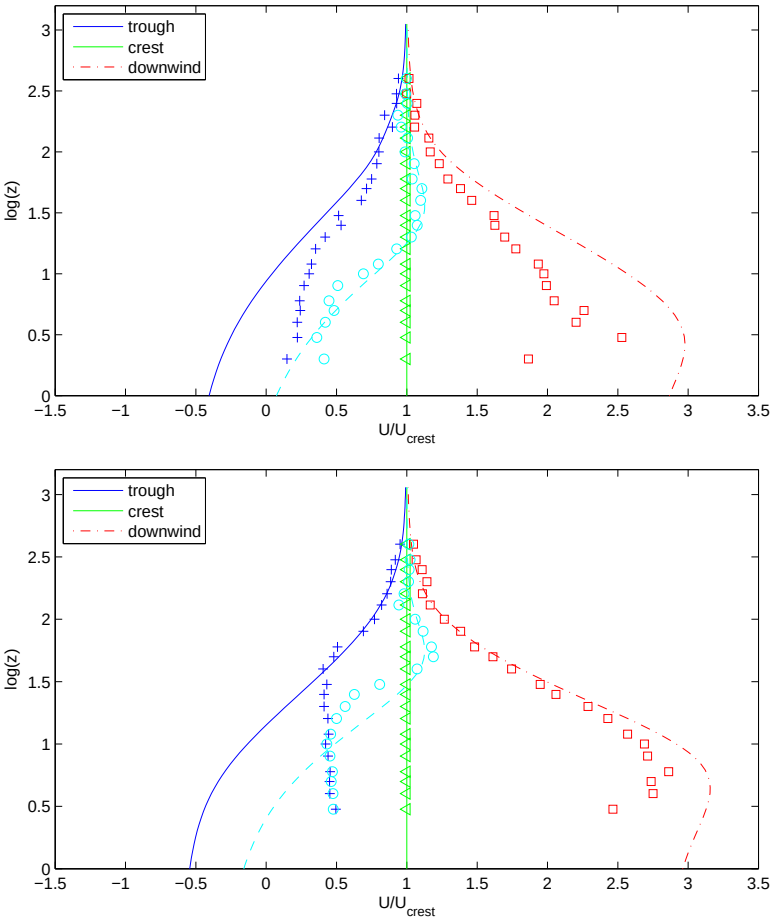

Figure 2.4: Comparison of model results and experimental data from Gong et al (1996), results are normalized by velocity at hill crest, (a) $z_0 = 0.03$ mm (b) $z_0 = 0.4$ mm. Vertical results are plotted versus $\log(Z)$ where Z is in mm. x-direction velocity U is scaled by $U(\lambda)$. Line segments are model results and measurement data are given as: (+) trough, ($\triangleleft$) midway upwind, ($\square$) crest, (O) midway downwind.

case is the fact that the three-dimensional longitudinal vortices are not represented in our two-dimensional model. The absence of roll vortices may cause the different results and flow separation. These vortices may play a role in transferring momentum down towards the surface and inhibiting flow separation. Initial studies by [78] were unsuccessful in establishing this but further study with three-dimensional models is planned. Therefore we will focus on the rough wall case in the rest of this paper.

In Figure 2.3(b) we can find good result on the wave crest between the experiment data and model results. When $\log(Z) < 1.5$, with Z in mm, different results are shown on wave trough and midway downwind. Since the measurement data cannot distinguish the direction of the flow, when flow separates, horizontal velocities do not give negative values in the rough wall case. Results from the NLMSFD model show that flow separates in the wave trough. Thus in Figure 2.3(b), the normalized speed-up ratio of model results are negative over the trough and midway downwind while measured data are not conclusive. Normalized results are also given in Figure 2.4.

In Figure 2.5 surface pressure is compared over one period, and normalized by $P/\rho U_{ref}^2$ where the reference velocity U_{ref} is taken as $U(\lambda/4)$ which is horizontally averaged. In the rough wall case model result and measurement data show fair

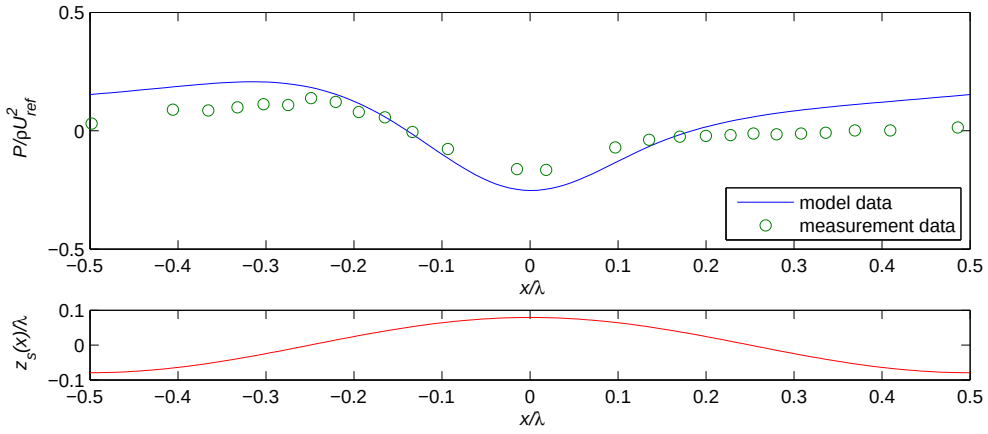

Figure 2.5: Surface pressure scaled by ρU_{ref}^2 (rough wall case).

agreement and it should be noted that measuring static pressure through small holes in the carpet covered floor may be inaccurate. Contour plots of modelled E/u_*^2 and $-u\bar{w}/u_*^2$ are given in Figure 2.6 and Figure 2.7 for the region close to surface. Perturbations in the upper region are nearly zero since $E_0/u_*^2 = 4$ and $-\overline{uw}_0/u_*^2 = 1$. The y axis scale is stretched rather than a 1:1 ratio in order to show patterns clearly.

It was previously stated that recirculation was not observable in the experiments due to equipment limitations. In order to show the region of flow separation, we further calculate the stream function ϕ with

$$U = \frac{\partial \phi}{\partial z}. \tag{2.58}$$

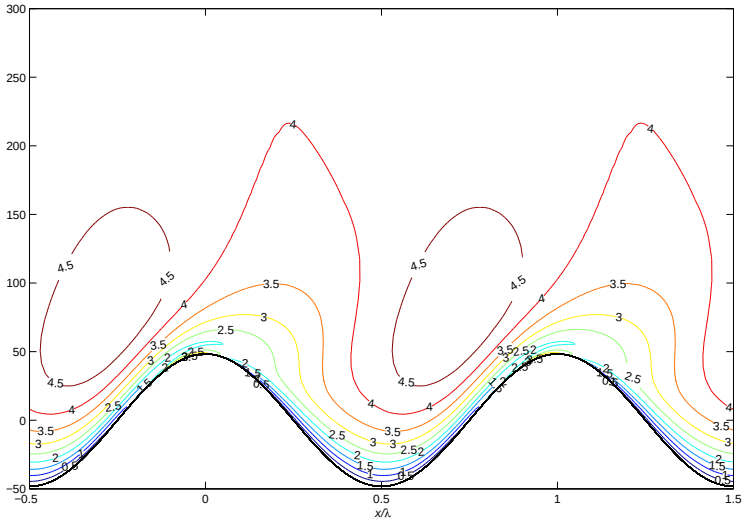

Figure 2.6: Contour plot of E/u_*^2 over two periods, $z_0 = 0.4$ mm.

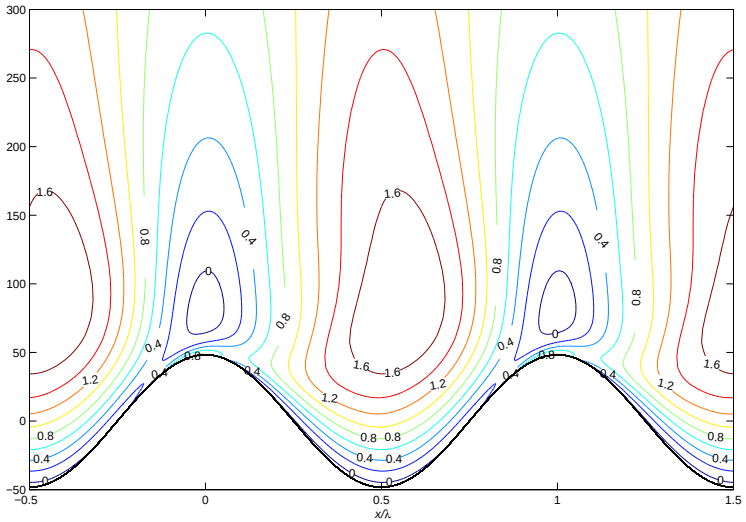

Figure 2.7: Contour plot of $-\overline{uw}/u_*^2$ over two periods, $z_0 = 0.4$ mm.

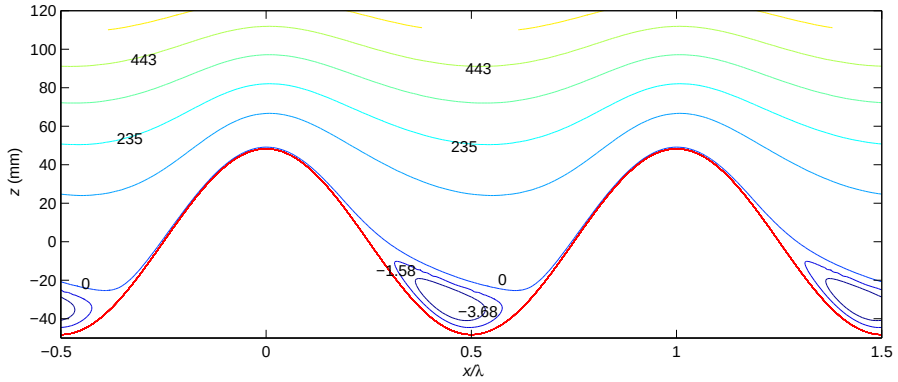

Figure 2.8: Contour plot of the stream function in the lower part of the domain when $z_0 = 0.4$mm.

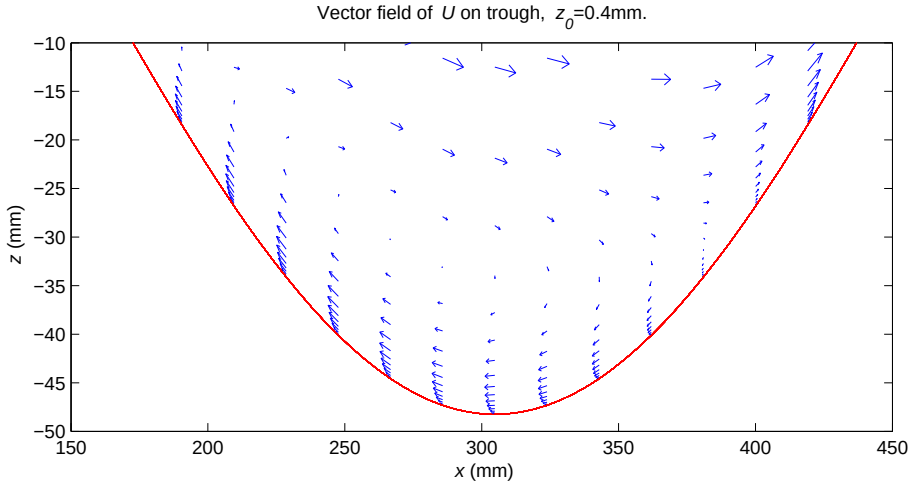

Figure 2.9: Velocity vector field in the lower part of the domain when $z_0 = 0.4$mm.

Contour plots of ϕ and velocity vector field are given in Figure 2.8 and Figure 2.9. NLMSFD predicts a large region of flow separation in the rough wall case, which is also observed in wind tunnel experiment. The separation zone in the rough wall case is about 270 mm in length and 24 mm in depth over trough from model results. The relatively good agreement in the rough wall case and lack of agreement in the smooth wall case supports the view that the three-dimensional longitudinal vortices observed in the wind tunnel by [31] may play an important role in momentum transfer and in inhibiting flow separation in the smooth wall case.

2.5 Application to Bolund hill

The Bolund experiment is a field campaign run by the Risø National Laboratory for Sustainable Energy, Technical University of Denmark (DTU), Denmark. It was conducted in 2007 and 2008 and reported by [6].

In Figure 2.10, the terrain of Bolund hill has a dimension of 12m in height, 130m in length, 75m in width. It is located north of Risø DTU. A steep edge occurs on the western side of the hill with a maximum slope around 1.2. Surface roughness also changes sharply from the water surface to a land surface. Two roughness are used as $z_0 = 0.015$ m for grassland and $z_0 = 0.0003$ m for water surface. Ten masts,

Figure 2.10: Photo of Bolund hill from [6]

M0 to M9 (see Figure 2.11) were used to collect wind data. There were four simulation cases for the blind comparison of Bolund experiment, the first three cases are wind from west with directions of 270°, 255°, and 239°, the fourth case is wind from east with direction of 90°. The locations of the masts are listed in Table 2.1.

Owing to the limitation of our two-dimensional model, we simulated only case 1, case 3, and case 4 on cross-sections of Bolund hill, which are along lines A and B in Figure 2.11. First, we present our results from case 1, where the friction velocity is set to be $u_* = 0.4$ ms^{-1}, and upstream turbulence kinetic energy (TKE)

Table 2.1: The locations of the masts

Mast ID	x [m]	y [m]	Ground level [m]
M0	-180.832	-103.267	0.75
M1	-52.426	-30.987	0.78
M2	-34.840	-21.110	10.80
M3	3.220	0.000	11.66
M4	51.458	30.612	1.37
M5	1.502	-48.926	2.59
M6	-46.121	0.242	11.47
M7	-66.887	0.016	0.81
M8	92.009	-0.136	2.00
M9	327.326	-39.296	0.75

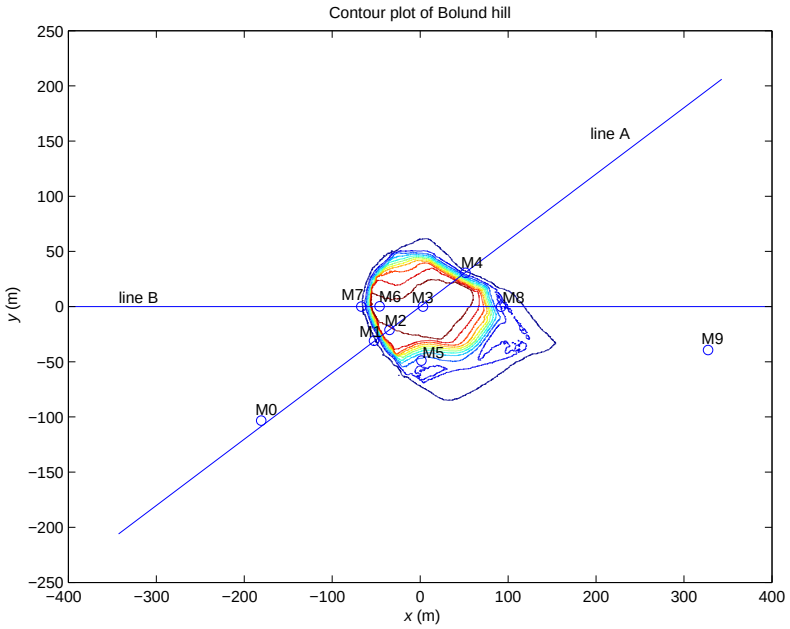

Figure 2.11: Contour plot of Bolund hill (re-plotted from data provided by [6])

Table 2.2: The four simulation cases

Case	Wind direction [°]	Roughness length z_0 [m]	Ground level [m]	TKE_0/u_{*0}^2 [-]	u_{*0} [m/s]
1	270	0.0003	0.75	5.8	0.4
2	255	0.0003	0.75	5.8	0.4
3	239	0.0003	0.75	5.8	0.4
4	90	0.015	0.75	5.8	0.5

$E_0/u_*^2 = 5.8$. Details of each case setup can be found in Table 2.2. A roughness length of $z_0 = 0.0003$ m is used here for all computations since the upstream flow is over a water surface. Because the Bolund hill has a steep edge that will effect the stability of our iteration, a surface smoothing technique is also used to smooth the terrain from actual maximum slope of 1.1 to 0.77 for case 1.

[41] and others have used the concept of speed-up, S, and a "fractional speed-up ratio", ΔS, relative to an undisturbed upstream flow to characterize wind speed increases caused by topography

$$\Delta S = \frac{U(X,Z)}{U_0(Z)} - 1. \tag{2.59}$$

Roughness change effects can be considered separately using results from a planetary boundary-layer (PBL) model in [85]. Here we let

$$U = U_0(Z)\left(\frac{1+\Delta S_t(X,Z)}{1+\Delta S_t(-400,Z)} + \Delta S_r(X,Z)\right), \tag{2.60}$$

where $U_0(Z)$ is the equilibrium profile over water, ΔS_t is fractional speed-up ratio for terrain change from the NLMSFD model, and ΔS_r is fractional speed-up ratio for roughness change from PBL model. The appearance of $\Delta S_t(-400, Z)$ is to compensate for the use of periodic boundary condition. A total of 256 wavenumbers are used in the X-direction and 81 grid points in Z after a logarithm transformation. This is a first attempt to couple the effects of terrain shape change and roughness change. Values of normalized ΔS_t and ΔS_r in case 1, 3, and 4 are given in Figures 2.12, 2.13, and 2.14.

We can observe that for roughness change, the fractional speed-up ratio is negative when flow passes from sea to Bolund island. The wind speeds up downwind of the island and slows again when flow hits land west of x=320 m. For terrain change, the fractional speed-up ratio changes sharply at the hill edge and smoothly over the hill top.

In Figures 2.15, 2.16, and 2.17, we present the normalized surface velocity at two different heights, 2 metres from surface and 5 metres from surface. The total

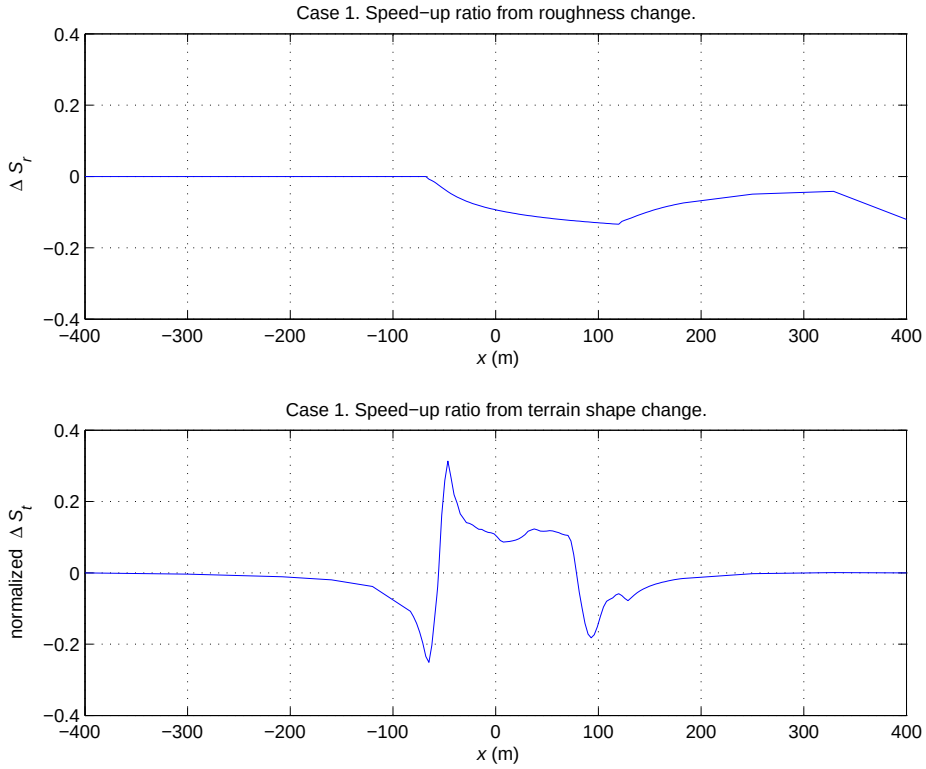

Figure 2.12: Fractional speed-up ratio in case 1, 2 metres from surface.

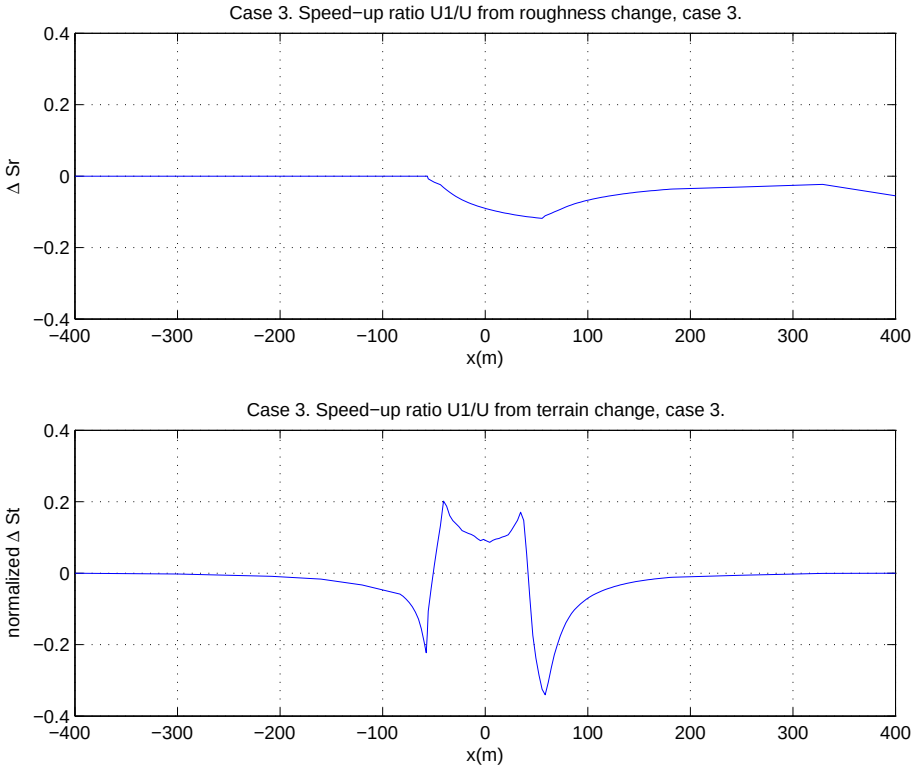

Figure 2.13: Fractional speed-up ratio in case 3, 2 metres from surface.

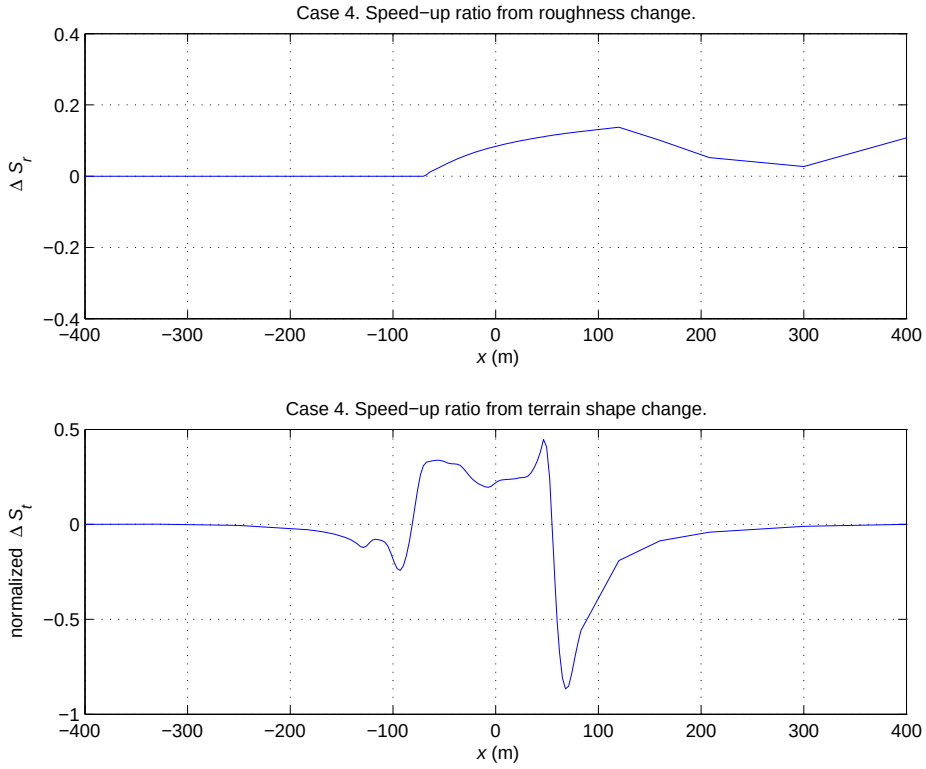

Figure 2.14: Fractional speed-up ratio in case 4, 2 metres from surface.

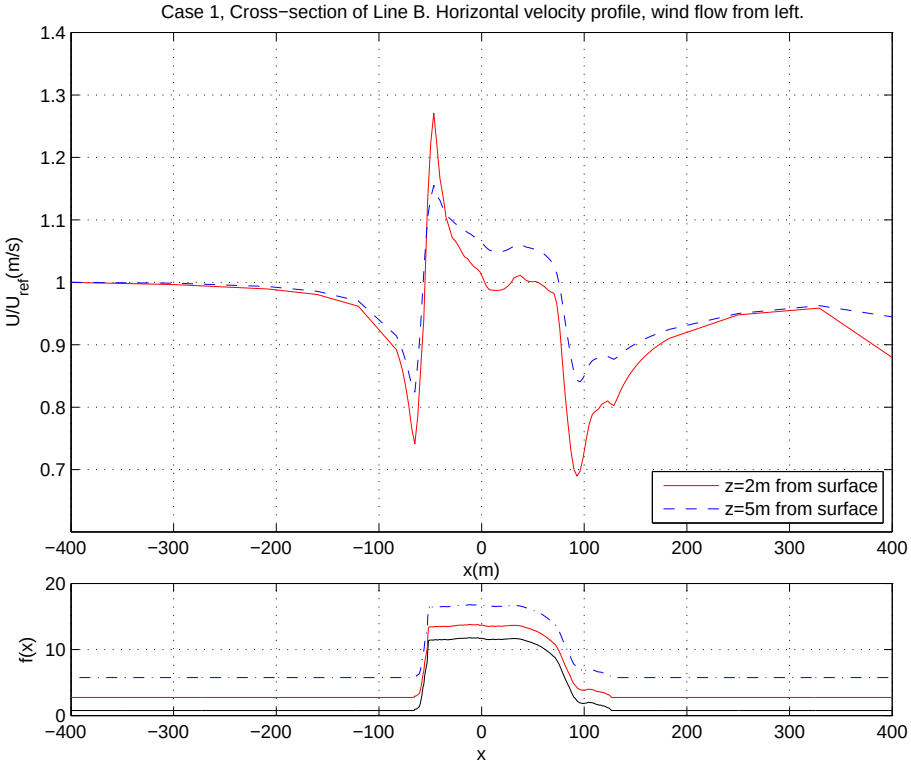

Figure 2.15: Case 1. Surface velocity on Line B.

velocity s (wind speed) is defined by

$$s = (U^2 + V^2 + W^2)^{1/2}, \tag{2.61}$$

and we use the upstream velocity as the reference velocity s_{ref}. Field measurements are compared with the model data for case 1 and case 3 in Figures 2.18 and 2.19. Since a smoothing technique is applied to the hill terrain, there are under-predictions of wind speed reductions on the lee side but fair agreement with observations on the hill top five metres from the surface. For two metres from

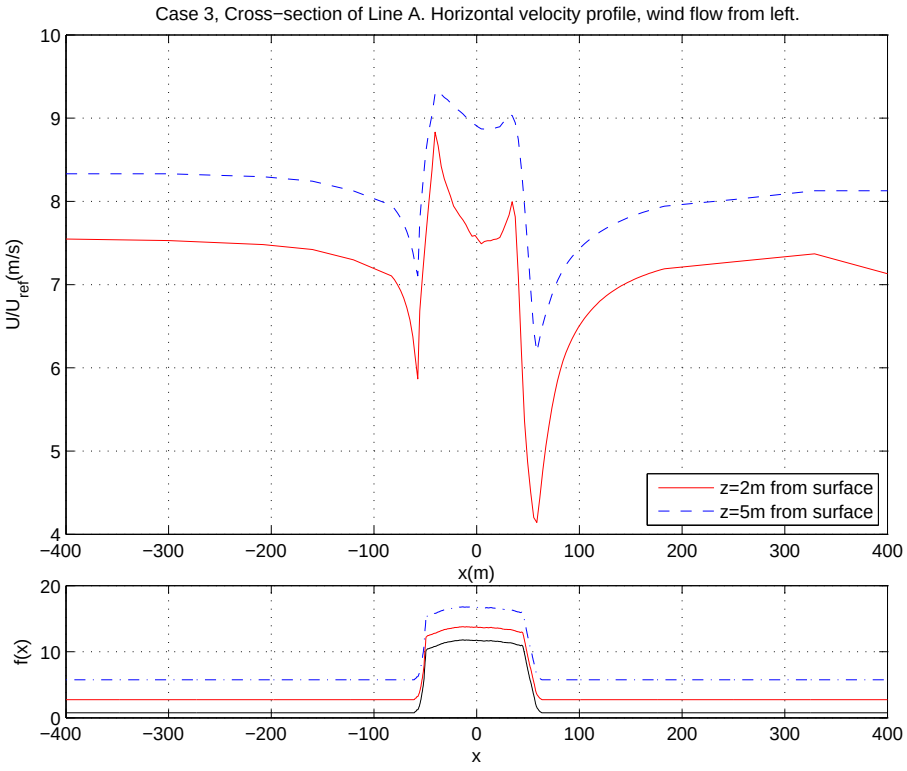

Figure 2.16: Case 3. Surface velocity on Line A.

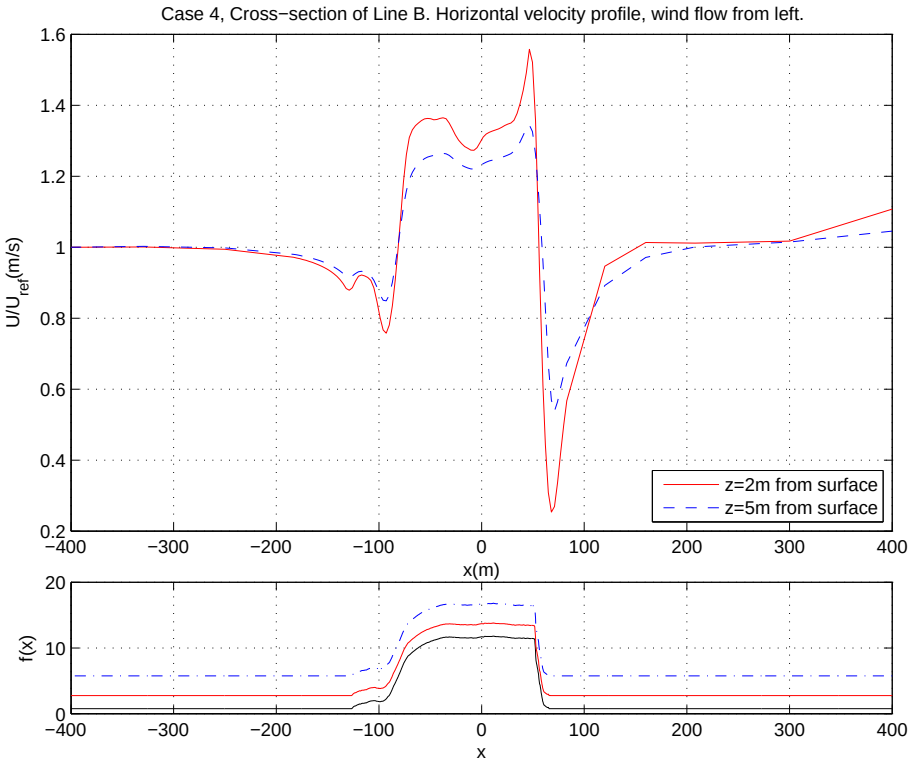

Figure 2.17: Case 4. Surface velocity on Line B.

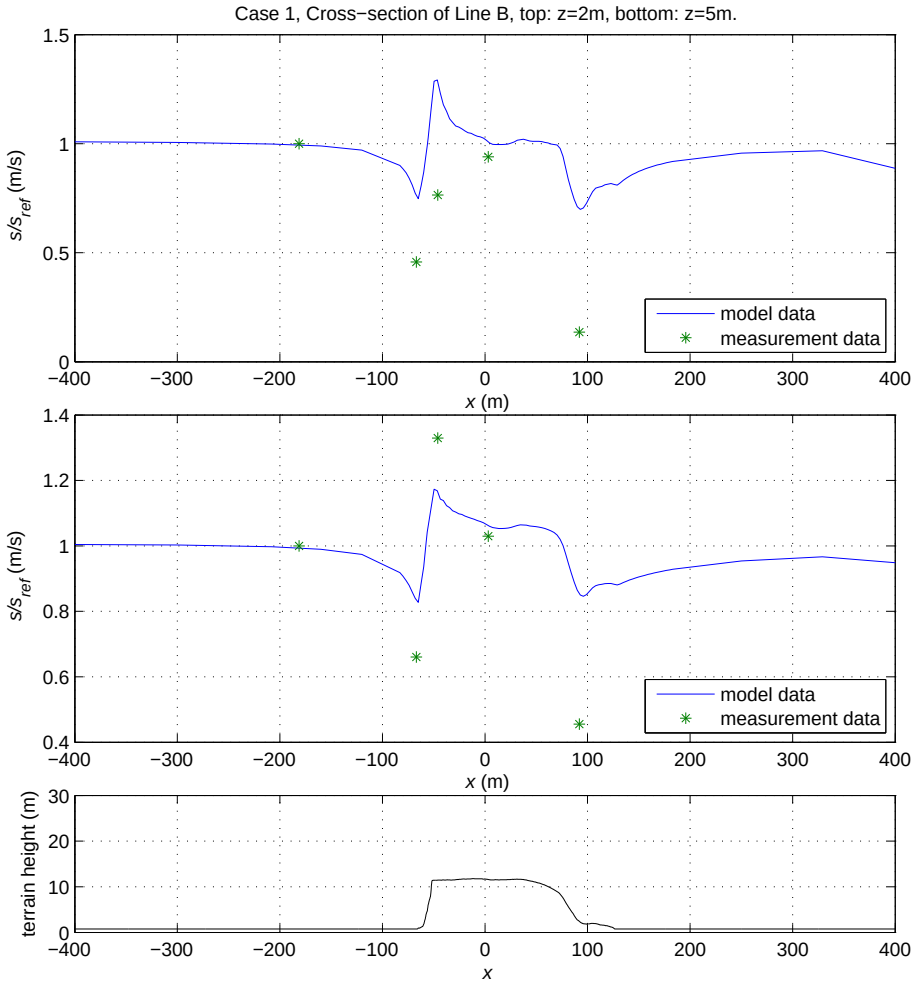

Figure 2.18: Case 1. Surface velocity on Line B compare with field measurements.

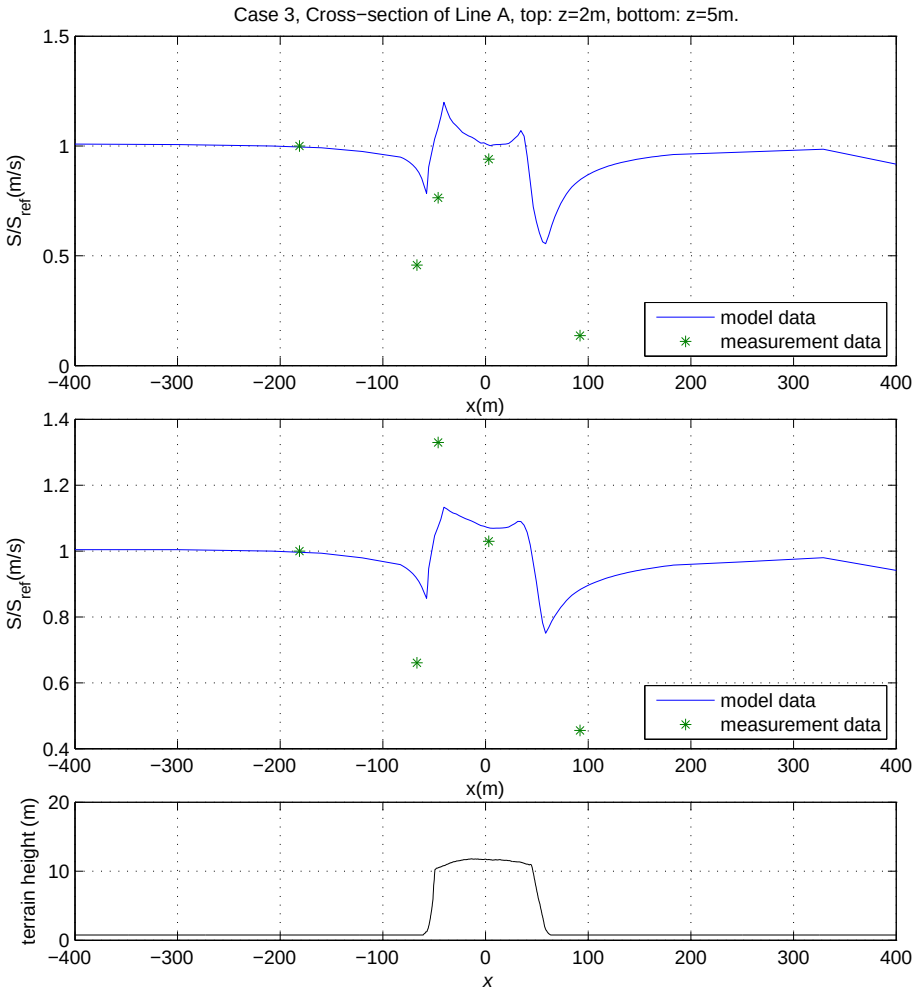

Figure 2.19: Case 3. Surface velocity on Line A compare with field measurements.

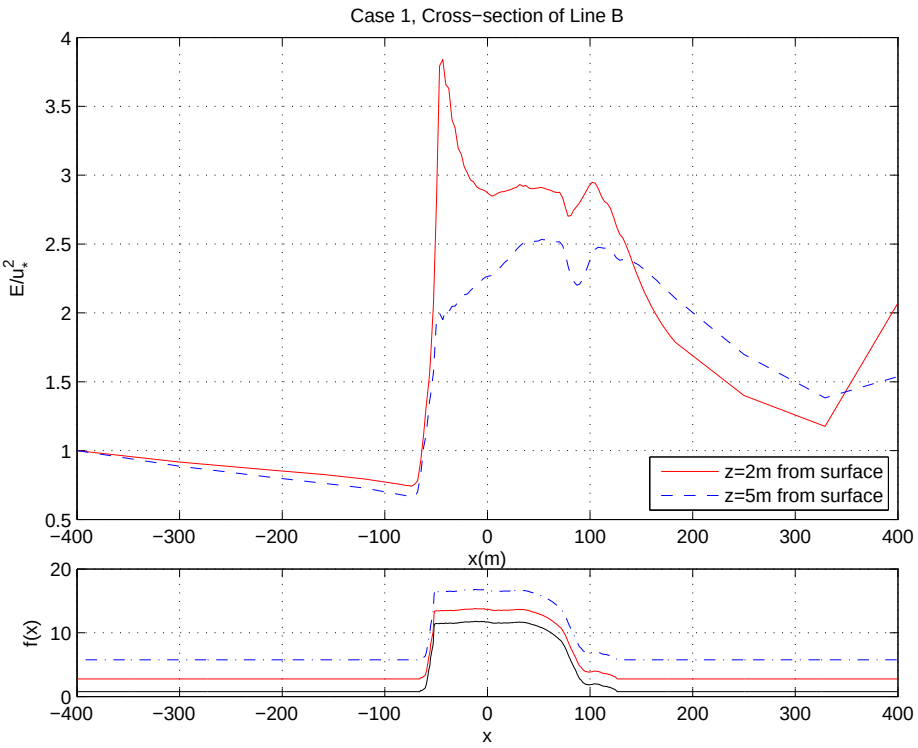

Figure 2.20: Case 1. Surface TKE on Line B.

the surface, the model under-predicts the magnitude of the normalized velocity perturbation near the upwind escarpment but agrees on the hill top where topographic and roughness change induced perturbations approximately balance each other. The two-dimensional NLMSFD model can predict the general flow pattern of Bolund hill. The normalized surface TKE is also given in Figures 2.20, 2.21, and 2.22.

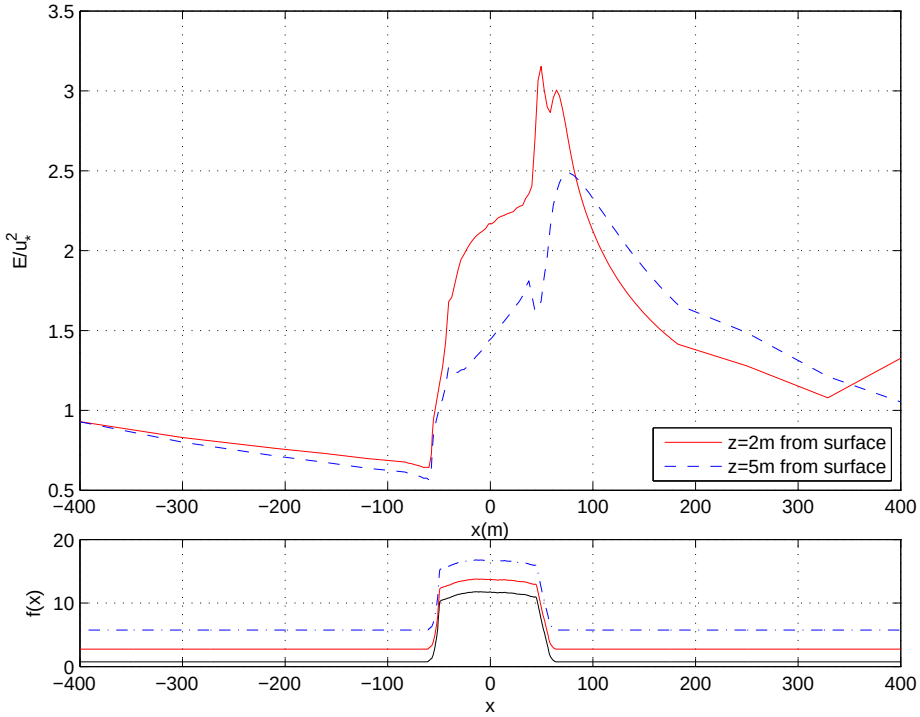

Figure 2.21: Case 3. Surface TKE on Line A.

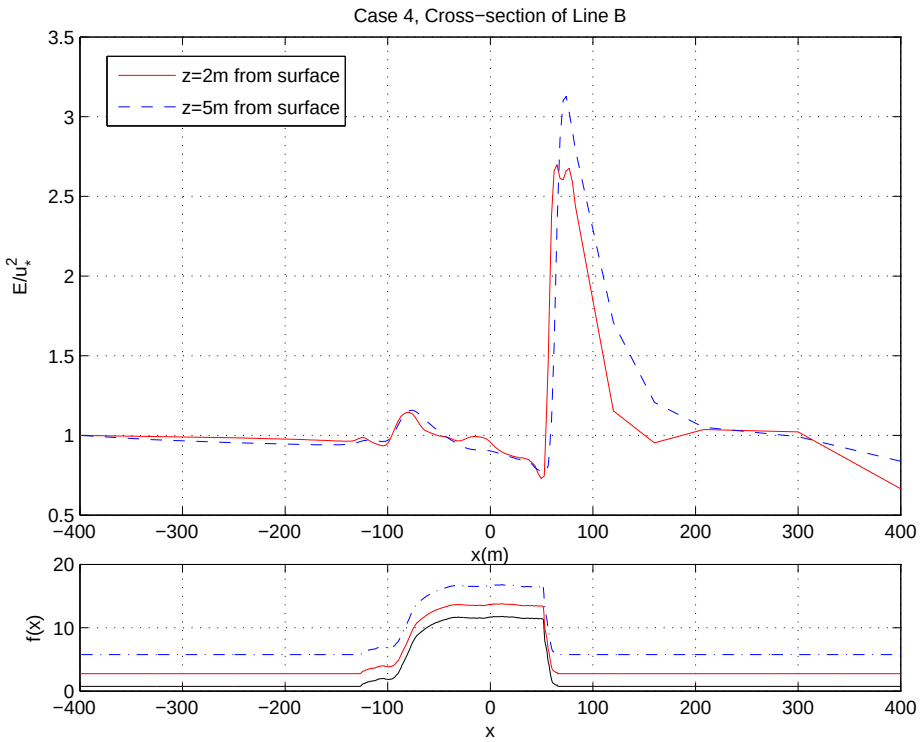

Figure 2.22: Case 4. Surface TKE on Line B.

3 The Characteristic Finite Volume Method for Time-dependent RANS Models with $k-\varepsilon$ closure

In the wind energy industry, solving the Navier-Stokes equations of turbulence flow is very challenging. Wind flow over complex topography has been widely studied since the 1970s in papers such as [41] [75], [12], [49], [20]. In problems with very high Reynolds numbers, the convective term is more dominated than the diffusive term. Mentioned in [72], this causes computational difficulties and nonphysical oscillations.

In order to resolve the dominance of nonlinear convective term, we study and develop the characteristic finite volume method to efficiently and accurately solve the time-dependent Reynolds Averaged Navier-Stokes (RANS) equations in this paper. The characteristic method uses a substantial derivative for temporal and convection discretization. Along characteristics, the solution changes much slower than in the original time direction at fixed points in space. Hence, the characteristic

difference will leads to efficient numerical schemes. It can get more accurate results by using larger time steps which is not restricted by the Courant-Friedrichs-Lewy condition. This kind of characteristic method has been studied by [62], [23], [72], [83], [48]. They showed that this kind characteristic method can be applied in many subject areas which relate to convection-diffusion problems. In meteorological models, people use the same kind of approach, called Semi-Lagrangian methods. [68] first used this method combined with the spectral form of the meteorological equations. Other applications, such as applying Semi-Lagrangian methods to shallow water equations, can be found in [69] and [13].

In this chapter, we develop a characteristic finite volume (CFV) method for the RANS models with a certain turbulence closure. Closure models are needed to study turbulence flows with high Reynolds numbers and better predict turbulent flow. There are many different closure models as noted in [4], such as $k-\kappa z$, $k-\varepsilon$, $k-\varepsilon-\tau$, $q^2\ell$. In this paper, the well-known $k-\varepsilon$ closure is used, where k stands for turbulence kinetic energy (TKE), κ is the von Karman constant (0.4), and ε is the dissipation rate of TKE. The use of $k-\varepsilon$ closure along with RANS models can be found in [47] and [22]. In our CFV method, we treat the time derivative and convective terms as a total derivative and discretize it along the characteristic direction by using a backward characteristic tracking. Combining this, the rest of

the terms from momentum equations in RANS models is discretized by the finite volume method. In the coupled $k-\varepsilon$ closure, it contains two equations with respect to k and ε, which have time derivative terms and convective terms. A similar characteristic approach is applied on these two equations of the $k-\varepsilon$ closure. As a result, we apply the characteristic finite volume method not only to the Reynolds averaged momentum equations but also to the coupled energy equations of the $k-\varepsilon$ closure. Numerical experiments will focus on two-dimensional topography. The first test is flow over flat terrain, we compare results from the characteristic finite volume scheme and a regular Euler time scheme. It shows the advantages of stability and accuracy from the characteristic method in large time steps. Complex terrains are tested next, which show that our method can be applied on various terrain shapes and roughness. Finally, a realistic terrain wind flow, over Bolund hill in Denmark, is efficiently simulated by the developed CFV method. Numerical results are in a good agreement with field measurements.

This chapter contains the model description of the RANS equations and closure models. We then propose the CFV method with a brief algorithm procedure to RANS equations with $k-\varepsilon$ closure. Example of flow over two-dimensional flat terrain is given for comparison of the convergence. We also test on two-dimensional cliff and blocks and further extend to a realistic terrain, the Bolund hill in Den-

mark. Simulation results are compared with field measurements by [11], [8], as well as numerical results from the previous chapter.

3.1 Navier-Stokes Equations

To describe the fluid motion, the Newton's law of motion is applied on the continuum. The Navier-Stokes equations are derived based on the conservation of mass and momentum ([37], [79], [19]). The governing equations of the incompressible Newtonian fluids are given in the following coordinate free form,

$$\rho\left(\frac{\partial}{\partial t}\mathbf{u}+\mathbf{u}\cdot\nabla\mathbf{u}\right) = -\nabla p+\mu\nabla^2\mathbf{u}+\mathbf{f}, \tag{3.1}$$

$$\nabla\cdot\mathbf{u} = 0, \tag{3.2}$$

where $\mathbf{u}=(u,v,w)$ is the velocity vector, ρ is the flow density, p is the pressure, μ is the dynamic viscosity and $\mathbf{f}$ represents body forces such as gravity and Coriolis force. The extended form can be written as,

$$\begin{aligned}
\rho\left(\frac{\partial u}{\partial t}+u\frac{\partial u}{\partial x}+v\frac{\partial u}{\partial y}+w\frac{\partial u}{\partial z}\right) &= -\frac{\partial p}{\partial x}+\mu\left(\frac{\partial^2 u}{\partial x^2}+\frac{\partial^2 u}{\partial y^2}+\frac{\partial^2 u}{\partial z^2}\right)+f_x,\\
\rho\left(\frac{\partial v}{\partial t}+u\frac{\partial v}{\partial x}+v\frac{\partial v}{\partial y}+w\frac{\partial v}{\partial z}\right) &= -\frac{\partial p}{\partial y}+\mu\left(\frac{\partial^2 v}{\partial x^2}+\frac{\partial^2 v}{\partial y^2}+\frac{\partial^2 v}{\partial z^2}\right)+f_y,\\
\rho\left(\frac{\partial w}{\partial t}+u\frac{\partial w}{\partial x}+v\frac{\partial w}{\partial y}+w\frac{\partial w}{\partial z}\right) &= -\frac{\partial p}{\partial z}+\mu\left(\frac{\partial^2 w}{\partial x^2}+\frac{\partial^2 w}{\partial y^2}+\frac{\partial^2 w}{\partial z^2}\right)+f_z,\\
\frac{\partial u}{\partial x}+\frac{\partial v}{\partial y}+\frac{\partial w}{\partial z} &= 0.
\end{aligned}$$

We can further obtain the dimensionless form by applying

$$\begin{aligned} x_i' &= \frac{x_i}{\widetilde{L}}, \\ u_i' &= \frac{u_i}{\widetilde{U}_{ref}}, \\ p' &= \frac{p}{\rho \widetilde{U}_{ref}^2}, \\ t_i' &= \frac{t\widetilde{U}_{ref}}{\widetilde{L}}, \end{aligned}$$

where $\widetilde{U_{ref}}$ and $\widetilde{L}$ are the characteristic velocity and length. Dividing $\rho\widetilde{U_{ref}}^2/\widetilde{L}$ on both sides of (3.1) and (3.2), we neglect primes from variables for simplicity,

$$\frac{\partial}{\partial t}\mathbf{u} + \mathbf{u}\cdot\nabla\mathbf{u} = -\nabla p + \frac{1}{\mathrm{Re}}\nabla^2\mathbf{u}, \tag{3.3}$$

$$\nabla\cdot\mathbf{u} = 0, \tag{3.4}$$

where Re is the Reynolds number

$$\mathrm{Re} = \frac{\rho\widetilde{U}_{ref}\widetilde{L}}{\mu}. \tag{3.5}$$

The equations under Cartesian coordinates by neglecting the body forces can be written as,

$$\frac{\partial u_i}{\partial t} + u_j\frac{\partial u_i}{\partial x_j} = -\frac{\partial p}{\partial x_i} + \frac{1}{\mathrm{Re}}\frac{\partial}{\partial x_j}\left(\frac{\partial u_i}{\partial x_j} + \frac{\partial u_j}{\partial x_i}\right), \tag{3.6}$$

$$\frac{\partial u_i}{\partial x_i} = 0. \tag{3.7}$$

3.2 Reynolds Averaged Navier-Stokes Equations

For turbulence flow with very high Reynolds number, Navier-Stokes equations cannot resolve the small-scale turbulence unless the computational mesh is fine enough to catch the dissipative eddies. Since the large eddies of the flow are dependent on the flow geometry and the smaller eddies are self similar, we can solve the mean variables under averaged Navier-Stokes equations and model the smaller eddies with turbulence closures or subgrid-scales. Three different averages are given as,

$$
\begin{aligned}
{}^{t}\overline{U}(x_0) &= \lim_{T\to\infty}\frac{1}{2T}\int_{-T}^{T} U(x_0,t)dt, && (3.8)\\
{}^{s}\overline{U}(t_0) &= \lim_{X\to\infty}\frac{1}{2X}\int_{-X}^{X} U(x,t_0)dx, && (3.9)\\
{}^{e}\overline{U}(x_0,t_0) &= \frac{1}{N}\sum_{n=1}^{N} U_n(x_0,t_0) = \int_{-\infty}^{\infty} U\cdot P(U)dU, && (3.10)
\end{aligned}
$$

where ${}^{t}\overline{U}$ is the time average, ${}^{s}\overline{U}$ is the space average, and ${}^{e}\overline{U}$ is the ensemble average. We can write each variable as a mean flow over a certain time frame plus a random fluctuating component. For example, the velocity can be written as,

$$\mathbf{u}(x,t) = \mathbf{U}(x,t) + \mathbf{u}'(x,t), \tag{3.11}$$

where $\mathbf{U} = (U_1, U_2, U_3)$. We substitute both terms into the Navier-Stokes equations (3.6) and (3.7) to obtain the following Reynolds Averaged Navier-Stokes equations,

$$
\begin{aligned}
\frac{\partial}{\partial t}U_i + U_j\frac{\partial}{\partial x_j}U_i &= -\frac{\partial P}{\partial x_i} + \frac{1}{\mathrm{Re}}\frac{\partial}{\partial x_j}\left(\bar{\tau}_{ij} + \tau_{ij}^{R}\right), && (3.12)\\
\frac{\partial U_i}{\partial x_i} &= 0, && (3.13)
\end{aligned}
$$

where $\bar{\tau}_{ij}$ and τ_{ij}^R are defined as

$$\bar{\tau}_{ij} \equiv \nu \left(\frac{\partial U_i}{\partial x_j} + \frac{\partial U_j}{\partial x_i} \right), \tag{3.14}$$

$$\tau_{ij}^R \equiv -\rho \overline{u_i' u_j'}. \tag{3.15}$$

The τ_{ij}^R is considered as the extra stress term, which is known as the Reynolds stress. Such terms need to be modelled by the closure equations in order to have the same number of unknowns and equations. According to the Boussinesq approximation, the model equations for Reynolds stress and eddy viscosity are given as,

$$-\overline{u_i' u_j'} = -\frac{2}{3} k \delta_{ij} + \nu_t \left(\frac{\partial U_i}{\partial x_j} + \frac{\partial U_j}{\partial x_i} \right), \tag{3.16}$$

$$\nu_t = c_\mu \frac{k^2}{\varepsilon}, \tag{3.17}$$

where k is the Turbulence Kinetic Energy (TKE).

3.3 RANS Models with $k - \varepsilon$ Closure

The turbulence flow can be resolved by RANS equations along with various closure schemes. In this Chapter, we adopt the $k - \varepsilon$ closure because it is the most widely

used closure scheme. The dimensional form of the RANS equations are given as,

$$\rho\frac{\partial}{\partial t}U_i + \rho U_j\frac{\partial}{\partial x_j}U_i = -\frac{\partial P}{\partial x_i} + \frac{\partial}{\partial x_j}\left(\mu\left(\frac{\partial U_i}{\partial x_j}+\frac{\partial U_j}{\partial x_i}\right) - \rho\overline{u_i'u_j'}\right), \quad (3.18)$$

$$\frac{\partial U_i}{\partial x_i} = 0, \quad (3.19)$$

$$-\rho\overline{u_i'u_j'} = -\frac{2}{3}\rho k\delta_{ij} + \mu_t\left(\frac{\partial U_i}{\partial x_j}+\frac{\partial U_j}{\partial x_i}\right), \quad (3.20)$$

$$\mu_t = \rho c_\mu\frac{k^2}{\varepsilon}. \quad (3.21)$$

To predict the turbulent flow numerically, [47] calculated the turbulent kinetic energy k $(= \frac{1}{2}\overline{u_j'u_j'})$ and its dissipation rate ε from two equations. [22] states that the $k-\varepsilon$ model is used widely in engineering because it gives reasonable estimate of the mean flow, it is better than the simple mixing-length model but not that complicated. The equations of k and ε are

$$\rho\frac{\partial}{\partial t}k + \rho U_j\frac{\partial}{\partial x_j}k = \frac{\partial}{\partial x_j}\left[\left(\mu+\frac{\mu_t}{\sigma_k}\right)\frac{\partial k}{\partial x_j}\right] + \mu_t\frac{\partial U_i}{\partial x_j}\left(\frac{\partial U_i}{\partial x_j}+\frac{\partial U_j}{\partial x_i}\right) - \rho\varepsilon, \quad (3.22)$$

$$\rho\frac{\partial}{\partial t}\varepsilon + \rho U_j\frac{\partial}{\partial x_j}\varepsilon = \frac{\partial}{\partial x_j}\left[\left(\mu+\frac{\mu_t}{\sigma_\varepsilon}\right)\frac{\partial \varepsilon}{\partial x_j}\right] + c_1\mu_t\frac{\varepsilon}{k}\frac{\partial U_i}{\partial x_j}\left(\frac{\partial U_i}{\partial x_j}+\frac{\partial U_j}{\partial x_i}\right) - \rho c_2\frac{\varepsilon^2}{k}, \quad (3.23)$$

where both k and ε are ensemble averaged. Coefficients given in Table 3.1 are set to the same values as [22],

Equations (3.18)-(3.23) form a complete system. Boundary conditions are re-

Table 3.1: The $k-\varepsilon$ model constants

κ	c_μ	σ_k	σ_ε	c_1	c_2
0.4	0.09	1.0	1.11	1.44	1.92

quired for the mean variables such as $\mathbf{U}$, p, k, ε. The inlet boundary conditions for $\mathbf{U}$, k, ε are given as

$$U_1 = \frac{u_*}{\kappa}\ln\left(\frac{z+z_0}{z_0}\right),\ U_2 = 0,\ U_3 = 0, \tag{3.24}$$

$$k = \frac{u_*^2}{c_\nu^{1/2}}, \tag{3.25}$$

$$\varepsilon = \frac{u_*^3}{\kappa(z+z_0)}. \tag{3.26}$$

The zero-gradient condition is used for p. And a calculated condition is used for ν_t,

$$\nu_t = C_\mu \frac{k^2}{\varepsilon}. \tag{3.27}$$

where $\nu_t = \mu_t/\rho$. The top boundary conditions are slip condition for $\mathbf{U}$, k, ε and zero-gradient for p. The outlet boundary is considered as the flow is fully developed. Thus the zero-gradient condition is used for $\mathbf{U}$, k, and ε. The pressure is given a fixed value of zero. For the wall boundary, no-slip condtion is set for $\mathbf{U}$ and zero-gradient condition is set for p. Wall functions are used for k, ε, ν_t ([34]).

3.4 The Characteristic Finite Volume Method

For the convection term dominated problems, the characteristic direction can be used in the equation descritization instead of the original time direction. This will be applied to the momentum equations (3.18), k equation (3.22), and ε equation (3.23). We first consider the compact form of the momentum equation (3.18) for convinence,

$$\rho\frac{\partial \mathbf{U}}{\partial t} + \rho\mathbf{U}\cdot\nabla\mathbf{U} = \nabla\cdot(\Gamma_{\mathbf{U}}\nabla\mathbf{U}) + S_{\mathbf{U}}(\mathbf{U},k,\varepsilon) - \nabla p, \tag{3.28}$$

where $\Gamma_{\mathbf{U}}$ is a function of k and ε and $S_{\mathbf{U}}$ is the source term. The material derivative of U can be written as

$$\frac{D\mathbf{U}}{D\tau} = \frac{\partial \mathbf{U}}{\partial t} + \mathbf{U}\cdot\nabla\mathbf{U}. \tag{3.29}$$

For a given temporal grid $t_n = n\Delta t$, the characteristic $\chi(\tau;\mathbf{x},t_{n+1})$ for every $\mathbf{x}$ and $\tau \in (t_n, t_{n+1})$ is given by,

$$\frac{d\chi(\tau;\mathbf{x},t_{n+1})}{d\tau} = \mathbf{U}(\chi(\tau;\mathbf{x},t_{n+1}),\tau), \tag{3.30}$$

$$\chi(t_{n+1};\mathbf{x},t_{n+1}) = \mathbf{x}. \tag{3.31}$$

Therefore, the material derivative can be approximated as following,

$$\frac{D\mathbf{U}}{D\tau} \cong \frac{\mathbf{U}^{n+1}(\mathbf{x}) - \mathbf{U}^{n}(\chi^n)}{\Delta\tau}, \tag{3.32}$$

where $\chi^n = \chi(t_n;\mathbf{x},t_{n+1})$.

In order to approximate the material derivative, we use the known value of $\mathbf{U}^n$ as an approximation of $\mathbf{U}$ in Equation (3.30). The equation becomes that for $\tau \in (t_n, t_{n+1})$.

$$\frac{d\chi(\tau, \mathbf{x})}{d\tau} = \mathbf{U}^n(\chi(\tau)), \tag{3.33}$$

$$\chi(t_{n+1}) = \mathbf{x}. \tag{3.34}$$

The above characteristic equation can be solved for χ^n,

$$\chi^n = \mathbf{x} - \Delta t \mathbf{U}^n(\mathbf{x}). \tag{3.35}$$

In the numerical simulation, the characteristic method is combined with finite volume method (FVM). The finite volume discretisations are used as mentioned in [57], [80], [43] and in the open source CFD software OpenFOAM [55].

Given the two-dimensional domain of control volume, the centroid of the control volume P denotes the computational point for the material derivative. N denotes all other owner and neighbor cell centers. All cell faces are marked as f, thus the face area vector $\mathbf{S}_f$ is constructed for each face and points outwards from the cell centre, V is the volume of the cell. By using the Finite Volume technique, we integrate the equation (3.28) over the control volume. We can convert the volume integral to the surface integral by the Gauss's theorem. The Laplacian term can be

treated as

$$\begin{aligned}\int_V \nabla \cdot (\Gamma_{\mathbf{U}} \nabla \mathbf{U}) dV &= \int_{\mathbf{S}} d\mathbf{S} \cdot (\Gamma_{\mathbf{U}} \nabla \mathbf{U}) \\ &= \sum_f \Gamma_{\mathbf{U}f} \mathbf{S}_f \cdot (\nabla \mathbf{U})_f. \end{aligned} \tag{3.36}$$

To resolve the face normal gradient, let d be the distance between the center of the owner cell P and the neighbor cell N. We have

$$\mathbf{S}_f \cdot (\nabla \mathbf{U})_f \cong |\mathbf{S}_f| \frac{\mathbf{U}_N - \mathbf{U}_P}{|d|}. \tag{3.37}$$

In each control volume, we integrate the momentum equation (3.28). The left hand side of the equation yields,

$$\begin{aligned}\rho \int_V \left[\frac{\partial \mathbf{U}}{\partial t} + U \cdot \nabla \mathbf{U} \right] dV &= \rho \int_V \frac{D}{D\tau} \mathbf{U} dV \\ &= \frac{\rho \mathbf{U}_P(\mathbf{x}) V - \rho \mathbf{U}_P^O(\chi^n) V}{\Delta t}, \end{aligned} \tag{3.38}$$

where the superscribed notation O denotes values in the previous time step. Combining other terms from the right hand side of Equation (3.28) which are discretised by the finite volume method, the resulting semi-discretised system for momentum equations are,

$$a_P \mathbf{U}_P = H_{\mathbf{U}}(k^O, \varepsilon^O; \mathbf{U}) + a_P \mathbf{U}_P^O(\chi^n) + S_{\mathbf{U}}(\mathbf{U}^O, k^O, \varepsilon^O) - \int_V \nabla p dV, \tag{3.39}$$

where a_P is the coefficient,

$$a_P = \frac{\rho V}{\Delta t}, \tag{3.40}$$

and $H_{\mathbf{U}}(k^O, \varepsilon^O; \mathbf{U})$ is the algebraic system term which contains the discretization of the diffusive term,

$$H_{\mathbf{U}}(k^O, \varepsilon^O; \mathbf{U}) = -\sum_N a_N(k^O, \varepsilon^O)\mathbf{U}_N, \tag{3.41}$$

where a_N are coefficients. Similarly, the discretization form of k equation (3.22) and ε equation (3.23) can be written as,

$$a_P k_P = H_k(k^O, \varepsilon^O, \mathbf{U}^O; k) + a_P k_P^O(\chi^n) + S_k(\mathbf{U}^O, k^O, \varepsilon^O), \tag{3.42}$$

$$a_P \varepsilon_P = H_\varepsilon(k^O, \varepsilon^O, \mathbf{U}^O; \varepsilon) + a_P \varepsilon_P^O(\chi^n) + S_\varepsilon(\mathbf{U}^O, k^O, \varepsilon^O). \tag{3.43}$$

To solve the incompressible time-dependent RANS equations, the velocity-pressure coupling causes oscillations in solutions. [68] first used this method combined with the spectral form of the meteorological equations. [59] derived a scheme for steady-state Navier-Stokes equations by using momentum prediction and pressure and velocity corrections, this method is known as the Semi-Implicit Method for Pressure-Linked Equations (SIMPLE). For a time-dependent system, which also involves other scalar transport equations, [40] derived the pressure-implicit with splitting of operator (PISO) algorithm and [66] suggested to used a non-staggered mesh grid.

The pressure gradient term is not discretised yet in Equation (3.39), a pressure equation is derived by joint of the momentum equations and the discretised

continuity equation,

$$\int_V \nabla \cdot U dV = \oint_{\mathbf{S}} d\mathbf{S} \cdot \mathbf{U} = 0. \tag{3.44}$$

Substituting Equation (3.39) to the above equation, we obtain the following approximated pressure equation,

$$\sum_f \mathbf{S_f} \cdot \left[\left(\frac{1}{a_P} \right)_f (\nabla_h p)_f \right] = \sum_f \mathbf{S_f} \cdot \left(\frac{H_{\mathbf{U}}(k^O, \varepsilon^O; \mathbf{U})}{a_P} + \mathbf{U}_P^O(\chi^n) + \frac{S_{\mathbf{U}}(\mathbf{U}^O, k^O, \varepsilon^O)}{a_P} \right)_f, \tag{3.45}$$

where ∇_h is the difference gradient operator. Therefore, the solution procedure of the Characteristic Finite Volume method is combined with PISO algorithm, where the PISO loop contains an implicit velocity predictor and several explicit velocity correctors. More corrector steps can be performed, however, at least two corrector steps are needed.

The Algorithm of the CFV method:

Step 1. Set initial values for all variables, such as $\mathbf{U}^O$, p^O, k^O, ε^O.

Step 2. Start loop until final time step reached. Use PISO algorithm in following, do Step 3 to Step 5.

Step 3. Predictor step, solve the momentum equations Equation (3.39) for $\mathbf{U}^*$. The pressure field from old time step is used.

$$a_P \mathbf{U}_P^* = H_{\mathbf{U}}(k^O, \varepsilon^O; \mathbf{U}^*) + a_P \mathbf{U}_P^O(\chi^n) + S_{\mathbf{U}}(\mathbf{U}^O, k^O, \varepsilon^O) - \nabla_h p^O V.$$

Step 4. First corrector step, solve the pressure equation Equation (3.45) for p^*,

$$\sum_f \mathbf{S_f} \cdot \left[\left(\frac{1}{a_P} \right)_f (\nabla_h p^*)_f \right] = \sum_f \mathbf{S_f} \cdot \left(\frac{H_{\mathbf{U}}(k^O, \varepsilon^O; \mathbf{U}^*)}{a_P} + \mathbf{U}_P^O(\chi^n) + \frac{S_{\mathbf{U}}(\mathbf{U}^O, k^O, \varepsilon^O)}{a_P} \right)_f ,$$

and correct momentum equation explicitly,

$$a_P \mathbf{U}_P^{**} = H_{\mathbf{U}}(k^O, \varepsilon^O; \mathbf{U}^*) + a_P \mathbf{U}_P^O(\chi^n) - S_{\mathbf{U}}(\mathbf{U}^*, k^O, \varepsilon^O) - \nabla_h p^* V.$$

Step 5. Second corrector step, solve the pressure equation Equation (3.45) for p^{**},

$$\sum_f \mathbf{S_f} \cdot \left[\left(\frac{1}{a_P} \right)_f (\nabla_h p^{**})_f \right] = \sum_f \mathbf{S_f} \cdot \left(\frac{H_{\mathbf{U}}(k^O, \varepsilon^O; \mathbf{U}^{**})}{a_P} + \mathbf{U}_P^O(\chi^n) + \frac{S_{\mathbf{U}}(\mathbf{U}^O, k^O, \varepsilon^O)}{a_P} \right)_f ,$$

and correct momentum equation explicitly,

$$a_P \mathbf{U}_P^{***} = H_{\mathbf{U}}(k^O, \varepsilon^O; \mathbf{U}^{**}) + a_P \mathbf{U}_P^O(\chi^n) + S_{\mathbf{U}}(\mathbf{U}^{**}, k^O, \varepsilon^O) - \nabla_h p^{**} V.$$

Step 6. Use the known $\mathbf{U}^{n+1} = \mathbf{U}^{***}$ field and $p^{n+1} = p^{**}$ field, solve turbulence equations Equation (3.42), Equation (3.43) implicitly,

$$\begin{aligned} a_P k_P^{n+1} &= H_k(k^O, \varepsilon^O, \mathbf{U}^O; k^{n+1}) + a_P k_P^O(\chi^n) + S_k(\mathbf{U}^{n+1}, k^O, \varepsilon^O), \\ a_P \varepsilon_P^{n+1} &= H_\varepsilon(k^O, \varepsilon^O, \mathbf{U}^O; \varepsilon^{n+1}) + a_P \varepsilon_P^O(\chi^n) + S_k(\mathbf{U}^{n+1}, k^O, \varepsilon^O). \end{aligned}$$

Other turbulence equations Equation (3.20), Equation (3.21) are solved explicitly from the known k^{n+1} and ε^{n+1}.

Step 7. Stop when the time limit is reached.

Table 3.2: The solvers for linear system

Eqn.	Solver	Preconditioner	Tolerance
U	Preconditioned bi-conjugate gradient	Diagonal incomplete-LU (asymmetric)	1e-5
P	Preconditioned conjugate gradient	Diagonal incomplete--Cholesky (symmetric)	1e-6
P Final	Preconditioned conjugate gradient	Diagonal incomplete--Cholesky (symmetric)	1e-6
k	Preconditioned bi-conjugate gradient	Diagonal incomplete-LU (asymmetric)	1e-5
ε	Preconditioned bi-conjugate gradient	Diagonal incomplete-LU (asymmetric)	1e-5

The resulting linear systems in each predictor and corrector steps are solved by vary equation solvers in OpenFOAM, In Table 3.2, these solvers are used typically in the PISO algorithm. Table 3.3 contains the numerical scheme for each terms of the equation such as the gradient, divergence, and laplacian derivatives.

Table 3.3: The derivative and interpolation schemes

Derivatives	Schemes
Time	Euler
Gradient	Gauss Linear
Divergence	Gauss Limited Linear
Laplacian	Gauss Linear corrected
Interpolation	Linear

3.5 Numerical experiments on two-dimensional flat terrain

In order to show the advantages of the Characteristic Finite Volume method, we consider a two-dimensional turbulence channel air flow over a flat terrain at small scale. In a time-dependent problem, the step size of the time iteration is an important criterion for temporal accuracy and numerical stability. In this section, numerical results are compared between the characteristic finite volume method and the implicit Euler method. The comparisons will show that the characteristic finite volume method converges with a relatively large time step size while the Euler method is broken, meanwhile the accuracy of the solution from the characteristic finite volume method is still maintained.

We perform the simulation within a rectangular domain of 10 m long in

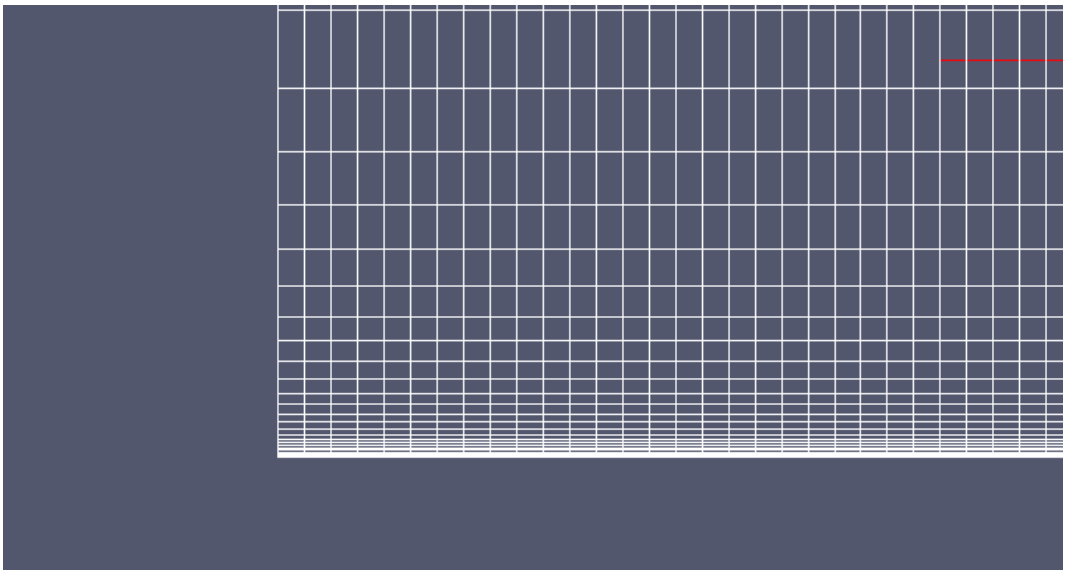

Figure 3.1: Case description of channel flow over flat terrain.

x-direction and 3 m high in z-direction. In Figure 3.1, a logarithmic grid is used in vertical direction and an uniform grid is used in horizontal direction. RANS equations with $k-\varepsilon$ model are used in examples. The Reynolds number used here is Re= 10^5. $L/z_0 = 10^3$, where L is the length of the computation domain and z_0 (=0.01 m) is the surface roughness. The inlet velocity follows the log-wind profile with a reference height of H_{ref}=3 m and a reference velocity of U_{ref}=1 m/s. The inlet boundary condition for pressure is zero gradient, and the initial values of k and ε are assigned as

$$k = \frac{u_*^2}{c_\mu^{1/2}}, \tag{3.46}$$

$$\varepsilon = \frac{c_\mu^{0.75} k^{1.5}}{\ell}, \tag{3.47}$$

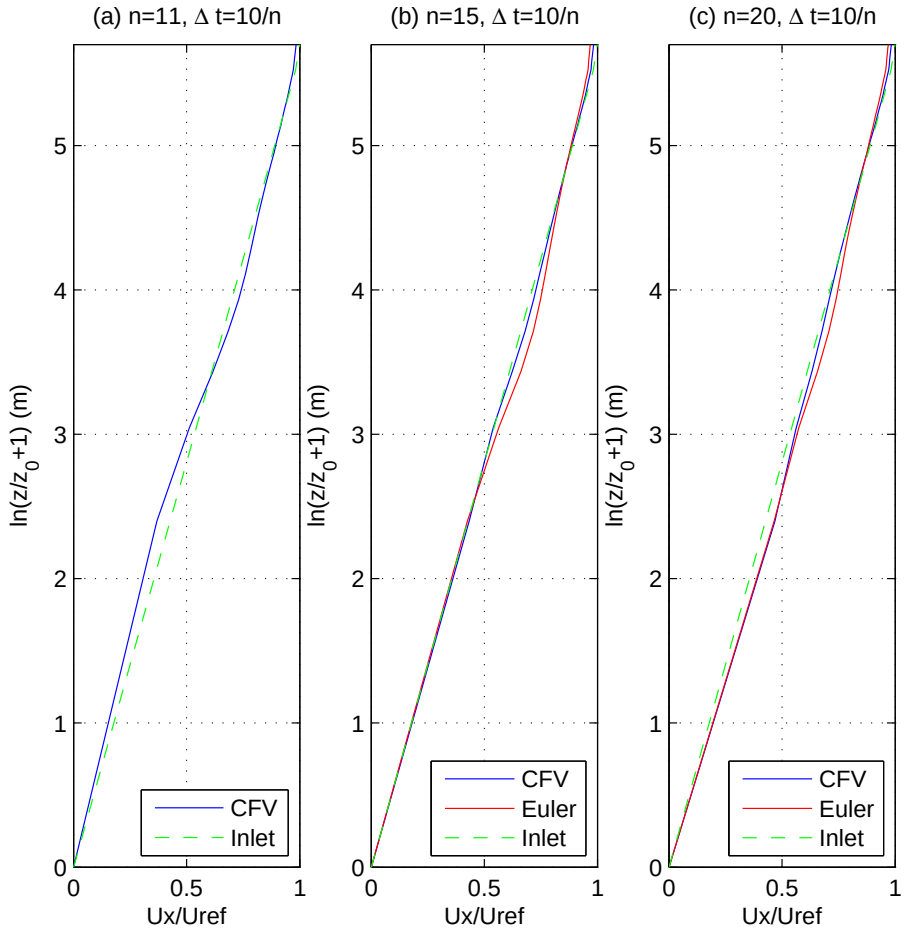

Figure 3.2: 2D flat terrain. Normalized vertical profiles of Ux, locate at $x = 5$ m and $T = 10$ s. (a) $\Delta t = 10/n = 1$ s, (b) $\Delta t = 10/n = 0.6667$ s, (c) $\Delta t = 10/n = 0.5$ s.

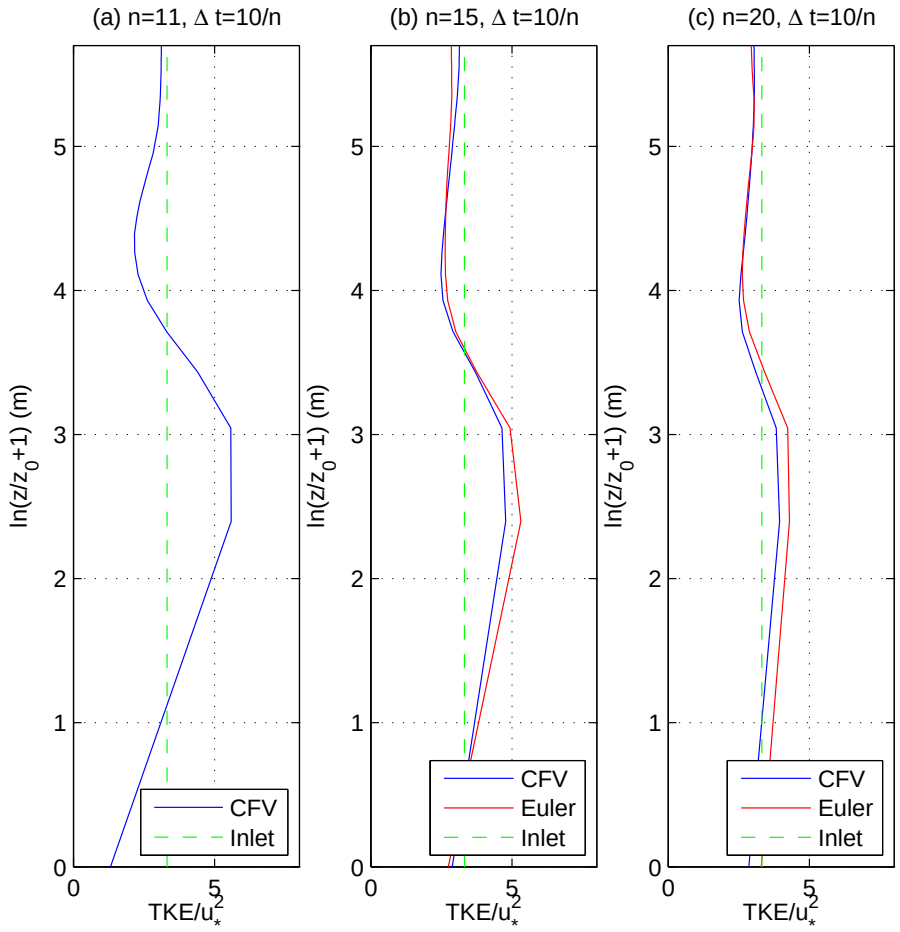

Figure 3.3: 2D flat terrain. Normalized vertical profiles of TKE, locate at $x = 5$ m and $T = 10$ s. (a) $\Delta t = 10/n = 1$ s, (b) $\Delta t = 10/n = 0.6667$ s, (c) $\Delta t = 10/n = 0.5$ s.

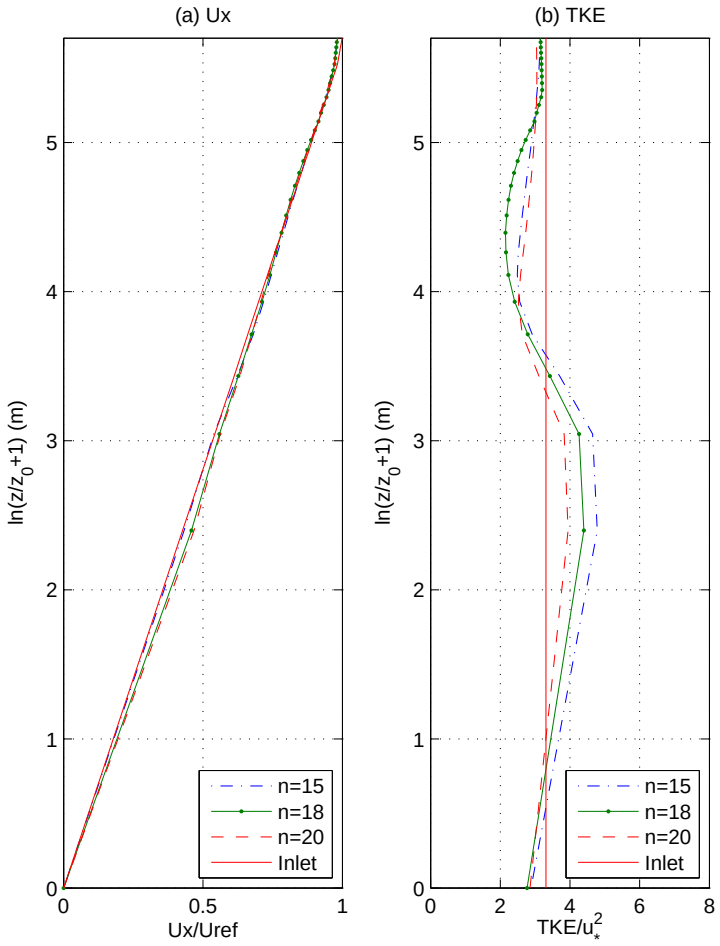

Figure 3.4: 2D flat terrain. Normalized vertical profiles from CFV method, locate at $x = 5$ m and $T = 10$ s. (a) Ux, (b) TKE.

where c_μ is constant of $k-\varepsilon$ model and ℓ is length scale. The outlet boundary conditions are zero for pressure and zero gradient for other variables. A no-slip condition is applied on the lower boundary and free stream values are assigned to variables on the upper boundary.

Numerical results in Figure 3.2 show the vertical profile of normalized x-direction velocity U_x/U_{ref} at the centre of the domain. We simulate the air flow for $T = 10$ s and let n denote the number of time intervals during the calculation of T s, therefore Δt is defined as T/n. When Δt is relatively small ($\Delta t = T/15$), both the Characteristic Finite Volume (CFV) method and the Euler method converge as shown in Figure 3.2(c). The velocity profiles are well maintained compare with the inlet profile. But when increase the size of Δt ($\Delta t = T/11$), the result from the Euler method is inaccurate in Figure 3.2(b), and totally broken in Figure 3.2(a) under $\Delta t = T/10$. In Figure 3.3, vertical profile of normalized TKE gives a similar conclusion in comparing stability between CFV method and Euler method.

From above, we obtain an obvious stability improvement by using the characteristic method over the implicit Euler method. In Figure 3.4, it shows a fast convergence of U_x and TKE by comparing the characteristic method itself. In order to track the trajectories of the $\chi(t_n)$ in the CFV method, we plot them in Figure

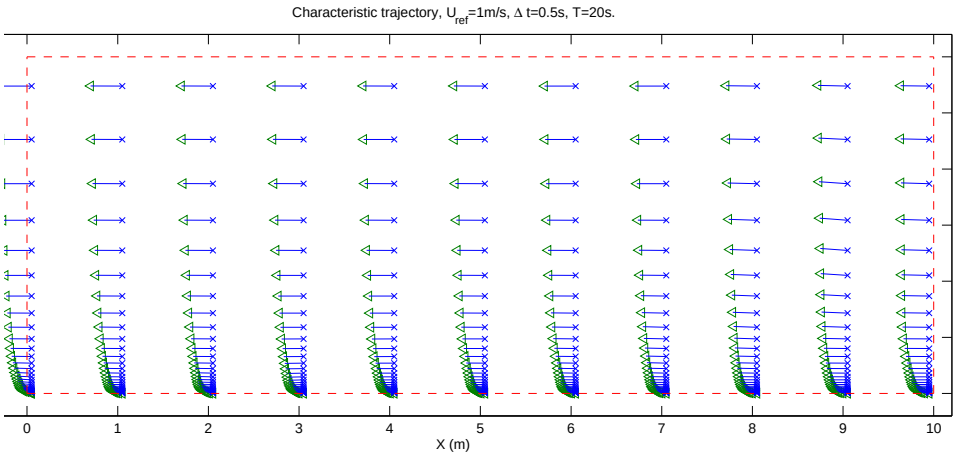

Figure 3.5: 2D flat terrain. Characteristic trajectories $\Delta t = 0.5$ s, $T = 20$ s.

3.5, which shows that the direction of each trajectory is consistent with the velocity profile.

In Figure 3.6, we also test the velocity profile versus different surface roughness. The inlet velocity is fixed under $L/z_0 = 10^3$, but the roughness of the flat terrain is used as $L/z_0 = 10^1$, $L/z_0 = 5 \times 10^2$, $L/z_0 = 10^3$, and $L/z_0 = 10^4$. For a larger roughness, we can observe the speed deficit near wall and for a small roughness, there is a speed up near wall.

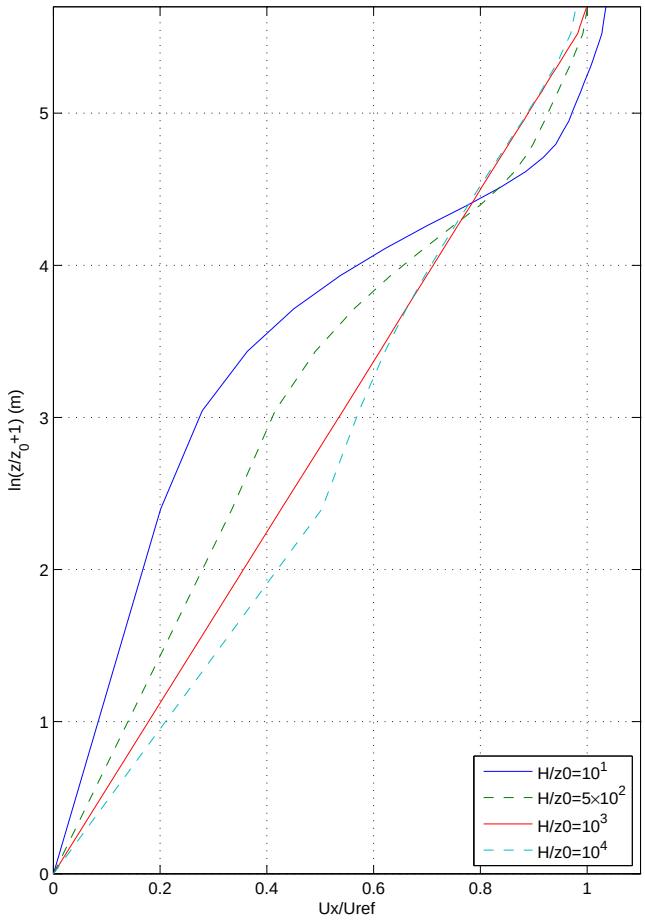

Figure 3.6: 2D flat terrain. Normalized vertical profiles of Ux, locate at $x = 5$ m and $T = 10$ s.

3.6 Two-dimensional geometric topography simulations

In this section we apply the CFV method on two-dimensional geometric topography and simulate air flow over complex terrain with steep curvature. Given in Figure 3.7, the first case is a two-dimensional cliff with the height $H = 1$ m and cliff length $20H$. The computation domain is $34H$ in length and $24H$ in height, the cliff is placed at $7H$ meters from the inlet (west). Two different surface roughness are tested, the smooth surface has $u_* = 0.21$ m/s and $z_0 = 0.01$ m, the rough surface has $u_* = 0.52$ m/s and $z_0 = 0.3$ m. RANS equations with $k - \varepsilon$ model are used in the computations, and the boundary conditions are used same as those mentioned earlier.

In Figure 3.8, we first present a simple comparison. The numerical results from the characteristic finite volume method are compared with the one from the implicit Euler method. We simulate the air flow over a smooth surface with $z_0 = 0.01$ m after $T = 10$ s, under an uniform grid with $\Delta x = \Delta y = H/5 = 0.2$ m. For the vertical profile of x-direction velocity U_x on the upwind side of the cliff, we can see both methods work well in Figure 3.8(c) when $n = 25$, but the Euler method starts oscillating in Figure 3.8(b) and is broken down in Figure 3.8(a) when $n = 21$. In Figure 3.9, same comparison is presented on the downside of the cliff. Both meth-

Figure 3.7: Case description of flow over 2D cliff.

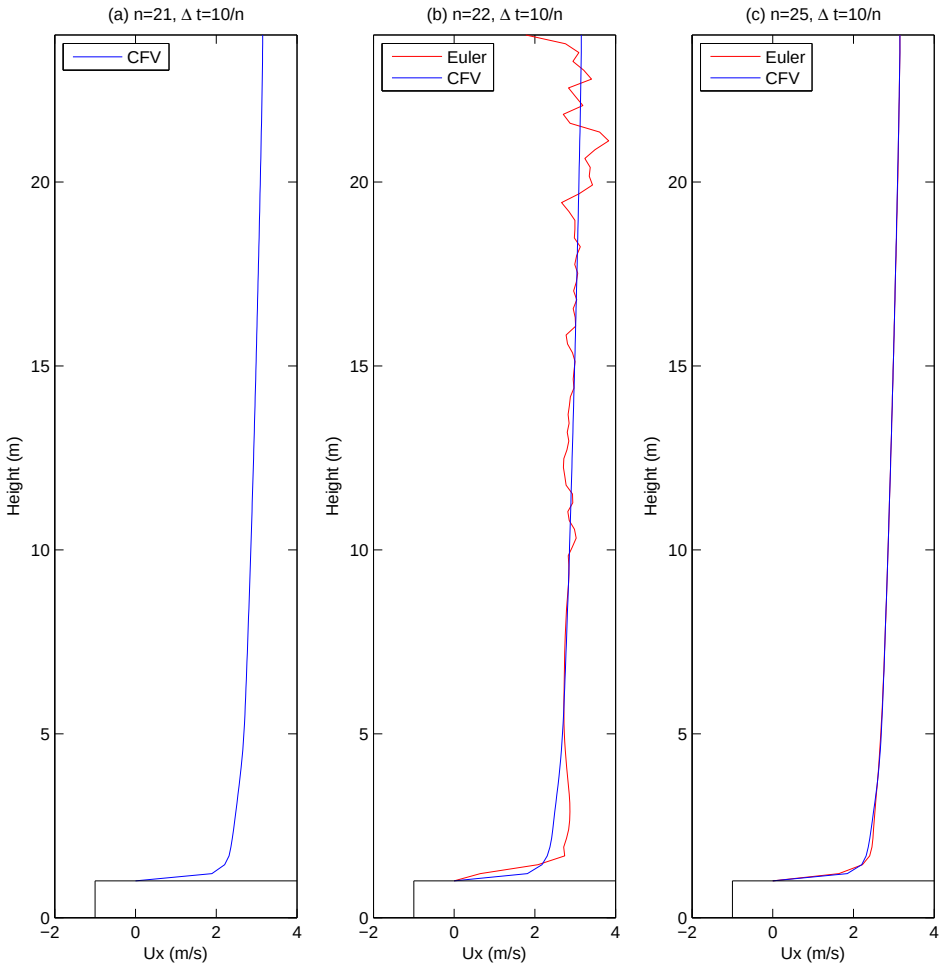

Figure 3.8: 2D cliff, cliff height=H, $z_0 = 0.01$ m, $u_* = 0.21$ m/s. $\Delta x = H/5 = 0.2$ m. Vertical profile of Ux, locate at $x = 7.5$ m and $T = 10$ s. (a) $\Delta t = T/n = 0.4762$ s, (b) $\Delta t = T/n = 0.4545$ s, (c) $\Delta t = T/n = 0.4$ s.

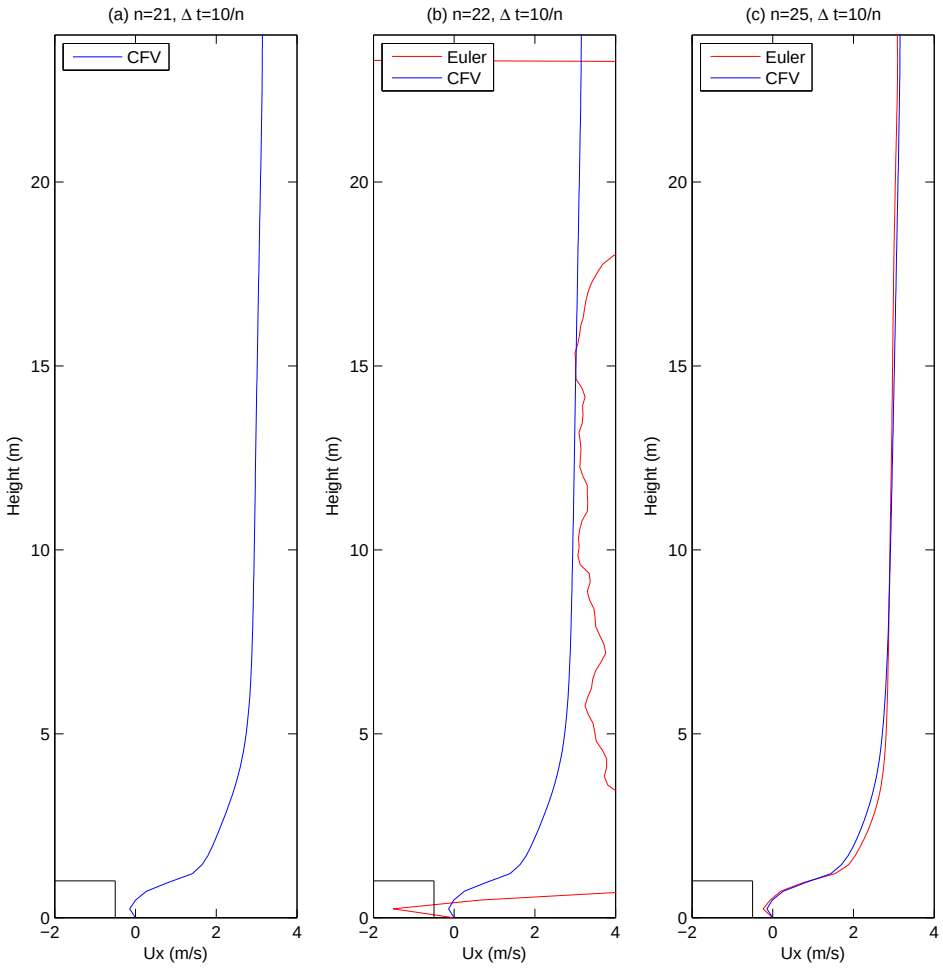

Figure 3.9: 2D cliff, cliff height=H, $z_0 = 0.01$ m, $u_* = 0.21$ m/s. $\Delta x = H/5 = 0.2$ m. Vertical profile of Ux, locate at $x = 27.5$ m and $T = 10$ s. (a) $\Delta t = T/n = 0.4762$ s, (b) $\Delta t = T/n = 0.4545$ s, (c) $\Delta t = T/n = 0.4$ s.

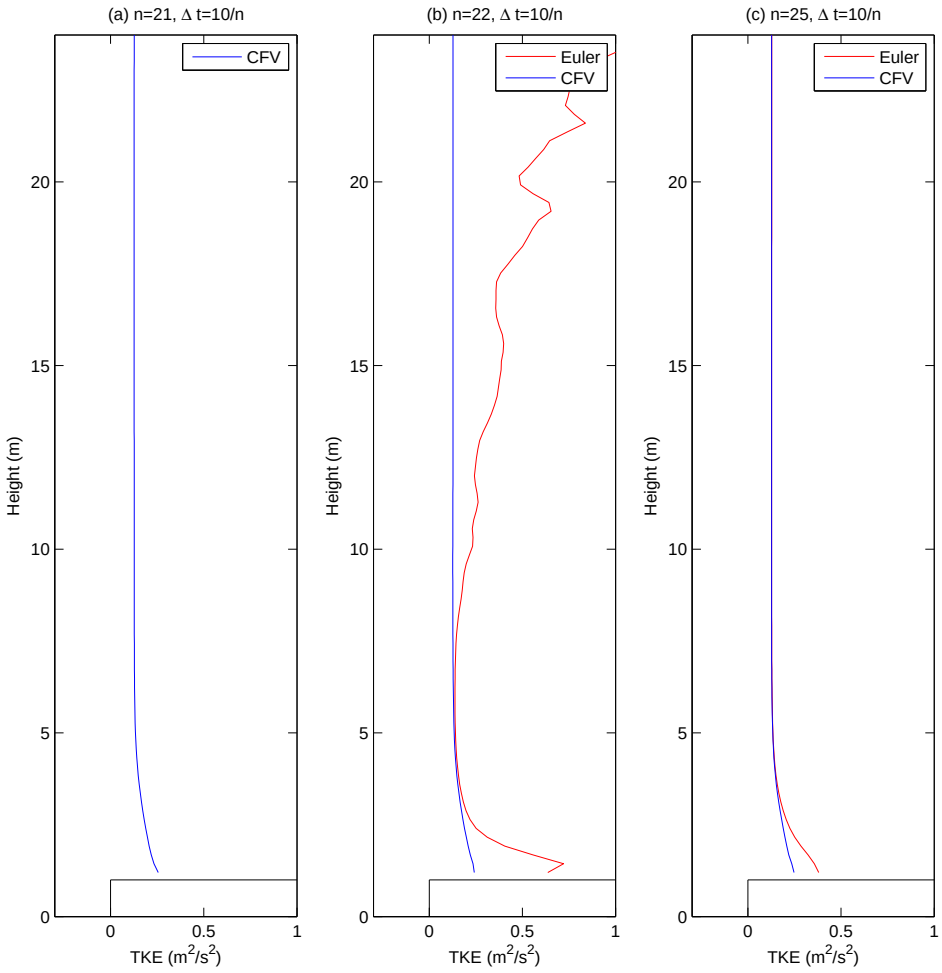

Figure 3.10: 2D cliff, cliff height=H, $z_0 = 0.01$ m, $u_* = 0.21$ m/s. $\Delta x = H/5 = 0.2$ m. Vertical profile of TKE, locate at $x = 7.5$ m and $T = 10$ s. (a) $\Delta t = T/n = 0.4762$ s, (b) $\Delta t = T/n = 0.4545$ s, (c) $\Delta t = T/n = 0.4$ s.

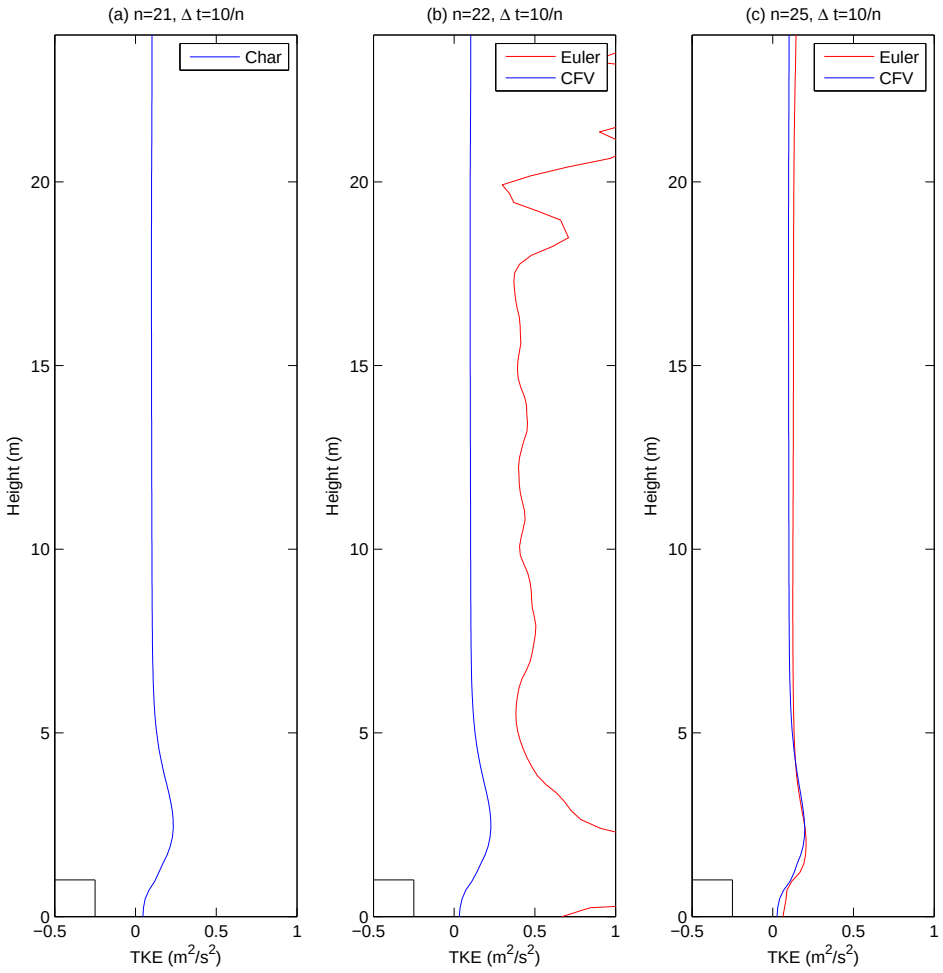

Figure 3.11: 2D cliff, cliff height=H, $z_0 = 0.01$ m, $u_* = 0.21$ m/s. $\Delta x = H/5 = 0.2$ m. Vertical profile of TKE, locate at $x = 27.5$ m and $T = 10$ s. (a) $\Delta t = T/n = 0.4762$ s, (b) $\Delta t = T/n = 0.4545$ s, (c) $\Delta t = T/n = 0.4$ s.

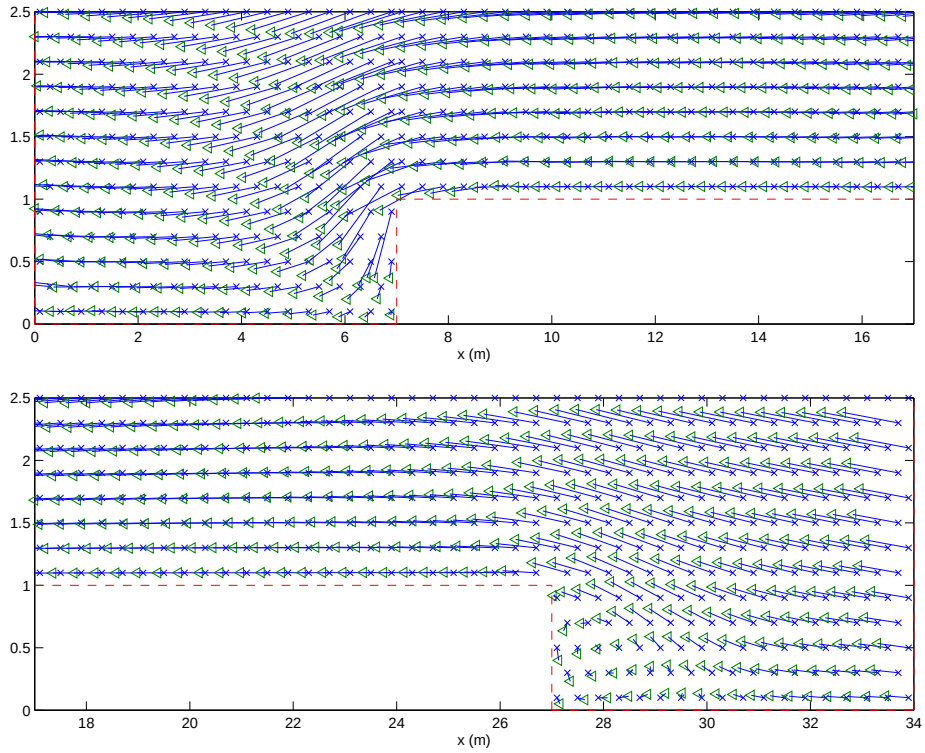

Figure 3.12: 2D cliff, cliff height=H, smooth surface, $z_0 = 0.01$ m, $u_* = 0.21$ m/s, $\Delta x = H/5 = 0.2$ m, $\Delta t = 0.5$ s.

ods predict a flow separation close to surface when $n = 25$, but the Euler method is broken when $n = 21$, while Characteristic method still gives a good prediction of flow separation at the same location. Vertical profiles of TKE are also compared in Figure 3.10 and 3.11 for two different locations.

The characteristic trajectories are plotted in Figure 3.12 when $z_0 = 0.01$ m and $\Delta t = 0.5$ s, in which case the Euler method fails to converge. From the trajectories we can see that the flow changes its direction on the upwind side of the cliff and separates on the downwind side of the cliff.

In order to observe flow separation region under different roughness, we compare the smooth surface ($z_0 = 0.01$ m) with the rough surface ($z_0 = 0.3$ m). We will also change the cliff height to see how it can influent the flow pattern. The time step size during computation is set to be $\Delta t = 0.2$ s for consistency in following tests. In Figure 3.13, the streamlines are plotted on the upwind side of the cliff, no flow separation is observed in the smooth surface case, but there is separation in the rough surface case with a diameter of 0.4 m. In Figure 3.14, flow separation is observed in both cases on the downside of the cliff. The smooth surface gives a region of 2 m in length and 0.8 m in height, while the rough surface gives a region of 1 m in length and 0.8 m in height. Not only change the surface roughness, we

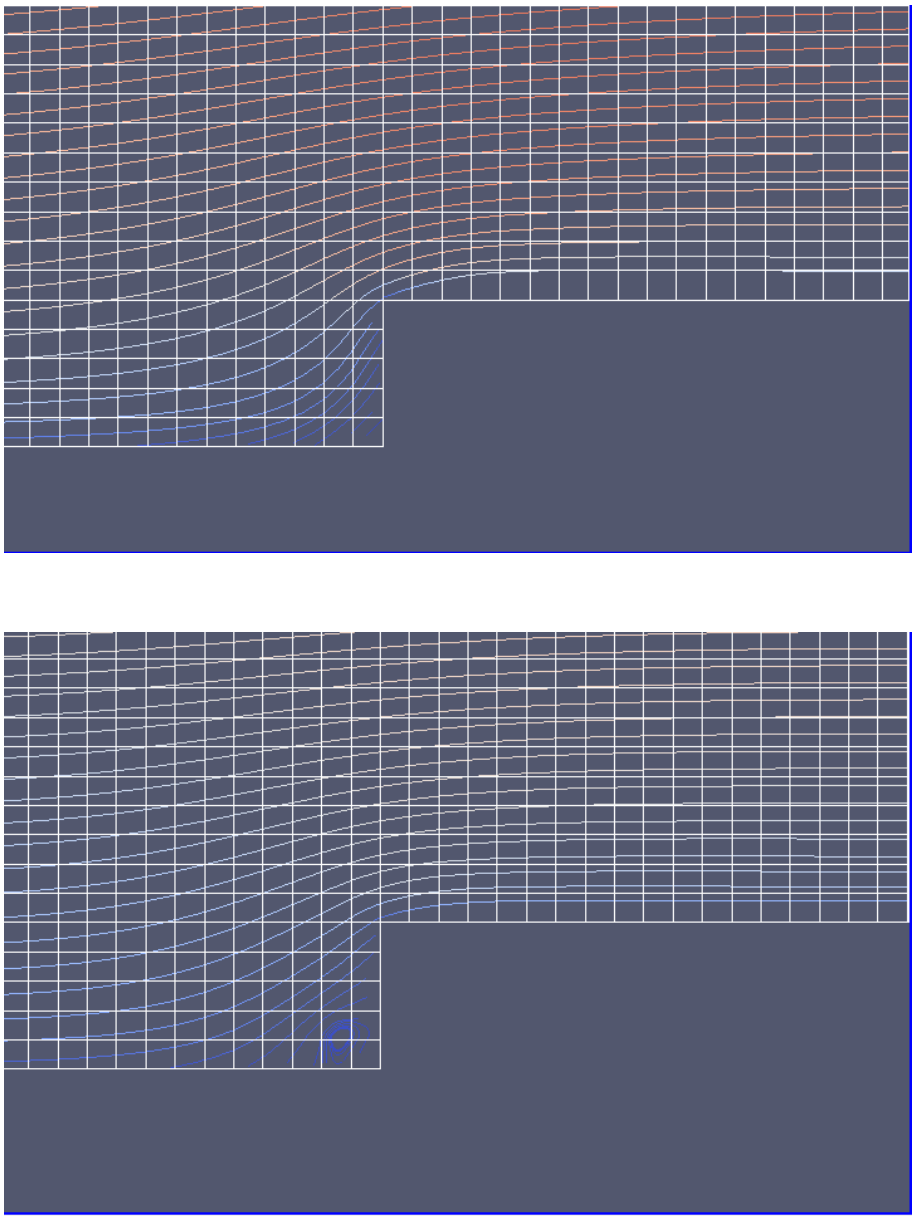

Figure 3.13: Streamline 2D cliff case, cliff height=H, $\Delta x = H/5 = 0.2$ m, $\Delta t = 0.2$ s. Left: Smooth surface $z_0 = 0.01$ m. Right: Rough surface $z_0 = 0.3$ m.

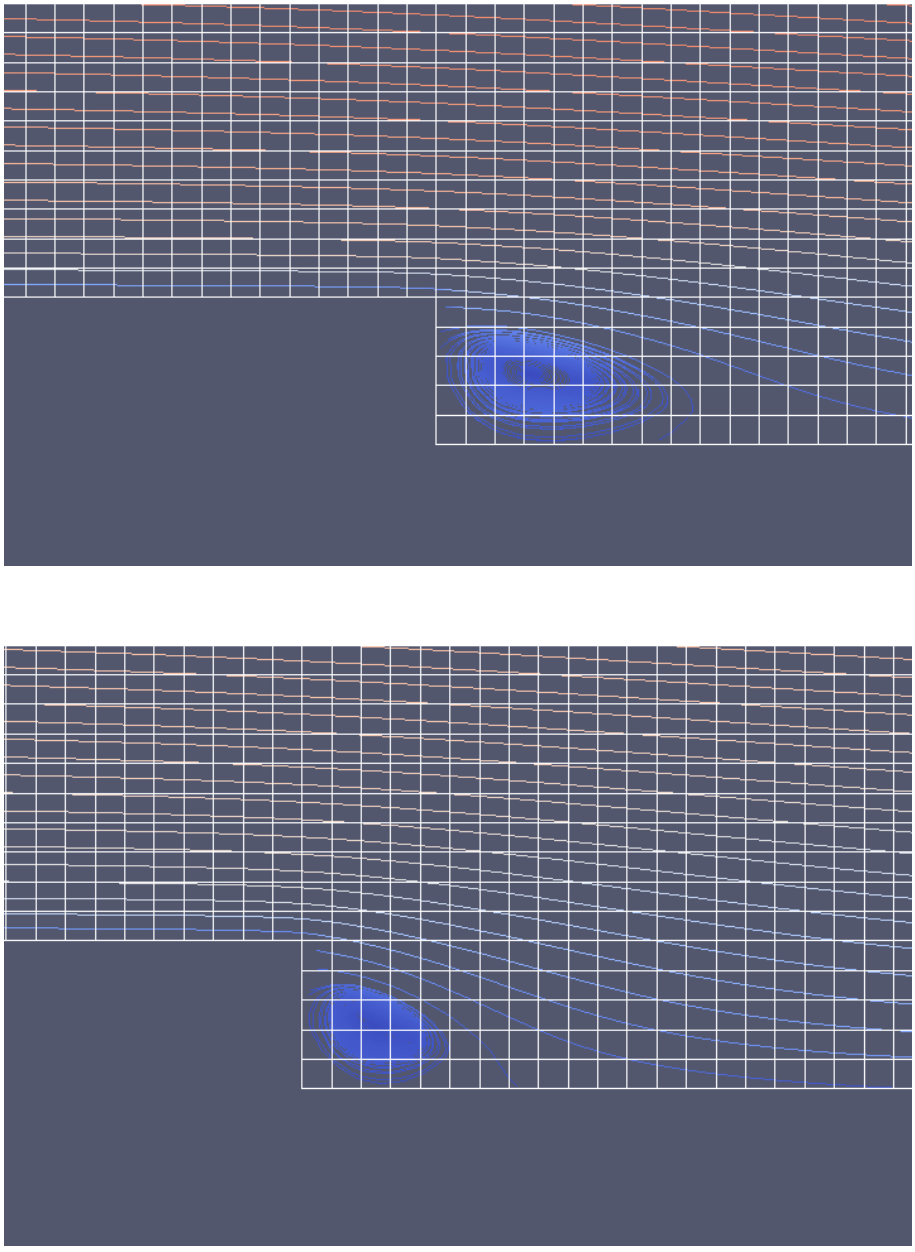

Figure 3.14: Streamline 2D cliff case, cliff height=H, $\Delta x = H/5 = 0.2$ m, $\Delta t = 0.2$ s. Left: Smooth surface $z_0 = 0.01$ m. Right: Rough surface $z_0 = 0.3$ m.

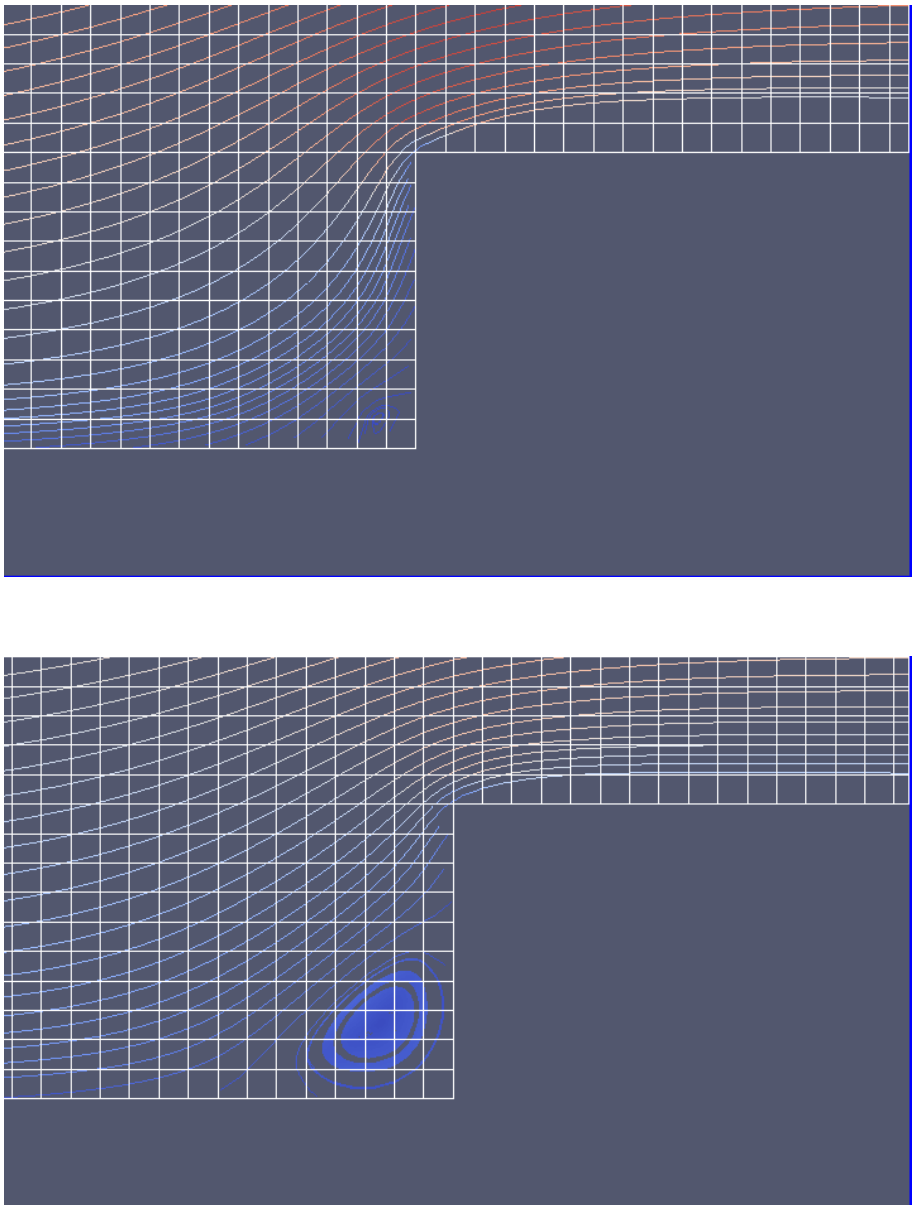

Figure 3.15: Streamline 2D cliff case, cliff height=$2H$, $\Delta x = H/5 = 0.2$ m, $\Delta t = 0.2$ s. Left: Smooth surface $z_0 = 0.01$ m. Right: Rough surface $z_0 = 0.3$ m.

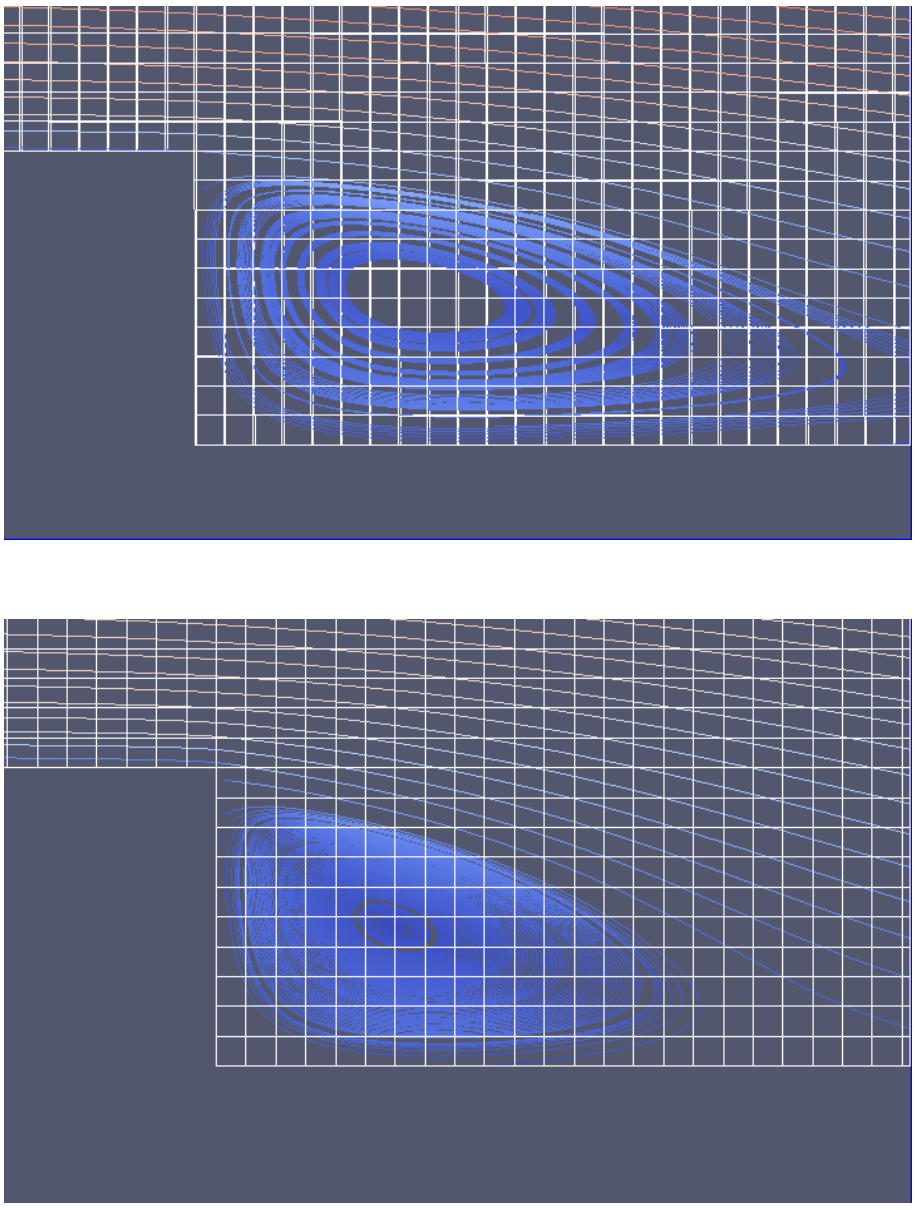

Figure 3.16: Streamline 2D cliff case, cliff height=$2H$, $\Delta x = H/5 = 0.2$ m, $\Delta t = 0.2$ s. Left: Smooth surface $z_0 = 0.01$ m. Right: Rough surface $z_0 = 0.3$ m.

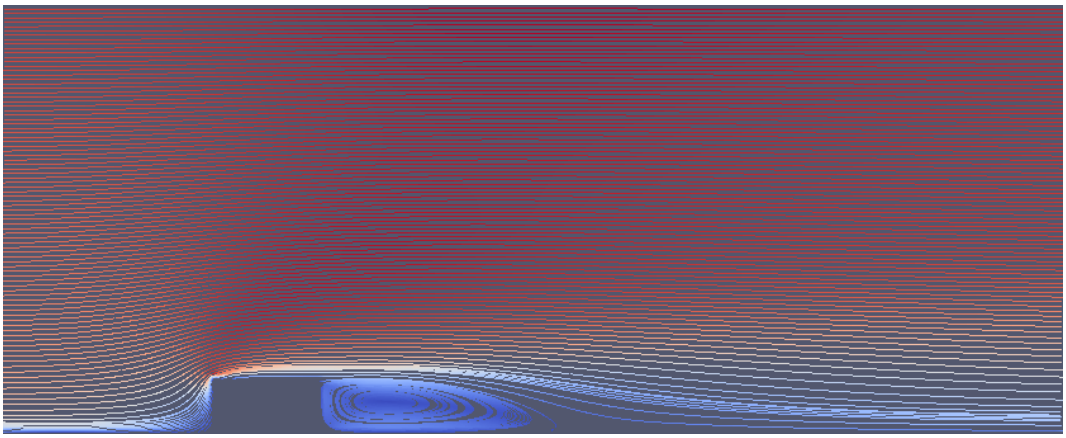

Figure 3.17: 2D block case, $\Delta t = 1$ s, $\Delta x = 0.5$ m, $T = 30$ s, $z_0 = 0.01$ m, $u_* = 0.3$ m/s. Distance=0 m.

also change the cliff height to be $2H$ in the following test. In Figure 3.15, when the cliff height is two times as before, flow separation can be now observed in the smooth surface case on the upwind side of the cliff, and a larger separation region is also observed in the rough surface case with a diameter of 1 m. In Figure 3.16, the separation region is also larger than the one in Figure 3.14, here the smooth surface gives a region of 5 m in length and 1.8 m in height and the rough surface gives a region of 3.4 m in length and 1.8 m in height.

In order to test the Characteristic Finite Volume method on a more complex and steep topography, we consider multiple blocks on ground. The computation domain is now 100 m in x direction and 40 m in z direction, the size of each block is

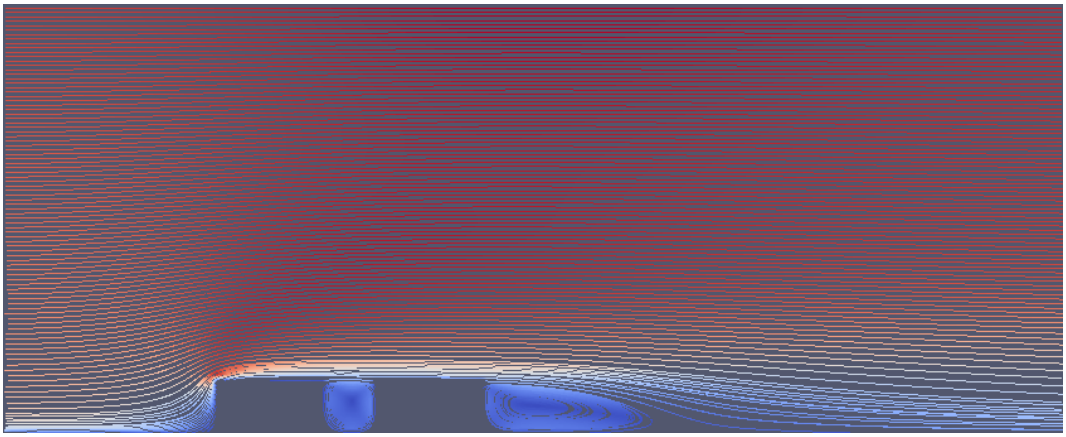

Figure 3.18: 2D block case, $\Delta t = 1$ s, $\Delta x = 0.5$ m, $T = 30$ s, $z_0 = 0.01$ m, $u_* = 0.3$ m/s. Distance=5 m.

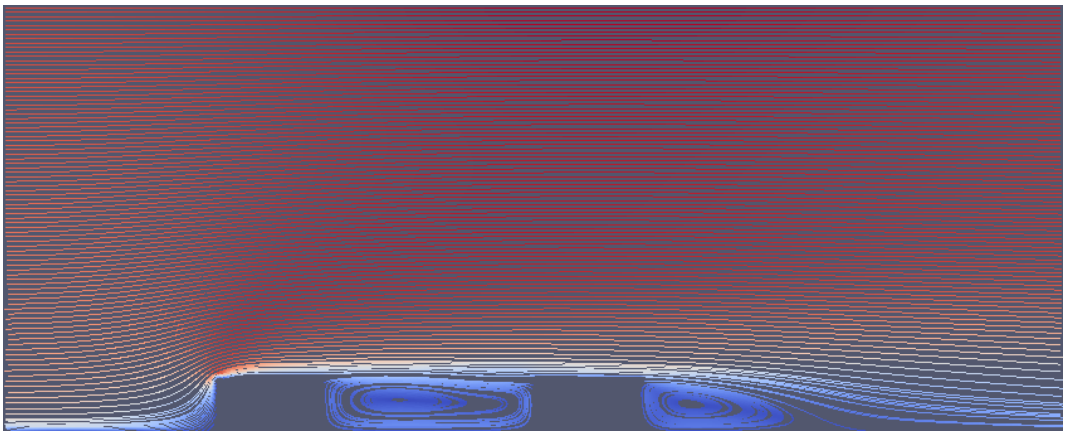

Figure 3.19: 2D block case, $\Delta t = 1$ s, $\Delta x = 0.5$ m, $T = 30$ s, $z_0 = 0.01$ m, $u_* = 0.3$ m/s. Distance=20 m.

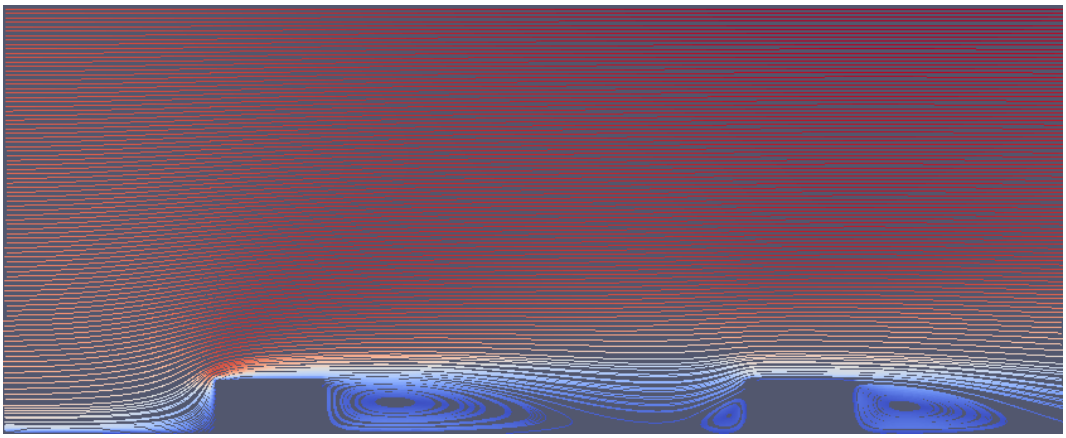

Figure 3.20: 2D block case, $\Delta t = 1$ s, $\Delta x = 0.5$ m, $T = 30$ s, $z_0 = 0.01$ m, $u_* = 0.3$ m/s. Distance=40 m.

10 m in length and 5 m in height. We simulate the air flow over topography under the situations that the distance between two blocks are 0 m, 5 m, 20 m, and 40 m. Boundary conditions remain the same as those mentioned at the beginning of this section, only the inlet velocity U_x has a reference speed of $U_{ref} = 10$ m/s and a reference height of $H_{ref} = 40$ m. Numerical results are carried out under $\Delta x = 0.5$ m and $\Delta t = 1$ s, in which the Euler method fails to converge. In Figures 3.17, 3.18, 3.19, 3.20, streamlines are plotted after a simulation of $T = 30$ s. We can observe different patterns of the separation region between two blocks. And when the distance is large (40 m), the separation region splits into two isolated regions.

3.7 Simulation over realistic terrain, Bolund hill

To simulate wind flow over a realistic topography, [11] and [8] conducted a field campaign on Bolund hill, a small island in Roskilde, Denmark. The dimension of the hill is 12 m in height, 130 m in length, 75 m in width. The roughness changes from water surface ($z_0 = 0.0003$ m) to grassland ($z_0 = 0.015$ m). One of the main challenges of this terrain is the steep escarpment which occurs on the western side of the hill. The maximum slope of the terrain is up to 1.2, which causes a computational crash from the Non-linear Mixed Spectral and Finite Difference (NLMSFD) method, which is used previously. In this section, we apply the Characteristic Finite Volume method on the time-dependent RANS equations and $k-\varepsilon$ model. The two-dimensional model is used to simulate wind flow over the cross sections of the Bolund hill, which are line B and line A (refer to Chapter 2).

In the field campaign, ten masts were used to collect wind data. We focus on the cases when wind direction is 270° on Line B and 240° on Line A. The friction velocity is set to be $u_* = 0.4$ m/s, and upstream TKE is $k_0/u_*^2 = 5.8$. We use the roughness of water surface ($z_0 = 0.0003$ m) as upstream inlet wind profile, and the computation domain is 800 m in x-direction and 500 m in z-direction. Boundary conditions are used same as Section 3.6. In numerical simulation, wind flow is simulated for $T = 100$ s, which is long enough to reach a steady state. A time step

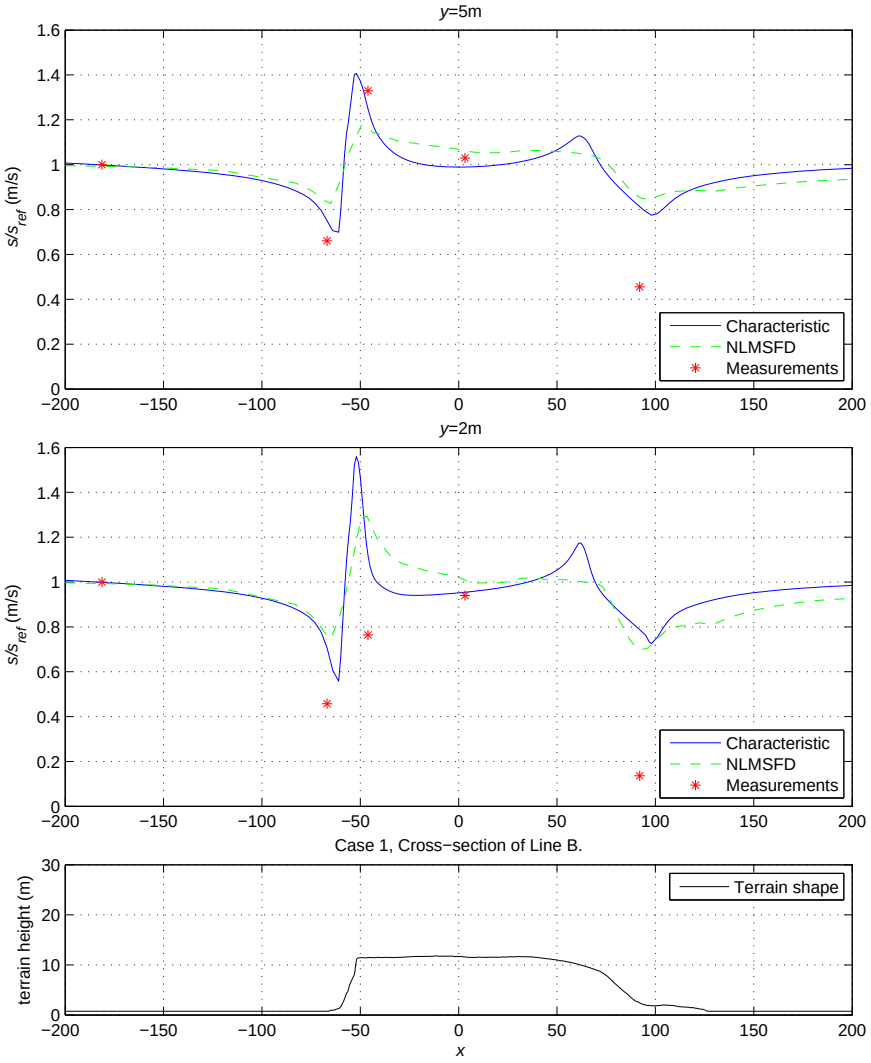

Figure 3.21: Surface velocity on Line B.

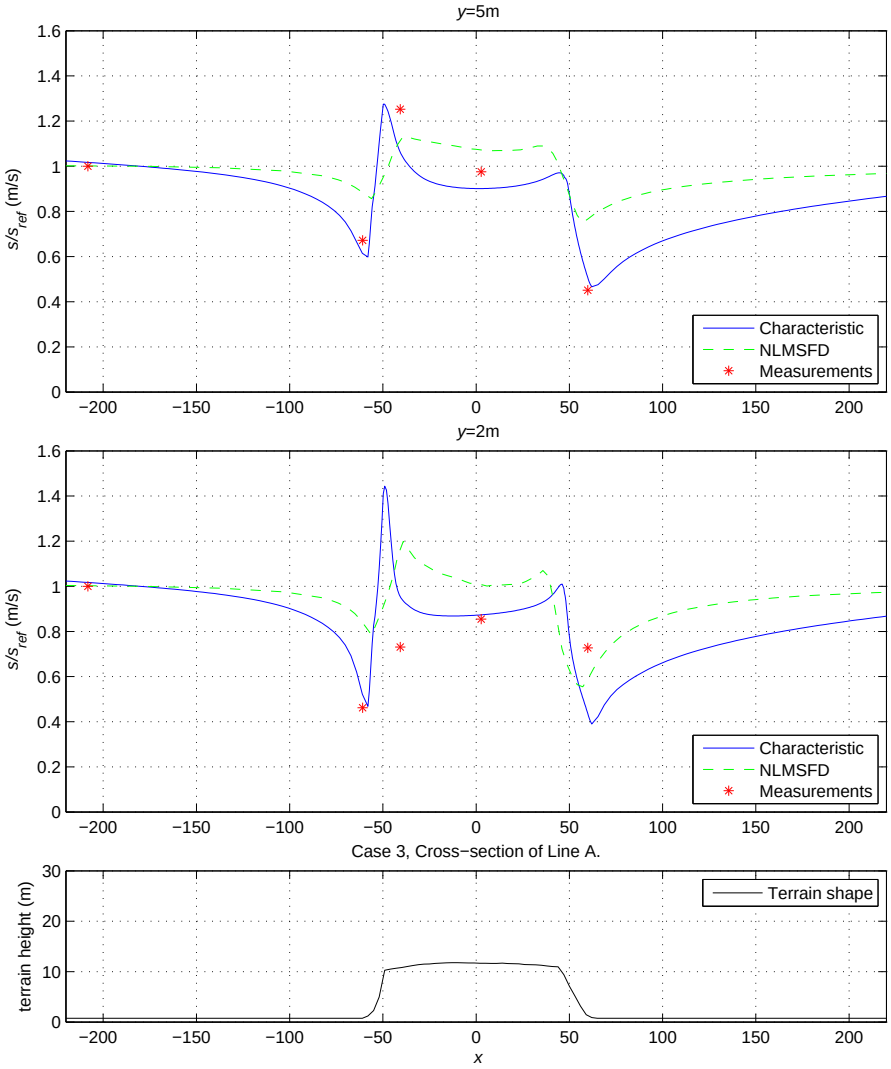

Figure 3.22: Surface velocity on Line A.

$\Delta t = 0.1$ s is used, from where the Euler method fails to converge.

In Figure 3.21 and Figure 3.22, we plot the normalized surface velocity s/s_{ref} 2 m and 5 m from terrain surface, where s is the total velocity $s = (U^2+V^2+W^2)^{1/2}$, s_{ref} is the reference total velocity at the upstream location. Results in both cases show a good agreement at the upwind side of the hill and the hill top. In Figure 3.22 there is a good agreement at the lee side of the hill, but there are under-predictions in Figure 3.21, which is believed as the limitation of the two-dimensional model over the three-dimensional realistic terrain.

4 Modelling Wind Flow and Turbine Wakes in Large Wind Farms by the CFV Method

In this chapter, we apply the characteristic finite volume method developed in Chapter 3 to simulate wind flow and turbine wakes in large wind farms. The time dependent Reynolds Averaged Navier-Stokes (RANS) equations are used as model equations that are coupled by the $k-\varepsilon$ equations. The effect of the wind turbines is considered as a higher surface roughness than the surroundings. Wake effect from neighboring turbines is studied in order to determine how efficiently the potential energy can be converted. Taking into account the effect of wind farms on the topography, one can consider a surface roughness change for the wind farm area such as [26], [18], [25]. Studying wind turbine wakes is useful on measuring how efficiently the wind farm is able to capture the available potential energy in the atmosphere. The roughness change is also studied by [73] and [85]. The object is to predict the recovery of the wind speed downwind of an existing wind farm. We consider the large scale model such that a cluster of wind farms is treated as a

roughness element. Small scale models are introduced by [45], which used a $k-\varepsilon$ model to simulate flow through a horizontal-axis wind turbine. Other concept such as adding the drag force and treat the group of roughness elements as a canopy is introduced by [9], [27]. In this chapter, the roughness change models are applied. Wind farms can be considered from one large wind turbine group to many smaller wind farm over a region. We simulate the wakes from a cluster of wind farms by considering the case as one large wind farm or several small wind farms. We present the results for the case with one block, two blocks, three blocks, and ten blocks. Wind speed reductions and recoveries are shown and an asymptote can be predicted with infinite blocks. We also propose to consider RANS equations with Coriolis Effect for modelling wind flows over a large wind farms due to the rotation of Earth. The wind flows within and downwind of the wind farms are predicted numerically. Simulation results on the Horns Rev wind farm are compared with field measurements in [35] and [5].

4.1 Roughness Treatment on Large Wind Farms

To model large wind farm we treat the effect of the wind turbines as roughness changes. Thus the lower boundary of the computation domain is treated as having different roughness patches. Wall functions are used on such patches in order to describe the changes on surface roughness. To demonstrate this model, we use

RANS equations with $k-\varepsilon$ closure. The inlet boundary conditions are a logarithm profile for $\mathbf{U}$ and an inverse linear profile for ε,

$$
\begin{aligned}
U_1 &= \frac{u_*}{\kappa}\ln\left(\frac{z+z_0}{z_0}\right), U_2 = U_3 = 0, && (4.1)\\
\frac{\partial P}{\partial x} &= 0, && (4.2)\\
k &= \frac{u_*^2}{c_\nu^{1/2}}, && (4.3)\\
\varepsilon &= \frac{c_\nu^{3/4}k^{3/2}}{\kappa(z+z_0)}. && (4.4)
\end{aligned}
$$

The outlet boundary conditions are

$$
\begin{aligned}
\frac{\partial \mathbf{U}}{\partial x} &= 0, && (4.5)\\
P &= 0, && (4.6)\\
\frac{\partial k}{\partial x} &= 0, && (4.7)\\
\frac{\partial \varepsilon}{\partial x} &= 0. && (4.8)
\end{aligned}
$$

For the lateral boundary the symmetric condition is applied. On the top boundary,

$$
\begin{aligned}
\frac{\partial \mathbf{U}}{\partial z} &= 0, && (4.9)\\
\frac{\partial P}{\partial z} &= 0, && (4.10)\\
\frac{\partial k}{\partial z} &= 0, && (4.11)\\
\frac{\partial \varepsilon}{\partial z} &= 0. && (4.12)
\end{aligned}
$$

For the lower boundary, we consider the bottom faces of the control volume as patches with different surface roughness. Therefore the wall functions are used on the lower boundary. The wall function for k is simply a zero-gradient condition. The wall function for ε is that an equilibrium assumption is used between production and dissipation of TKE combined with the logarithmic law of the wall, which gives

$$\varepsilon = \frac{C_\mu^{3/4} k^{3/2}}{\kappa z_p + z_0}, \tag{4.13}$$

where z_p is the z-coordinate of the first node, at which ε is computed. The wall function for ν_t is used for a rough wall based on the law of the wall. We can control the roughness of the domain throughout the specification of Nikuradse's roughness length k_s and the roughness constant C_s in [34]. The following relation is used at wall,

$$\frac{u_p}{u_*} = \frac{1}{\kappa} \ln \left(\frac{E z_p^+}{1 + C_s k_s^+} \right), \tag{4.14}$$

where E is the smooth wall constant $E = e^{\kappa B}$ and B is the smooth log law constant taken as 5.2. C_s is used for taking into account the roughness type and it takes the value between 0.2 and 1. $z_p^+ = \frac{u_* z}{\nu}$ is the dimensionless z coordinate at z_p and $k_s^+ = \frac{u_* k_s}{\nu}$ is the dimensionless roughness height k_s. Consider the fully rough regime as the complex rough terrain, the rough log law can be re-written as

$$\frac{u_p}{u_*} = \frac{1}{\kappa} \ln \left(\frac{E z_p}{C_s k_s} \right). \tag{4.15}$$

To find a prescribed value of k_s in this wall function, we compare the inlet condition of velocity and assume that the first cell node must be considered much bigger than the roughness length. We can get

$$k_s = \frac{Ez_0}{C_s} = 19.58z_0. \tag{4.16}$$

which means that the value of k_s depends on the surface roughness of each patch.

As analyzed previously, we can consider the wind farms as several higher roughness than the surrounding area based on [1] and [28]. Given the terrain surface roughness, different wind farms are treated as different patches on the terrain surface. The roughness of such patch can be determined by the following formula. In Figure 4.1, the roughness z_{00} can be calculated as

$$z_{00} = h_H \exp\left(-\frac{\kappa}{\sqrt{c_t + [\kappa/\ln(h_H/z_0)]^2}}\right) \tag{4.17}$$

where κ is the von Karman constant, h_H is the wind turbine hub height, z_0 is the roughness of the terrain surface and c_t is given as

$$c_t = \frac{\pi C_T}{8 \cdot d_r/D \cdot d_f/D} \tag{4.18}$$

where C_T is the thrust coefficient of the rotor which can be vary between 0 and 1, d_r is the distance to the next wind turbine in the same row, and d_f is the distance to the neighboring rows. For example, the turbines in a wind farm is evenly distributed,

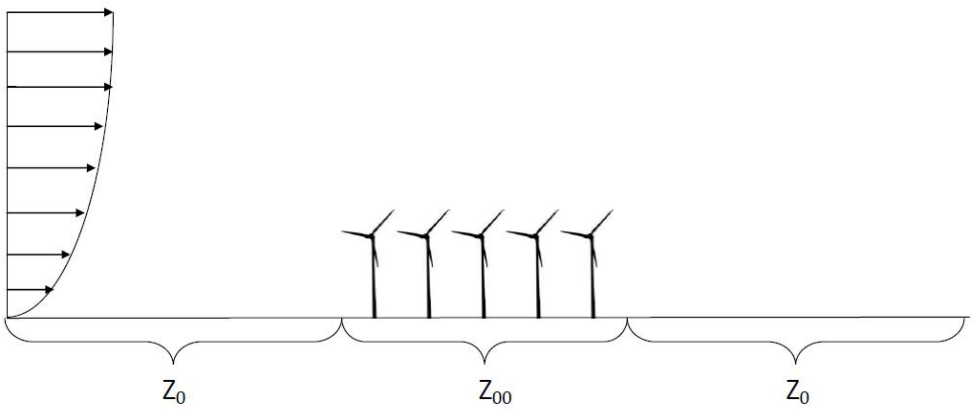

Figure 4.1: Wind turbines as roughness element.

and the distance between each turbine is $7D$ where D is the rotor diameter. Hub height of each turbine is 100 m. If the wind speed at hub height is approximately 14 m/s, a typical C_T is 0.6. Thus the following value of the parameters are chosen,

$$d_r = d_f = 7D,\ C_T = 0.6,\ h_H = 100\ m,$$

If the terrain roughness is $z_0 = 0.0002$ m, the roughness of this wind farm is $z_{00} = 0.5$ m from Equation (4.17).

4.2 Simulation on Large Offshore Wind Farms

In this section, we conduct numerical experiments on large offshore wind farms by using the developed characteristic finite volume method. We treat large scale

Table 4.1: Experiments on 2D model

Number of wind farms	size of wind turbine group (km)	Distance between groups (km)
1	30	–
2	15	15
3	10	10
10	3	3

wind farms as roughness elements. Experiments with similar treatment can be found in [26]. The surface roughness length for open water is set to be 0.0002 m, the roughness for the wind farm is 0.5 m. Experiments have been conducted on different wind farm configurations shown in Table 4.1 under a two-dimensional assumption. The total area is fixed for 900 km^2.

In Figure 4.2, one wind farm is located at $x = 50$ km and the size of the wind farm is 30 km in length. The grid size in the horizontal direction is $\Delta x = 1$ km and the vertical gird is uniformly graded with a ratio of 10. The time step $\Delta t = 100$ s. The simulation of all four cases are lasting for 20000 s to reach a stable state. The horizontal velocity profile at $z = 50$ m is presented in Figure 4.2(a) where the upstream velocity at the height of 50 m is used as reference velocity U_{ref}. The wind

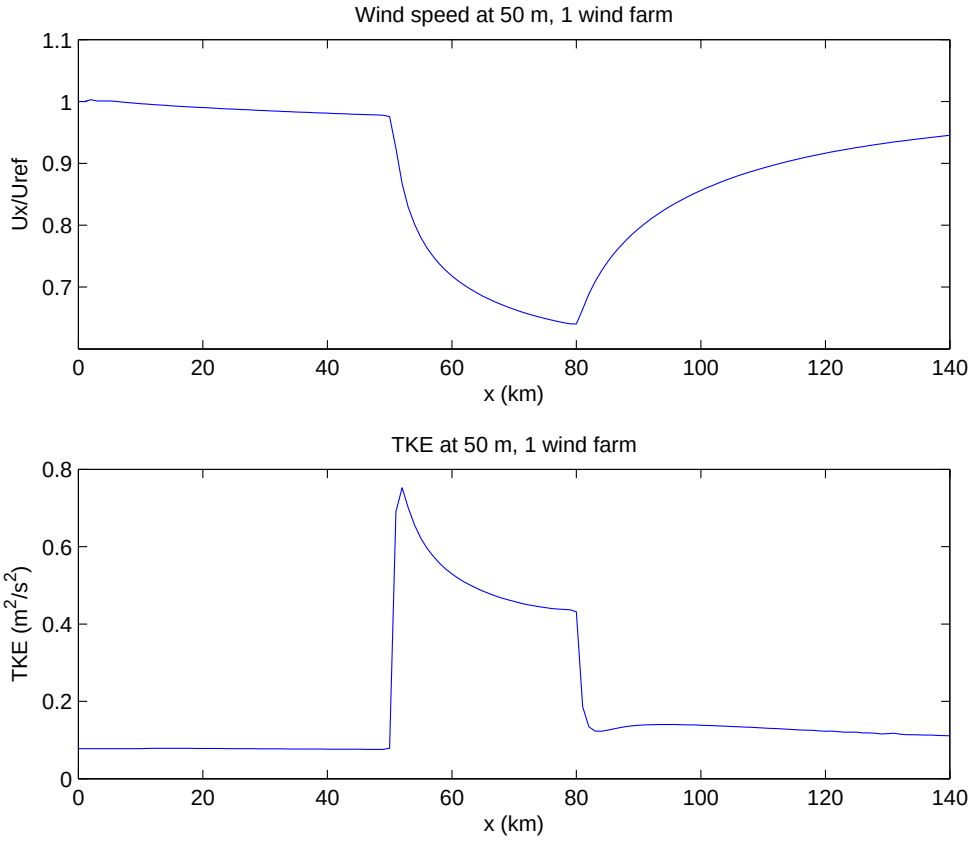

Figure 4.2: Horizontal velocity and TKE profile at z=50 m, one farm case.

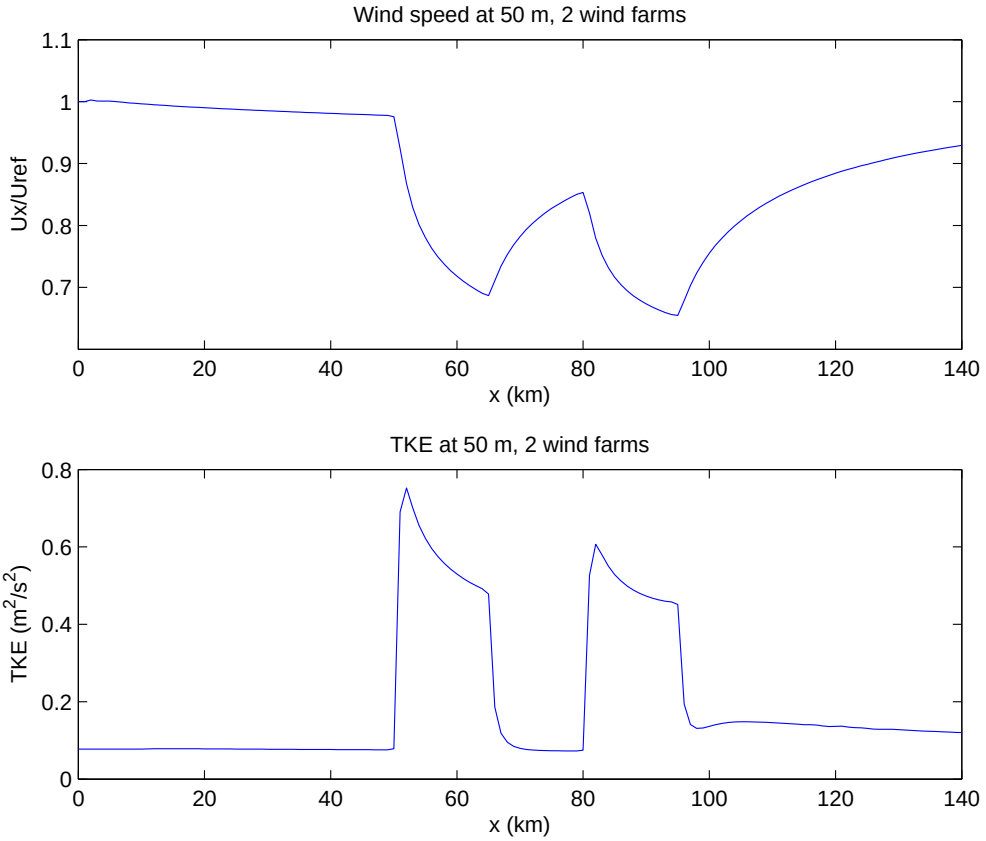

Figure 4.3: Horizontal velocity and TKE profile at z=50 m, two farms case.

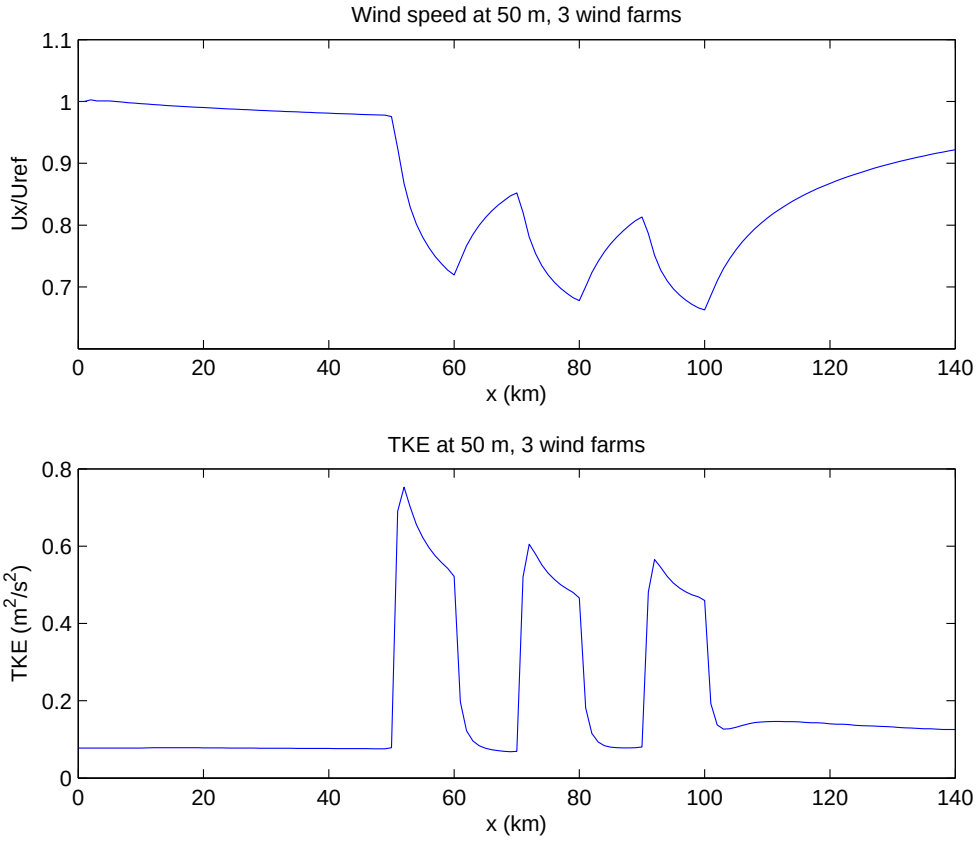

Figure 4.4: Horizontal velocity and TKE profile at z=50 m, three farms case.

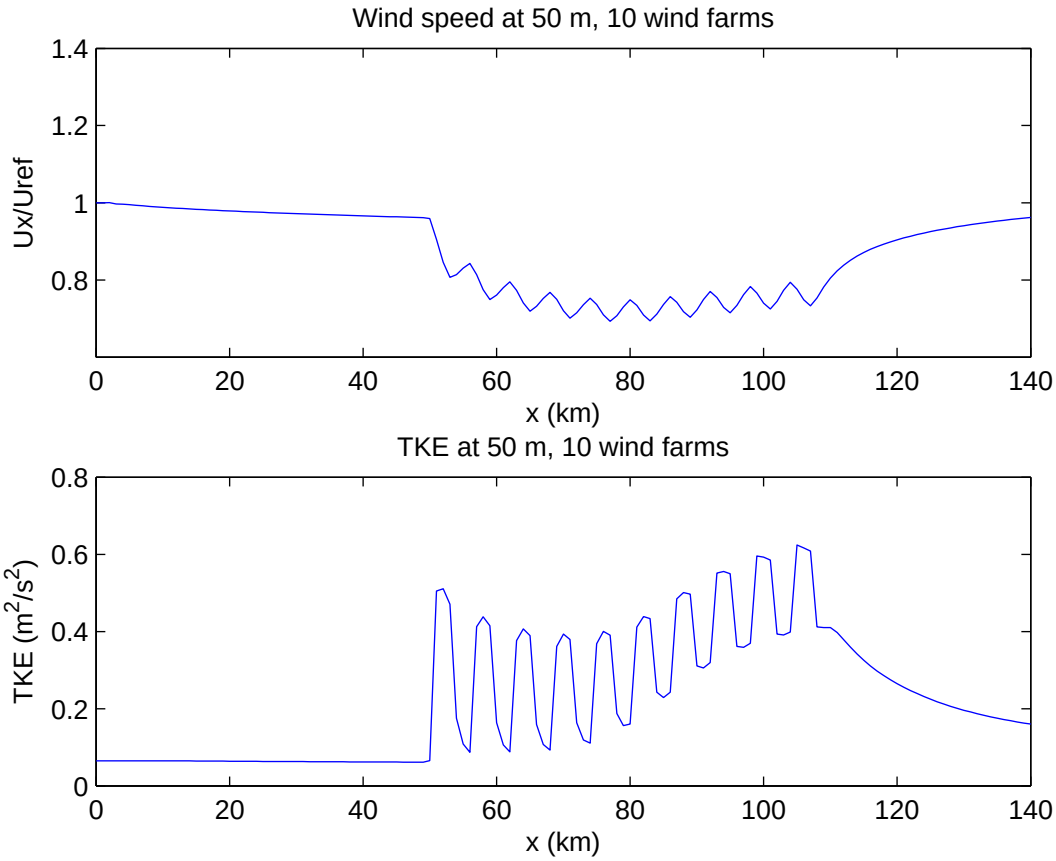

Figure 4.5: Horizontal velocity and TKE profile at z=50 m, ten farms case.

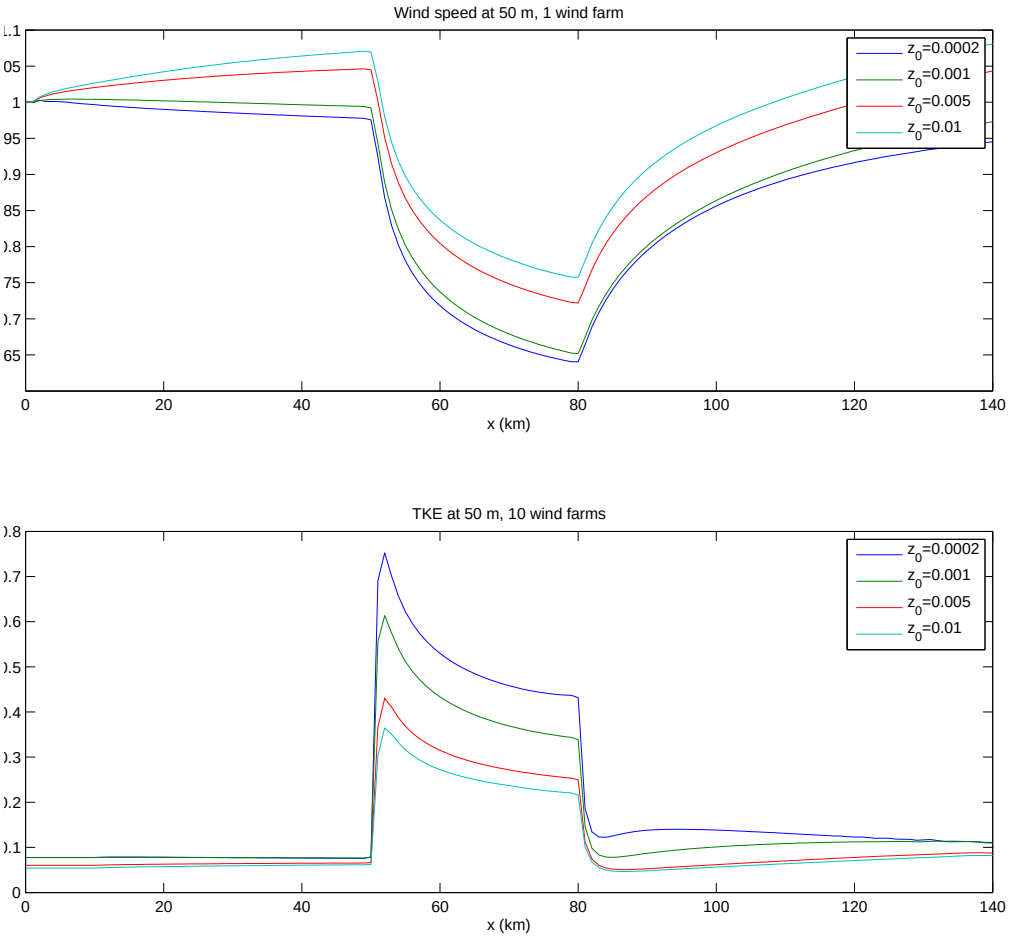

Figure 4.6: Horizontal velocity and TKE profile at z=50 m, under different roughness.

speed reduces from $x = 50$ km and recovers at $x = 80$ km. The horizontal TKE profile at $z = 50$ m is presented in Figure 4.2(b). A large variation occurs at the location of the wind farm. The results for two, three, ten wind farms are further given in Figure 4.3, Figure 4.4, and Figure 4.5.

For all four cases, the effect of the higher roughness of the wind farm can be observed as the wind speed reduction downwind of the turbine groups. The reduction of the wind speed within the groups can also be observed. The rate of reduction decreases with distance into the turbine group. For the case with ten wind farms, the wind speed inside the wind turbine group approaches an asymptote, at which point the wind farm roughness has led to full development of the wind speed profile. The downwind wind speed recovery or wake decay looks similar in all cases. Recovery to flow speed upwind of the turbine groups takes around 50 km. When the distance between turbine groups is small, there is a reduced recovery.

We also test the one wind farm case under different inlet surface roughness. Figure 4.6 shows the horizontal velocity profile of $z_0 = 0.01, 0.005, 0.001, 0.0002$ m. The higher surface roughness predicts smaller wind speed reduction and less TKE oscillation.

Table 4.2: Experiments on 3D model

Number of wind farms	size of wind turbine group (km)	Distance between groups (km)
1×1	30×30	–
2×2	15×15	15
3×3	10×10	10

The three-dimensional model is also considered to test the following cases in Table 4.2. In the case of one wind farm, the location of wind farm starts at x=50 km and y=50 km. The size of wind farm is 30×30 km^2. In the case of four wind farms, the locations of wind farms start at x=50 km and y=50 km. The size of the wind farm is 15×15 km^2 and the distance between two wind farms is 15 km. In the case of the nine wind farms, the locations of wind farms start at x=50 km and y=50 km. The size of wind farm is 10×10 km^2 and the distance between two wind farms is 10 km. The contour plots from Figure 4.7 to Figure 4.15 show the horizontal velocity field at heights of z=50, 70, 100 m. Large wind farm is given as patch(es) with higher surface roughness. The wind direction is from west to east. Wind speed deficit is shown on the downwind side of the patch(es).

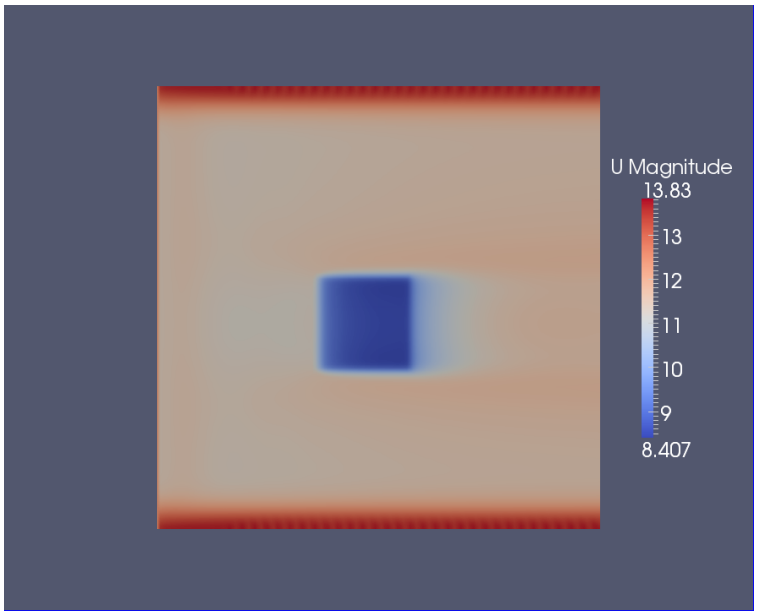

Figure 4.7: Contour plot of one wind farm at z=50 m.

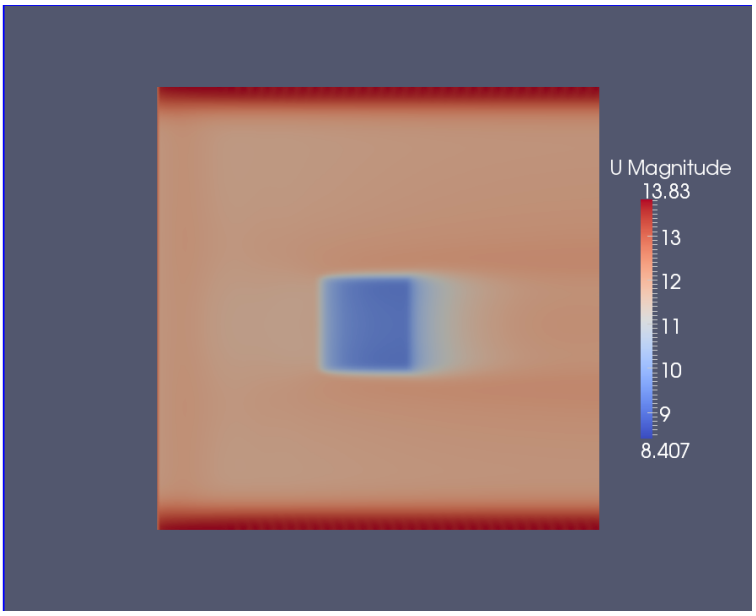

Figure 4.8: Contour plot of one wind farm at z=70 m.

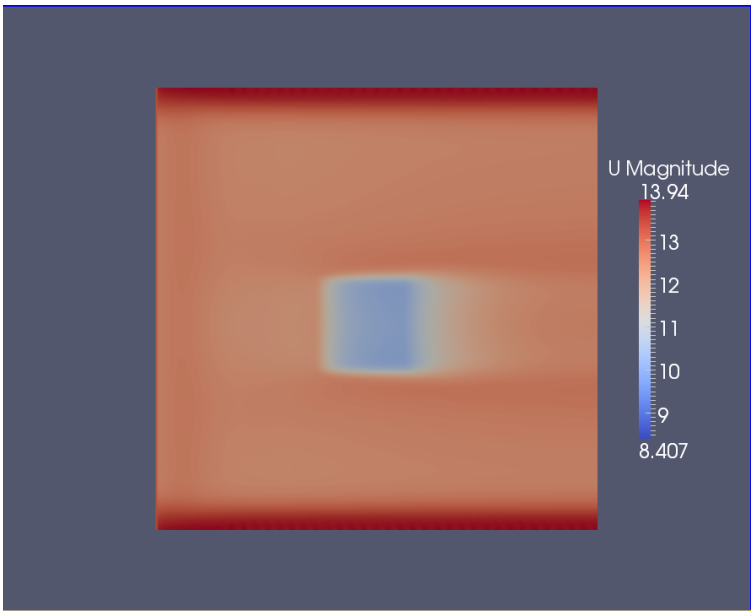

Figure 4.9: Contour plot of one wind farm at z=100 m.

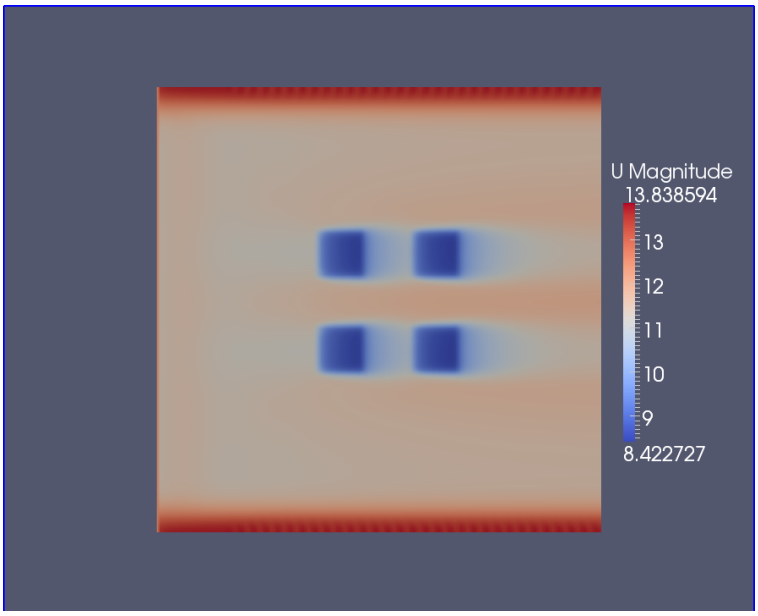

Figure 4.10: Contour plot of four wind farms at z=50 m.

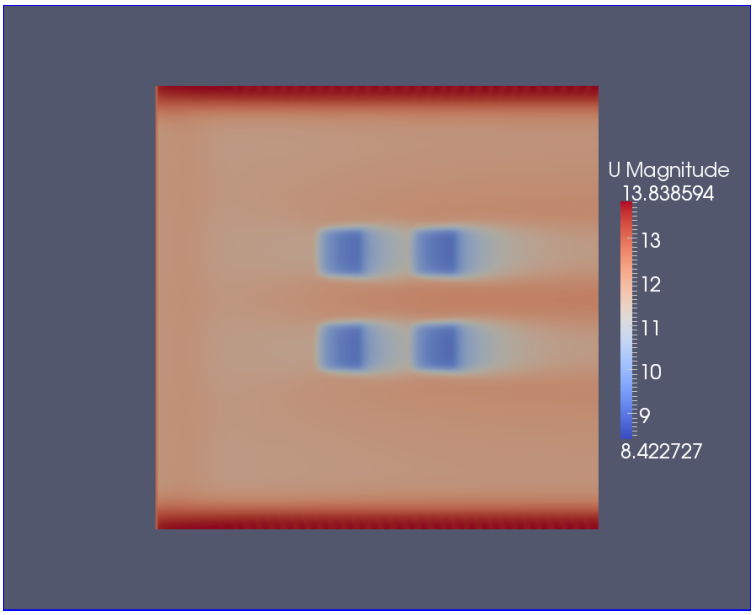

Figure 4.11: Contour plot of four wind farms at z=70 m.

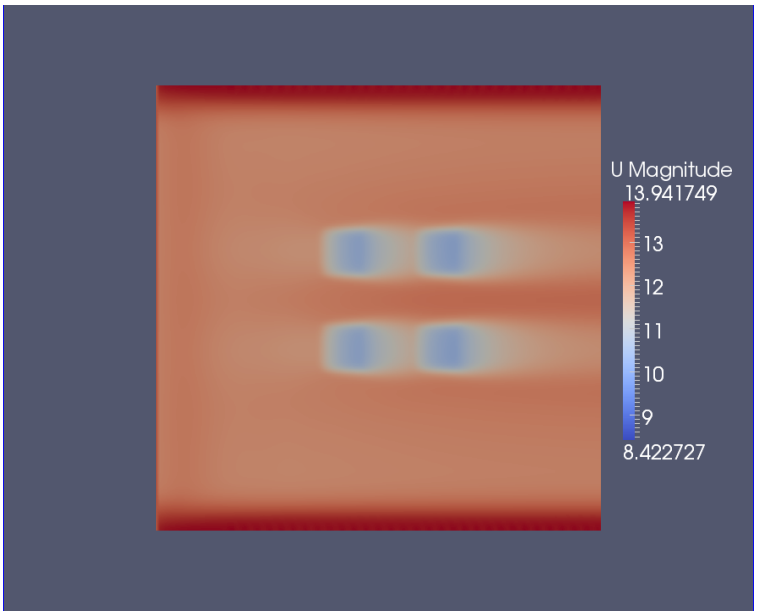

Figure 4.12: Contour plot of four wind farms at z=100 m.

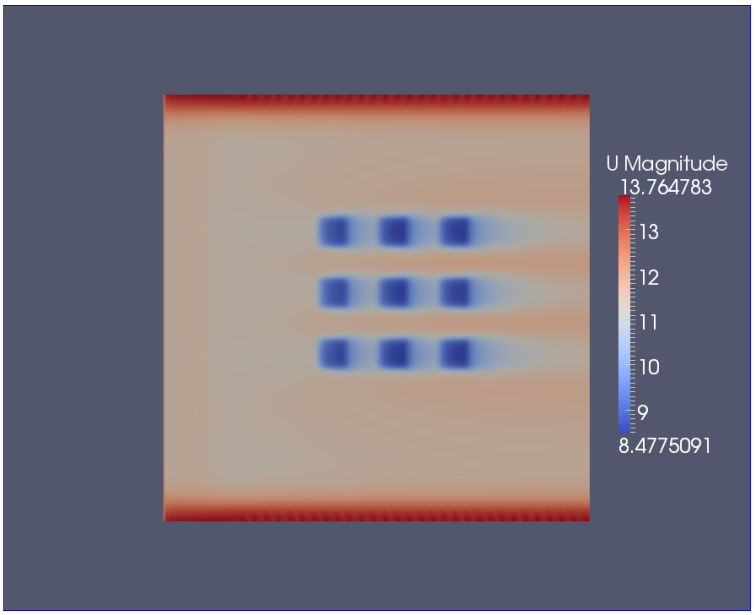

Figure 4.13: Contour plot of nine wind farms at z=50 m.

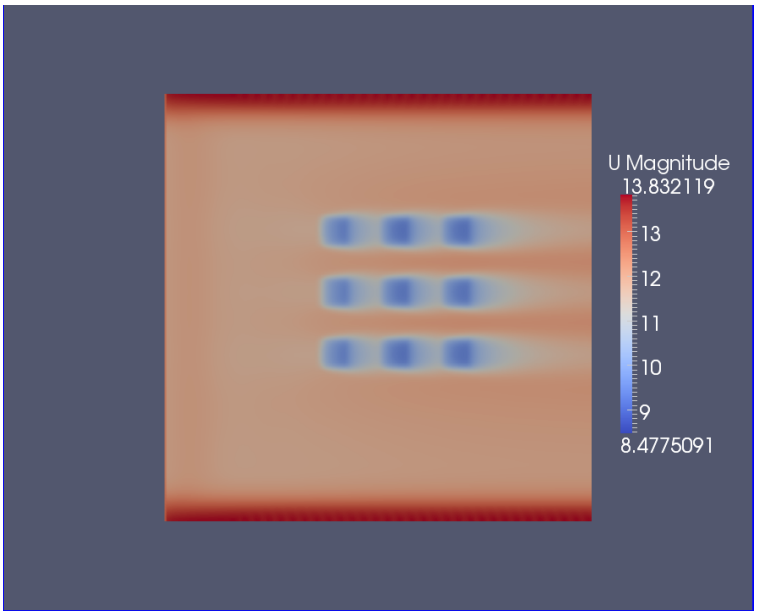

Figure 4.14: Contour plot of nine wind farms at z=70 m.

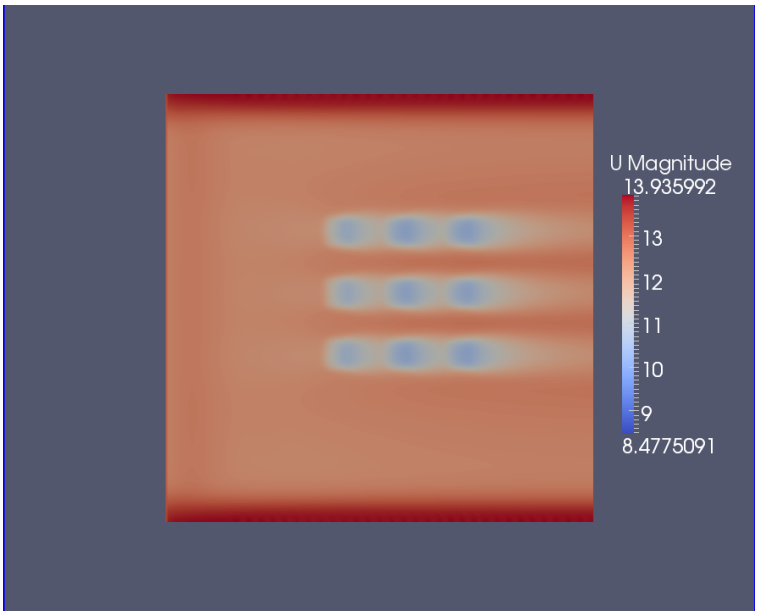

Figure 4.15: Contour plot of nine wind farms at z=100 m.

4.3 Simulation on Large Wind Farms Under the Coriolis Effect

In this section, we consider the Coriolis Effect on the wind flows in large wind farms. The Coriolis Force is proposed to be added to the momentum equations of the RANS models. In order to consider the large scale wind farms, wind flow under Coriolis effect need to be taken into account due to the rotation of Earth. The Coriolis force under unit mass can be considered as

$$\mathbf{F_c} = -2\mathbf{\Omega} \times \mathbf{U}, \tag{4.19}$$

where

$$\mathbf{U} = (U_1,\ U_2,\ U_3)^T, \tag{4.20}$$

$$\mathbf{\Omega} = \omega \cdot (0,\ 0,\ \sin(\varphi))^T. \tag{4.21}$$

Ω is the rotation rate vector, ω is the planetary rotation rate (rad/s), and φ is the latitude. As it is standard in Planetary Boundary Application, the horizontal components of rotation are ignored and the calculation is made on an f-plane.

The importance of the rotation effect can be determined by the Rossby number which is defined as

$$\mathrm{Ro} = \frac{U_{ref}}{2\omega \sin(\varphi) L}, \tag{4.22}$$

where U_{ref} is the velocity scale and L is the length scale. If the Rossby number is small, the rotation effect should be considered as dominant (as in geostrophic theory). If the Rossby number is very large, the rotation effect can be neglected. For example, the rotation rate of the earth is approximately 7.3×10^{-5} s^{-1}. Given a length scale of 50 km and a velocity scale of 10 m/s, the Rossby number at 45° N would be approximately 2, indicating that Coriolis terms are required.

Thus the RANS equations of $\mathbf{U}$, k, ε with Coriolis Effect are

$$\begin{aligned}
\rho\frac{\partial}{\partial t}U_i + \rho U_j\frac{\partial}{\partial x_j}U_i &= -\frac{\partial P}{\partial x_i} + \frac{\partial}{\partial x_j}\left(\mu\left(\frac{\partial U_i}{\partial x_j} + \frac{\partial U_j}{\partial x_i}\right) - \rho\overline{u_i' u_j'}\right) \\
&\quad -\epsilon_{ijk}\Omega_i(U_i - U_i g), \qquad (4.23)\\
\frac{\partial U_i}{\partial x_i} &= 0, \qquad (4.24)\\
\rho\frac{\partial}{\partial t}k + \rho U_j\frac{\partial}{\partial x_j}k &= \frac{\partial}{\partial x_j}\left[\left(\mu + \frac{\mu_t}{\sigma_k}\right)\frac{\partial k}{\partial x_j}\right] \\
&\quad +\mu_t\frac{\partial U_i}{\partial x_j}\left(\frac{\partial U_i}{\partial x_j} + \frac{\partial U_j}{\partial x_i}\right) - \rho\varepsilon, \qquad (4.25)\\
\rho\frac{\partial}{\partial t}\varepsilon + \rho U_j\frac{\partial}{\partial x_j}\varepsilon &= \frac{\partial}{\partial x_j}\left[\left(\mu + \frac{\mu_t}{\sigma_\varepsilon}\right)\frac{\partial \varepsilon}{\partial x_j}\right] \\
&\quad +c_1\mu_t\frac{\varepsilon}{k}\frac{\partial U_i}{\partial x_j}\left(\frac{\partial U_i}{\partial x_j} + \frac{\partial U_j}{\partial x_i}\right) - \rho c_2\frac{\varepsilon^2}{k}, \qquad (4.26)
\end{aligned}$$

where U_g is the geographic wind vector.

We take numerical experiments with same parameters by the CFV method. Results are presented in Figures 4.16, 4.17, 4.18 and 4.19. From the previous results in Figures 4.2, 4.3, 4.4 and 4.5, we observe a slow decreasing of the horizontal profile of U_x from the inlet direction. This issue can be solved by involving the Coriolis force and the geographic wind. We first simulate the case under the same domain and mesh grids over a flat terrain with no roughness change. The time iteration is set to be long enough (30000 s) in order to get the stable results. The outcome of this simulation is then used as an inlet profile for tests of the roughness change model. In Figures 4.16, 4.17, 4.18 and 4.19, the results of the simulation

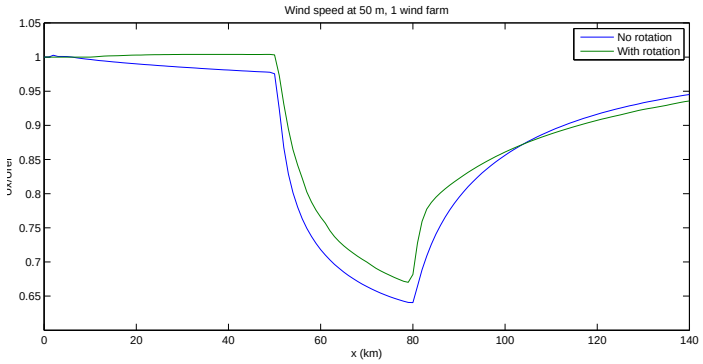

Figure 4.16: Horizontal velocity profile at z=50 m, one wind farm.

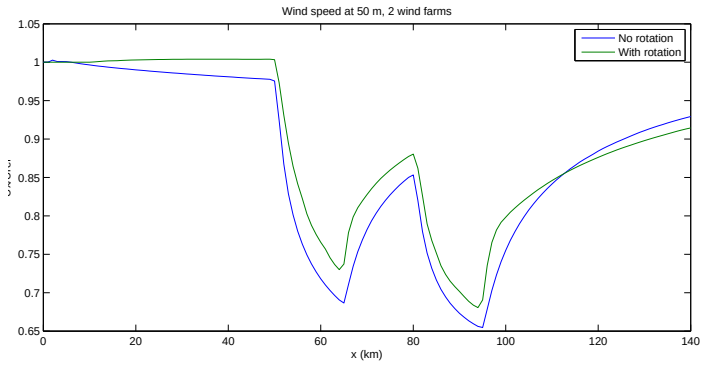

Figure 4.17: Horizontal velocity profile at z=50 m, two wind farms.

with 1, 2, 3, and 10 wind farms are shown. Comparing with the results obtained with and without rotation effects, the horizontal wind profiles with rotation effect are well maintained. The wind speed deficit is slower when the Coriolis Effect is involved.

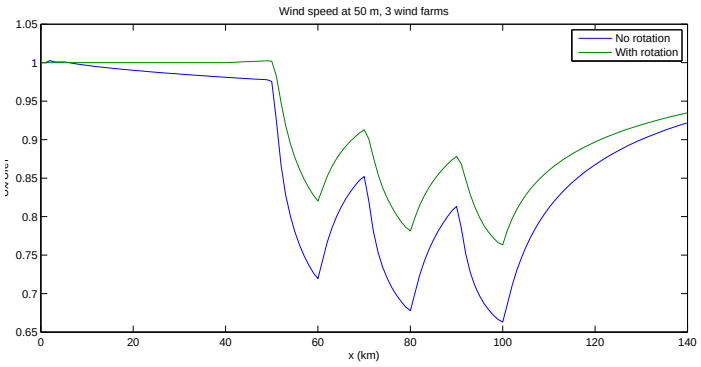

Figure 4.18: Horizontal velocity profile at z=50 m, three wind farms.

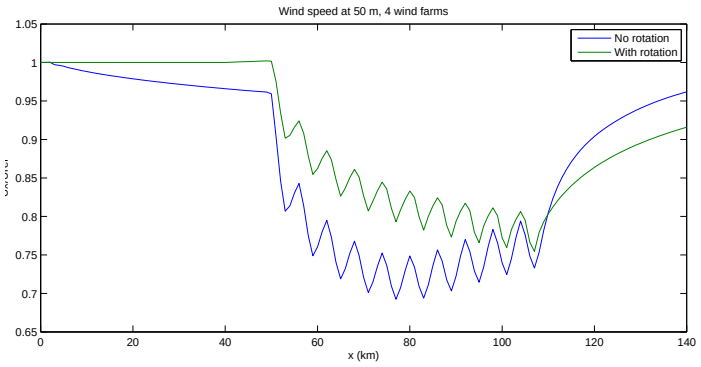

Figure 4.19: Horizontal velocity profile at z=50 m, ten wind farms.

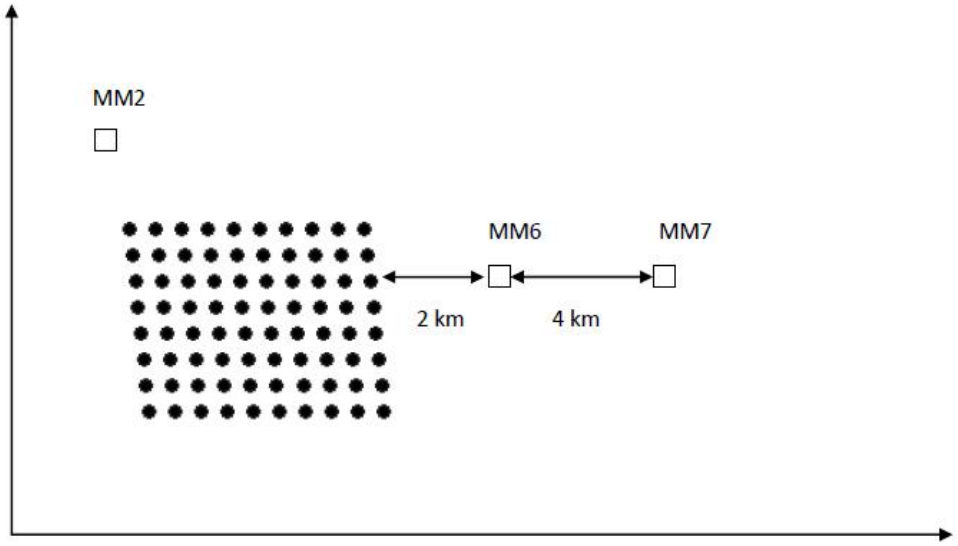

Figure 4.20: Horns Rev wind farm in the North Sea near Denmark.

4.4 Simulation on Horns Rev wind farm

[35] introduced the field measurements on Horns Rev wind farm, which is an offshore wind farm located in the North Sea near Denmark. In Figure 4.20, Horns Rev consists 8 rows of 10 2MW wind turbines which have a hub height of 70 m and rotor diameter $D = 80$ m. When the wind direction is 270 degree, the spacing between rows and columns is $7D$. When the wind speed is around 8 m/s, the thrust coefficient C_T can be taken as $C_T = 0.8$. There are three meteorology masts, MM2, MM6, and MM7, which capture the wind speed.

We use the roughness change models to obtain the numerical results and com-

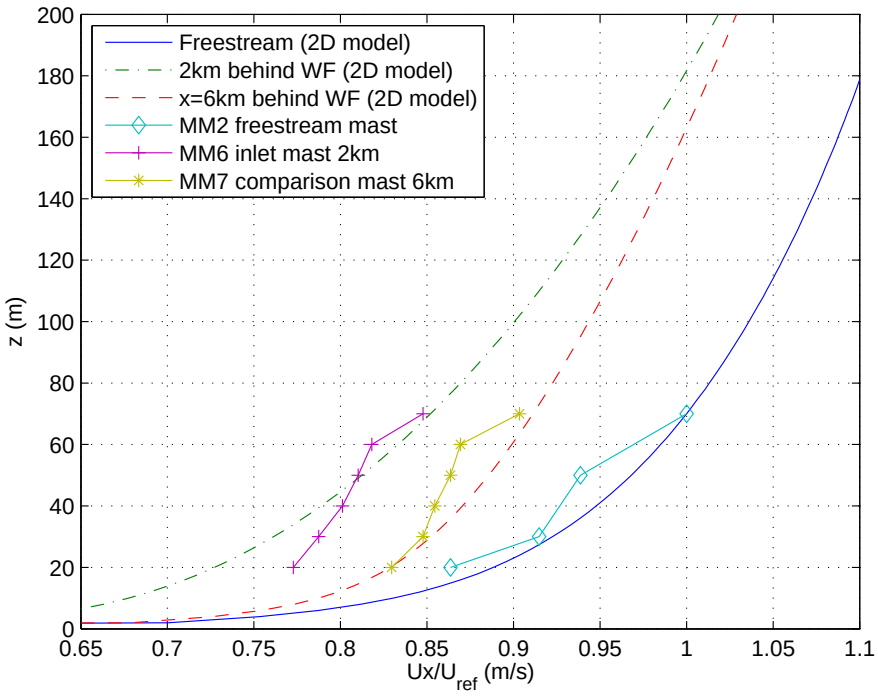

Figure 4.21: Comparison between measurements and model results for MM2, MM6, MM7.

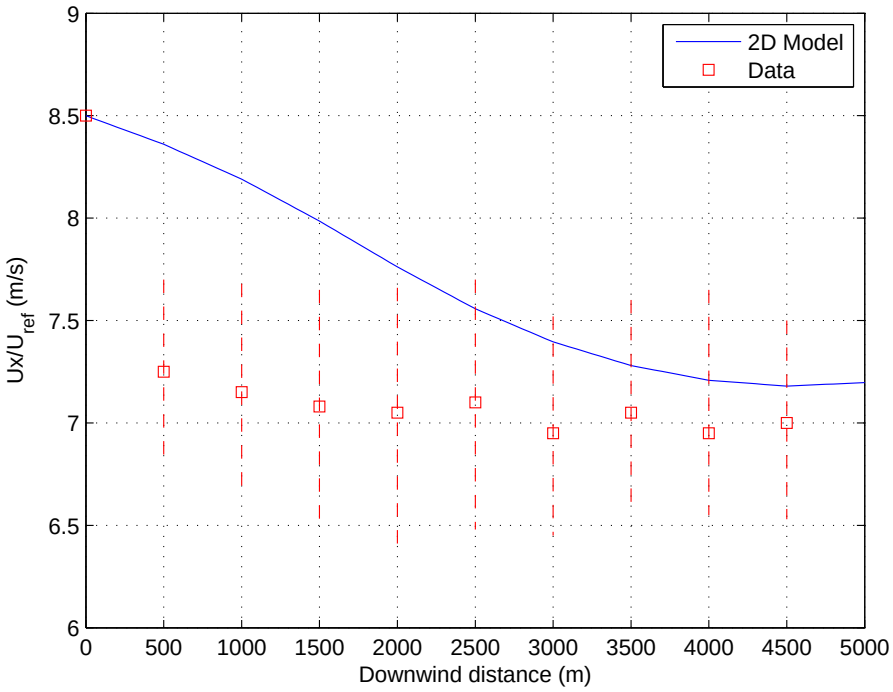

Figure 4.22: Comparison between measurements and model results within the wind farm, the fourth row.

pare to the field data. In Figure 4.21 vertical profiles of the wind speed are given, we use the upstream wind speed measured at height of 70 m as a reference velocity. Wind speeds are measured at different height of location MM2, MM6, and MM7. Our model predictions agree with the field data. At the downwind location MM6, a 2 km downwind of Horns Rev, comparing to the upstream velocity at MM7, a 6 km downwind of Horns Rev, the wind speed starts clearly to recover.

We also compare the field data within the wind farm. Wind speed at hub height (70 m) are measured for the fourth row of Horns Rev, which is the row in the middle of the wind farm. In Figure 4.22 downwind evolution of wind speed at hub height is given, the wind speed at the first hub is used as a reference speed. Our model prediction catches the speed reduction correctly. The model over-predicts the wind speed for the first 4 wind turbines, and it's prediction agrees well thereafter.

5 Conclusion

In this Thesis, we studied and developed numerical methods which are used in Computational Fluid Dynamics. Related to the wind energy industry, the nature of high Reynolds numbers of the air flows requires well-treatment on representing the turbulence. In our development, the Reynolds Averaged Navier-Stokes equations with turbulent closures were considered for simulating wind flows over complex topography and turbine wakes of wind farms.

In Chapter 2, we examined the iteration procedure of the Non-linear MSFD method. We improved the stability of the iteration method by adjusting the relaxation factors based on different surface roughness. Before such adjustment, the iteration procedure only converges when the maximum slope of the topography is less or equal to 0.3. We proposed the suitable choices of the relaxation factors which improved the computational stability on the topography with a much higher maximum slope. Flow separations were successfully predicted in the experiments

on a sinusoidal terrain while the previous result had no separation observed. The application on Bolund hill showed the potential of Non-linear MSFD on real topographies with high maximum slopes.

In Chapter 3, we developed the efficient CFV method for solving the time-dependent RANS equations with $k - \varepsilon$ closure by combining the characteristic method and the finite volume technique. The material derivative was discretized by the characteristic method. The developed CFV method is more stable and accurate than other commonly used time schemes such as the Euler method. This method was applied to many problems related to wind flows over different complex terrains with high maximum slopes. We successfully showed the flow separations on the complex topography by using this method. We solved the wind flows of a realistic topography over Bolund hill, and obtained a better result than the Non-linear MSFD method.

In Chapter 4, we further developed the CFV method to model wind flow and turbine wakes in wind farms. We considered the wind farms as higher surface roughness than the surroundings. The CFV method successfully predicted the wind speed deficit within the wind farms and turbine wake recovery. Results were presented for both two-dimensional and three-dimensional cases. The Coriolis Ef-

fect and geostrophic wind were also studied when taking into account of the large scale problems. Simulating by the CFV method, the RANS models and $k - \varepsilon$ closure with Coriolis force showed success in predicting wind flows over large wind farms due to the rotation of the Earth. Simulations on the Horns Rev wind farm are in a good agreement with field measurements.

The CFV method developed in this study can be used in solving related fluid dynamic problems and it has the potentials on applications related to wind energy industry.

Bibliography

[1] Adrian, G., Fiedler, F., *Simulation of unstationary wind and temperature fields over complex terrain and comparison with observations*. Beitraege zur Physik der Atmosphaere, 64, 1991, 27-48.

[2] Abbey, C., Joós, G., *A Stochastic Optimization Approach to Rating of Energy Storage Systems in Wind-Diesel Isolated Grids*, IEEE TRANSACTIONS ON POWER SYSTEMS, 24(1), 2009, 418-426.

[3] Akhgari, P. A., Kamalan, H., *Economical - environmental evaluation of natural gas and renewable energy systems*, Int. J. Energy Res., 37, 2013, 1550-1561.

[4] Ayotte, K. W., Xu, D., Taylor, P. A. *The impact of turbulence schemes on predictions of the mixed spectral finite-difference model of flow over topography*, Boundary-Layer Meteorol. 68, 1994, 1-33.

[5] Barthelmie, R. J., Frandsen, S. T., Rathmann, O., Hansen, K., Politis, E. S., Prospathopoulos, J., Schepers, J. G., Rados, K., Cabezón, D., Schlez, W., Neubert, A., Heath, M. *Flow and wakes in large wind farms: Final report for UpWind WP8*, Risø-R-1765(EN), 2011.

[6] Bechmann, A., Berg, J., Courtney, M. S., Jrgensen, H. E., Mann, J., Srensen, N. N., *The Bolund experiment: Overview and background. Technical Report Risø-R1658(EN)*, Risø DTU, National Laboratory for Sustainable Energy, Roskilde, Denmark, 2009.

[7] Burggraf, O. S., Duck, P. W., *Spectral Computation of Triple-Deck Flow*. RF Project 760325/712792, Technical Report 3. Ohio State University.

[8] Bechmann, A., Sørensen, N. N., Berg, J., Mann, J., Rethore, P. E. *The Bolund Experiment, Part II: Blind Comparison of Microscale Flow Models*, Boundary-Layer Meteorol. 141(2), 2011, 245-271.

[9] Belcher, S. E., Jerram, N., Hunt, J. C. R. *Adjustment of a turbulent boundary layer to a canopy of roughness elements*, J. Fluid. Mech., 488, 2003, 369-398.

[10] Beljaars, A. C. M., Walmsley, J. L., Taylor, P. A. *A mixed spectral finite-difference model for neutrally stratified boundary-layer flow over roughness changes and topography*, Boundary-Layer Meteorol. 38, 1987, 273-03.

[11] Berg, J., Mann, J., Bechmann, A., Courtney, M., Jørgensen, H. *The Bolund experiment, part I: flow over a steep, three-dimensional hill*, Boundary-Layer Meteorol. 141(2), 2011, 219-243.

[12] Castro, F. A., Palma, J. M. L. M., Silva, L. *A Simulation of the Askervein Flow. Part 1: Reynolds Averaged Navier-Stokes Equations ($k - \varepsilon$ Turbulence Model)*, Boundary-Layer Meteorol., 107, 2003, 501-530.

[13] Casulli, V. *Semi-implicit Finite Difference Methods for 2D shallow water equations*, J. Comp. Physics. 86, 1990, 56-74.

[14] Cherry, N. J., *Wind energy resource survey methodology* Journal of Industrial Aerodynamics, 5, 1980, 247-280.

[15] Chompoo-inwai, C., Chompoo-inwai, C., Leelajindakrairerk, M., Banjongjit, S., Fuangfoo, P., Lee, W. J. *Design Optimization of Wind Power Planning for a Country With Low-Medium-Wind-Speed Profile*, IEEE TRANSACTIONS ON INDUSTRY APPLICATIONS, 44(5), 2008, 1341-1347.

[16] Corbett, J. F., Ott, S., Landberg, L. *A Mixed Spectral-Integration Model for Neutral Mean Wind Flow Over Hills*, Boundary-Layer Meteorol., 128, 2008, 229-254.

[17] Crawford, R. H., *Life cycle energy and greenhouse emissions analysis of wind turbines and the effect of size on energy yield*, Renewable and Sustainable Energy Reviews, 13, 2009, 2653-2660.

[18] Crespo, A., Hernandez, J., Frandson, S. *Survey of modelling methods for wakes and wind farms*, Wind Energy, 2, 1999, 1-24.

[19] Davidson, P. A., *Turbulence: An introduction for scientists and engineers*, Oxford University Press, 2004.

[20] Dalpe, B., Masson, C. *Numerical simulation of wind flow near a forest edge*, J. Wind. Eng. Ind. Aerodyn., 97, 2009, 228-241.

[21] Deardorff, J. W. *A numerical study of three-dimensional turbulent channel flow at large Reynolds numbers*, J. Fluid. Mech., 41, 1970, 453-480.

[22] Doering, C. R., Gibbon, J. D. *Applied analysis of the Navier-Stokes equations*, Cambridge University Press, 1995.

[23] Douglas, J., Russell, T. F. *Numerical methods for convection-dominated diffusion problems based on combining the method of characteristics with finite element or finite difference procedures*, SIAM J. Numer. Anal., 19, 1982, 871-885.

[24] Elhadidy, M. A., Shaahid, S. M., *Exploitation of renewable energy resources for environment-friendly sustainable development in Saudi Arabia*, International Journal of Sustainable Engineering, 2(1), 2009, 56-66.

[25] Frandsen, S., Barthelmie, R., Pryor, S., Rathmann, O., Larsen, S., Hojstrup, J., Thogersen, M. *Analytical modelling of wind speed deficit in large offshore wind farms*, Wind Energy, 9, 2006, 39-3.

[26] Frandsen, S. T., Jørgensen, H. E., Barthelmie, R., Rathmann, O., Badger, J., Hansen, K., Ott, S., Rethore, P. E., Larson, S. E., Jensen, L. E., *The making of a second-generation wind farm efficiency model complex*, Wind Energy, 12, 2009, 445-458.

[27] Finnigan, J. J., Belcher, S. E. *Flow over a hill covered with a plant canopy*, Q. J. R. Met. Soc., 130, 2004, 1-29.

[28] Frandsen, S., Madsen, P. H. *Spatially average of turbulence intensity inside large wind turbine arrays*. Offshore Wind Energy in Mediterranean and other European Seas: Resources, Technology, Applications: European Seminar, Naples, Italy, ATENA/EWEA, 2003, 10-12, 97-106.

[29] Frisch, U., *Turbulence*, Cambridge University Press, 1995.

[30] Global Wind Energy Council, Global Wind Report Annual Market update, 2012.

[31] Gong, W., Taylor, P. A., Dornbrack, A. *Turbulent boundary-layer flow over fixed, aerodynamically rough, 2D sinusoidal waves*, J. Fluid. Mech. 312, 1996, 1-37.

[32] Gorle, C., van Beeck, J., Rambaud, J., van Tendeloo, G. *CFD modelling of small particle dispersion: the influence of the turbulent kinetic energy in the atmospheric boundary layer*, Atmospheric Environment 43, 2009, 673-681.

[33] Hanjalic, K., Kenjeres, S. *Some developments in turbulence modeling for wind and environmental engineering*, J. Wind. Eng. Ind. Aerodyn., 96, 2008, 1537-1570.

[34] Hargreaves, D. M., Wright, N. G. *On the use of the k-epsilon model in commercial CFD software to model the neutral atmospheric boundary layer*, J. Wind. Eng. Ind. Aerodyn., 95, 2006, 355-369.

[35] Hasager, C. B., Peña, A., Mikkelsen, T., Courtney, M., Antoniou, I., Gryning, S. E., Hansen, P., Sørensen, P. B. *12MW Horns Rev Experiment*, Risø-R-1506(EN), 2007.

[36] He, Y., Chen, X., *Wind turbine generator systems. The supply chain in China Status and problems*, Renewable Energy, 34, 2009, 2892-2897.

[37] Hinze, J. O., *Turbulence*, McGraw-Hill, New York, 1975.

[38] Hong, S., Bradshaw, C. J. A., Brook, B. W., *Evaluating options for the future energy mix of Japan after the Fukushima nuclear crisis*, Energy Policy, 56, 2013, 418-424.

[39] Huenteler, J., Schmidt, T. S., Kanie, N., *Japan's post-Fukushima challenge implications from the German experience on renewable energy policy*, Energy Policy, 45, 2012, 6-11.

[40] Issa, R. I., *Solution of the implicitly discretised fluid flow equations by operator-splitting*, J. Comp. Physics. 62, 1985, 40-65.

[41] Jackson, P. S., Hunt, J. C. R., *Turbulent flow over a low hill*, Q. J. Roy. Meteorol. Soc., 101, 1975, 929-55.

[42] Jakirlic S, Manceau R, Saric S, Fadai-Ghotbi A, Kniesner B, Carpy S, Kadavelil G, Friess C, Tropea C, Boree J *LES, Zonal and Seamless Hybrid LES/RANS: Rationale and Application to Free and Wall-Bounded Flows Involving Separation and Swirl*, Numerical Simulation of Turbulent Flows and Noise Generation Notes on Numerical Fluid Mechanics and Multidisciplinary Design, 104, 2009, 253-282.

[43] Jasak, H. *Error Analysis and Estimation for Finite Volume Method with Applications to Fluid Flow*, PhD thesis, Imperial College, University of London, 1996.

[44] Karpik, S. R., *An improved method for integrating the mixed spectral finite difference (MSFD) model equations*, Boundary-Layer Meteorol. 43, 1988, 273-86.

[45] Kasmi, A. E., Masson, C. *An extended $k-\varepsilon$ model for turbulent flow through horizontal-axis wind turbines*, J. Wind. Eng. Ind. Aerodyn., 96, 2008, 103-122.

[46] Lackner, M. A., Rogers, A. L., Manwell, J. F., *The round robin site assessment method A new approach to wind energy site assessment*, Renewable Energy, 33, 2008, 2019-2026.

[47] Launder, B. E., Spalding, D.B. *The numerical computation of turbulent flows*, Computer. Meth. App. Mech. Eng. 3, 1974, 269-289.

[48] Liang, D., Du, C., Wang, H. *A fractional step ELLAM approach to high-dimensional convetion-diffusion problems with forward particle tracking*, J. Comp. Physics, 221, 2007, 198-225.

[49] Lopes da Costa, J. C., Castro, F. A., Palma, J. M. L. M., Stuart, P. *Computer Simulation of Atmospheric Flows over Real Forests for Wind Energy Resource Evaluation*, J. Wind. Eng. Ind. Aerodyn. 94, 2006, 603-620.

[50] Mangi, S. C., *The Impact of Offshore Wind Farms on Marine Ecosystems A Review Taking an Ecosystem Services Perspective*, IEEE, 101(4), 2013, 999-1009.

[51] Martinez-Cesena, E. A., Mutale, J., *Wind Power Projects Planning Considering Real Options for the Wind Resource Assessment*, IEEE TRANSACTIONS ON SUSTAINABLE ENERGY, 3(1), 2012, 158-166.

[52] Mason, P. J., Sykes, R. I., *Flow Over an Isolated Hill of Moderate Slope*, Q. J. Roy. Meteorol. Soc. 105, 1979, 383-395.

[53] Mason, P. J. *Large-eddy simulation, A critical review of the technique*, Q. J. R. Meteorol. Soc., 120, 1994, 1-26.

[54] Mellor, G. L., Yamada, T., *Development of a turbulence closure model for geophysical fluid problems*, Review of Geophysics and Space Physics, 20(4), 1982, 851-875.

[55] OpenFOAM CFD program. www.openfoam.org.

[56] Patankar, S. V., Spalding, D. B., *A calculation procedure for heat, mass and momentum transfer in three-dimensional parabolic flows*, Int. J. Heat. Mass. Transfer., 15, 1972, 1787-1806.

[57] Patankar, S. V. *Numerical heat transfer and fluid flow*, Hemisphere Publishing Corporation, Washington, DC. 1980.

[58] Palma, J. M. L. M., Castro, F. A., Ribeiro, L. F., Rodrigues, A. H., Pinto, A. P., *Linear and nonlinear models in wind resource assessment and wind turbine micro-siting in complex terrain*, J. Wind. Eng. Ind. Aerodyn. 96, 2008, 2308-2326.

[59] Patankar, S. V., Spalding, D. B. *A calculation procedure for heat, mass and momentum transfer in three-dimensional parabolic flows*, Int. J. Heat Mass Transfer, 15, 1972, 1787-1806.

[60] Petersen, E. L., Mortensen, N. G., Landberg, L., Højstrup, J., Frank, H. P., *Wind power meteorology. Part I: climate and turbulence*, WIND ENERGY, 1, 1998, 2-22.

[61] Petersen, E. L., Mortensen, N. G., Landberg, L., Højstrup, J., Frank, H. P., *Wind power meteorology. Part II siting and models*, WIND ENERGY, 1, 1998, 55-72.

[62] Pironneau, O. *On the transport-diffusion algorithm and its applications to the Navier-Stokes equations*, Numer. Math. 38, 1982, 309-332.

[63] Prasad, R. D., Bansal, R. C., Sauturaga, M., *Wind Energy Analysis for Vadravadra Site in Fiji Islands A Case Study*, IEEE TRANSACTIONS ON ENERGY CONVERSION, 24(3), 2009, 750-757.

[64] Quinn, A. D., Richards, P. J. *A 6m cube in an atmospheric boundary layer flow Part 2: Computational solutions*, Wind and Structures, 5, 2002, 177-192.

[65] Reynolds, O., *On the dynamical theory of incompressible viscous fluids and the determination of the criterion*, Phil. Trans. R. Soc. Lond. A. 186, 1895, 123-164.

[66] Rhie, C. M., Chow, W. L. *Numerical Study of the Turbulent Flow Past an Airfoil with Trailing Edge Separation*, AIAA Journal, 21(11), 1983, 1525-1532.

[67] Riddle, A., Carruthers, D., Sharpe, A., McHugh, C., Stocker, J., *Comparisons between FLUENT and ADMS for atmospheric dispersion modelling*, Atmospheric Environment, 38(7), 2004, 1029-1038.

[68] Robert, A. *The integration of a low order spectral form of the primitive meteorological equations*, J. Meteor. Soc. Japan 44, 1966, 237-245.

[69] Robert, A. *A stable numerical integration scheme for the primitive meteorological equations*, Atmosphere-Ocean 19, 1981, 35-46.

[70] Sagaut, P. *Large-eddy simulation for incompressible flows*, Springer Press, 2006.

[71] Sahin, A. D., *Progress and recent trends in wind energy*, Progress in Energy and Combustion Science, 30, 2004, 501-543.

[72] Seaid, M. *Semi-lagrangian integration schemes for viscous incompressible flows*, Comp. Meth. App. Math., 2, 2002, 292-309.

[73] Sempreviva, A. M., Larsen, S. E., Mortensen, N. G., Troen, I. *Response of neutral boundary layers to changes of roughness*, Boundary-Layer Meteorology, 50, 1990, 205-226.

[74] Sumner, J., Masson, G. $k-\varepsilon$ *simulations of the neutral atmospheric boundary layer: analysis and correction of discretization errors on practical grids*, Int. J. Numer. Meth. Fluids., published online: Nov 2011 DOI: 10.1002/fld.2709.

[75] Taylor, P. A. *Some numerical studies of surface boundary-layer flow above gentle topography*, Boundary-Layer Meteorol. 11, 1977, 439-465.

[76] Taylor, P. A., Walmsley, J. L., Salmon, J. R., *A simple model of neutrally stratified boundary-layer flow over real terrain incorporating wave number-dependent scaling*, Boundary-Layer Meteorol., 26, 1983, 169-89.

[77] Taylor, P. A., Mason, P. J., Bradley, E. F., *Boundary-layer flow over low hills - A review*, Boundary-Layer Meteorol. 39, 1987, 107-132.

[78] Taylor, P. A., Gallino, S., Li, P. Y., Xu, D. *Airflow over waves: anomalies and a conjecture*, Proc IMA Conference on Wind-over-Wave Couplings, Salford, UK, April 1997.

[79] Teman, R., *Navier-Stokes equations: theory and numerical analysis*, American Mathematical Society, 2001.

[80] Versteeg, H. K., Malalasekera, W., *An intruduction to computational fluid dynamics: The finite volume method*, Longman Press, 1995.

[81] Walmsley, J. L., Salmon, J. R., Taylor, P. A., *On the application of a model of boundary-layer flow over low hills to real terrain*, Boundary-Layer Meteorol., 23, 1982, 17-46.

[82] Walmsley, J. L., Taylor, P. A., Keith, T., *A simple model of neutrally stratified boundary-layer flow over complex terrain with surface roughness modulations*, Boundary-Layer Meteorol. 36, 1986, 157-186.

[83] Wang, H., Liang, D., Ewing, R. E., Lyons, S. L., Qin, G. *An Approximation to Miscible Displacement in Porous Media with Point Sources and Sinks by an Eulerian-Lagrangian Localized Adjoint Method and Mixed Finite Element Methods*, SIAM J. Sci. Comput. 22, 2000, 561-581.

[84] Wang, L., Yeh, T. H., Lee, W. J., Chen, Z., *Benefit Evaluation of Wind Turbine Generators in Wind Farms Using Capacity-Factor Analysis and Economic-Cost Methods*, IEEE TRANSACTIONS ON POWER SYSTEMS, 24(2), 2009, 692-704.

[85] Weng, W., Taylor, P. A., Salmon, J. R. *A 2-D numerical model of boundary-layer flow over single and multiple surface condition changes*, J. Wind. Eng. Ind. Aerodyn., 98, 2010, 121-132.

[86] Xu, D., Taylor, P. A. *A non-linear extension of the Mixed Spectral Finite Diffrence model for neutrally stratified flow over topography*, Boundary-Layer Meteorol. 59, 1992, 177-186.

[87] Yu, X., Weng, W., Taylor, P. A., Liang, D., *Relaxation Factor Effects in the Non Linear Mixed Spectral Finite Difference Model of Flow over Topographic Features*, Boundary-Layer Meteorology, 140, 2011, 23-35.

[88] Yu, X., Liang, D., Taylor, P.A., *Characteristic methods for Reynolds Averaged Navier-Stokes equations of flow over topography*, Submitted, 2013.

[89] Zhang, Y., Chowdhury, A. A., Koval, D. O., *Probabilistic Wind Energy Modeling in Electric Generation System Reliability Assessment*, IEEE TRANSACTIONS ON INDUSTRY APPLICATIONS, 47(3),2011, 1507-1514.